



City Research Online

City, University of London Institutional Repository

Citation: Jennings, Ben (2013). Chromatic sensitivity: effects of light level and selective photoreceptor adaptation. (Unpublished Doctoral thesis, City University London)

This is the unspecified version of the paper.

This version of the publication may differ from the final published version.

Permanent repository link: <https://openaccess.city.ac.uk/id/eprint/2459/>

Link to published version:

Copyright: City Research Online aims to make research outputs of City, University of London available to a wider audience. Copyright and Moral Rights remain with the author(s) and/or copyright holders. URLs from City Research Online may be freely distributed and linked to.

Reuse: Copies of full items can be used for personal research or study, educational, or not-for-profit purposes without prior permission or charge. Provided that the authors, title and full bibliographic details are credited, a hyperlink and/or URL is given for the original metadata page and the content is not changed in any way.

**Chromatic sensitivity:
effects of light level and selective
photoreceptor adaptation**

Ben J. Jennings

Doctor of Philosophy

City University London

Applied Vision Research Centre

Department of Optometry and Visual Science

March 2013

Contents

List of figures.....	Page 6
List of Tables.....	13
Commonly used symbols and abbreviations.....	14
Acknowledgments.....	15
Declaration.....	16
Abstract.....	17
Chapter 1 - Vision	
1.1 Introduction.....	18
1.2 The eye.....	18
1.3 The human eye.....	19
1.4 Connection to the brain.....	23
1.5 Photoreceptors	26
1.5.1 Rods.....	26
1.5.2 Cones.....	27
1.6 The Retinal distribution of rods and cones and the cone mosaic.....	30
1.7 Other retinal cell types.....	32
1.7.1 Ganglion cells (RGCs).....	33
1.7.2 Photosensitive retinal ganglion cells.....	33
1.7.3 Amacrine cells.....	34
1.7.4 Bipolar cells.....	34
1.7.5 Horizontal cells.....	35
1.8 Retinal layers.....	36
1.9 The lateral geniculate nucleus.....	37
1.10 Electromagnetic radiation.....	38
1.10.1 Photons.....	39
1.10.2 Electromagnetic wavelength and frequency.....	39
1.10.3 Photon speed and energy.....	41
1.11 Luminance and retinal illuminance.....	41
1.12 Contrast.....	42
1.13 Sensitivity over various light levels.....	43
1.13.1 Photopic vision.....	44
1.13.2 Scotopic vision.....	45
1.13.3 Mesopic vision.....	45
1.13.4 Purkinje shift.....	46
1.14 Luminosity efficiency function.....	47
1.15 Colour.....	48
1.15.1 Hue, brightness and saturation.....	49
1.15.2 Additive and Subtractive colour mixing.....	50
1.16 Colour vision.....	51
1.16.1 Trichromatic theory.....	52
1.16.2 Opponent process theory.....	53
1.16.3 Unique hues.....	57
1.16.4 The CIE 1931 colour space.....	58

1.16.5 CIE standard 2 deg standard observer and the colour matching functions.....	59
1.16.6 Wavelength discrimination.....	60
1.16.7 Colour discrimination – MacAdam’s ellipses.....	62
1.16.8 Chromatic Adaptation.....	64
1.16.9 Pre-photoreceptor filters.....	66
1.17 Macular pigment density.....	66
1.18 Lens pigment density.....	67

Chapter 2 - Materials, Methods and Data Processing

2.1 Introduction.....	69
2.2 The Colour Assessment and Diagnosis (CAD) Test.....	69
2.2.1 CAD Test Equipment.....	70
2.2.2 Monitor Calibration.....	71
2.2.3 Gamma Correction.....	71
2.2.4 Red, Green and Blue Monitor Phosphor Calibration.....	74
2.2.5 CAD stimulus and experimental procedure.....	75
2.2.6 Neutral Density filters.....	77
2.3 Data processing.....	78
2.3.1 The use of ellipses.....	79
2.3.2 Fitting algorithm.....	80
2.3.3 Cone excitations and contrasts.....	82
2.3.4 Cone contrast curves.....	86
2.4 P_scan-100 Pupillometry system.....	88
2.5 The Macular Assessment Profile (MAP) test.....	89

Chapter 3 - Colour detection thresholds as a function of chromatic adaptation and light level

3.1 Introduction.....	93
3.2 Background.....	94
3.3 Selection of background chromaticities and luminance levels.....	95
3.4 Experimental procedure and data processing.....	95
3.5 Results.....	98
3.5.1 Variation in detection thresholds.....	99
3.5.2 L- and M-cones.....	100
3.5.3 S-Cones.....	102
3.6 Reconstruction of ellipses.....	103
3.7 Additional data for detections made at 24 cd m ⁻²	107
3.8 Comparison with MacAdam’s ellipses.....	108
3.9 Comparison with the Cambridge Colour Test.....	110
3.10 Discussion and Conclusion.....	113

Chapter 4 - Effect of the Adapting Field on Chromatic Sensitivity

4.1 Introduction.....	115
4.2 Re-adaptation time control experiment.....	116
4.3 Method and data collection.....	117
4.4 Observer BJ.....	119
4.5 Results.....	119
4.5.1 Variation of thresholds along cardinal L-M and S axes.....	122
4.5.2 L- and M-cone thresholds along L-M and S axes.....	123
4.5.3 S-cones thresholds along the L-M and S axes.....	126

4.5.4	Variation of thresholds with respect to ellipse orientation.....	128
4.5.5	L- and M-cones thresholds along the ellipse axes.....	130
4.5.6	S-cones thresholds along the ellipse axes.....	134
4.5.7	Distribution of Ellipse orientations.....	135
4.5.8	Fitting errors.....	141
4.6	Discussion and Conclusion.....	142

Chapter 5 - Effect of chromatic adaptation as a function of retinal location

5.1	Introduction.....	144
5.2	Method.....	145
5.3	Observers.....	147
5.4	No border control experiment.....	147
5.5	Results.....	149
5.5.1	Equal adapting field and target chromaticity results.....	149
5.5.2	Different adapting field and target chromaticity results.....	150
5.6	Discussion and Conclusion.....	152

Chapter 6 - The variation of cone contrasts at threshold with Macular Pigment optical density

6.1	Introduction.....	154
6.2	Method.....	155
6.2.1	Colour Assessment and Diagnosis (CAD) test.....	155
6.2.2	Macular Assessment Profile (MAP) test.....	156
6.3	Results.....	156
6.3.1	Range of test subject macular pigment levels.....	156
6.3.2	Ellipse orientation vs. macular pigment levels.....	158
6.3.3	The effect of ellipse size and orientation on cone contrast curves.....	160
6.3.3.1	Variation of ellipse size and cone contrast curves.....	161
6.3.3.2	Variation of ellipse orientation and cone contrast curves...	163
6.3.4	Extraction of L- and M-cone gradients from the fitted data.....	166
6.3.4.1	L- and M-cone gradients in the reddish and greenish colour directions.....	167
6.3.4.2	Predicting macular pigment levels from cone contrasts.....	170
6.3.5	Correcting cone fundamentals for macular pigment.....	170
6.3.5.1	Effect of macular pigment corrected cone sensitivities on the L- and M-cone contrast curves.....	172
6.3.5.2	Effect of macular pigment corrected cone sensitivities on the S-cone contrast curves.....	174
6.3.6	Correcting cone fundamentals for lens yellowing.....	176
6.4	Discussion and conclusion.....	177

Chapter 7 - Cone noise, pupil size and photoreceptor excitation

7.1	Introduction.....	179
7.2	Introduction - Experiment 1.....	179
7.3	Method and data collection.....	182
7.4	Results.....	183
7.4.1	Pupil size vs. rod, cone and melanopsin excitation.....	185
7.5	Conclusion – experiment 1.....	188
7.6	Introduction - experiment 2.....	189
7.7	Method and data collection.....	190
7.8	Results.....	190

7.8.1 Variation of L-, M and S-cone contrast signal-to-noise ratio.....	192
7.9 Conclusion – experiment 2.....	195
Final conclusions.....	196
References.....	200

List of figures

Fig. 1.1(a) and (b) An anterior external view of a female human's left eye is shown in (a), a sagittal schematic of a human eye is shown in (b), adapted from healthy eyes (2012). **Page .20.**

Fig. 1.2 A transverse slice through the series of physical connections from the eye to the primary visual area is illustrated. Image modified from Young (2007). **Page .24.**

Fig. 1.3 A rod cell oriented relative to the direction of incoming photons. Diagram adapted from Heeger (2012). **Page .27.**

Fig. 1.4 A cone cell oriented relative to the direction of incoming photons. Diagram adapted from Heeger (2012). **Page .28.**

Fig. 1.5 The 2° Stockman-Sharpe cone fundamentals. The data were obtained from the Institute of Ophthalmology (University of London) Colour & Vision Research Laboratory (cvrl.org, accessed July 2011), the data was plotted using the 1nm step size option provided by the CVRL database. **Page .30.**

Fig. 1.6 The distribution of rods and cones as a function of eccentricity in the temporal and nasal direction. The area over the optic disc has a complete absence of rods and cones. **Page .31.**

Fig. 1.7 The central (~1°) region of the normal human cone mosaic showing the arrangement of the L- (shown in red), M- (shown in green) and S-cones (shown in blue). S-cones are typically absent from the central 0.2 – 0.3° (indicated by the black circle). Image adapted from Gegenfurtner and Sharpe (2000). **Page .32.**

Fig. 1.8 A cross section of the retina, the structure and organisation of the different cell types are shown. Within this figure light would be entering through the pupil located at the bottom of the diagram, reaching the rods and cone lastly after all other cells. Image reproduced from American Scientist (Jan/Feb 2003). **Page .37.**

Fig. 1.9(a) and (b) The electromagnetic spectrum (a), the visible region between ~400 and ~700nm is shown expanded. A sinusoidal wave is shown in (b), one wavelength λ is indicated by the black horizontal bar. **Page .40.**

Fig. 1.10 Various properties of the human visual system as a functions of each other. Modified from Sacek (2006). **Page .44.**

Fig. 1.11(a) and (b) Blue bell flowers illuminated under daytime blue skylight (a) and evening twilight (b), the shift from (a) to (b) corresponds to a more intensely saturated bluish/violet colour being perceived. **Page .46.**

Fig. 1.12 The $V^*(\lambda)$ function plotted over the visible spectrum. Data from CVRL database tabulated data in 1nm stepsizes. **Page .48.**

Fig. 1.13 The HVL colour space relating a colours hue, saturation and brightness (labelled as value). Image reproduced from the QT: Online newsletter (Adaptive Coloring for Syntax Highlighting, Helder Correia, 2010). **Page .49.**

Fig. 1.14(a) and (b) Illustrates the additive colour mixing of the three red, green and blue primary light sources, (b) illustrates the subtractive mixing using the cyan, magenta and yellow as the primary coloured paint pigments. **Page .51.**

Fig. 1.15 The opponent process combines the L_s , M_s and S_s cone signals into the two opponent chromatic pathways and one luminance pathway. The +/- symbols in boxes denote that the signals are either being summed or subtracted. The +/- symbol not surrounded by boxes refer to the signal either being an increment or a decrement. **Page .55.**

Fig. 1.16 The two chromatic and luminance pathways of the DKL colour space are represented. r is a vector, the length of which represents the difference of a chromaticity relative to point (0,0,0), θ describes the chromaticity in terms of the angle between chromatic pathways and \emptyset represents the contribution of the luminance pathway. **Page .56.**

Fig. 1.17 Unique hue data shown relative to the L-M and S-(L+M) axes. Modified from Wuerger (2005). **Page .57.**

Fig. 1.18 The CIE 1931 xy chromaticity diagram. Image adapted from savory.de (Accessed July 2011). **Page .59.**

Fig. 1.19(a)and (b) The classic wavelength discrimination experiment stimulus; the test field of wavelength λ (left) and the comparison field of wavelength $\lambda+\Delta\lambda$ (right). The typical "W" shaped plot obtained over the visible spectrum for λ vs. $\Delta\lambda$. Adapted from Wright and Pitt (1934). **Page .62.**

Fig. 1.20 A single MacAdam's ellipse;, the white circles are the standard deviations for colour matches made with respect to the reference colour, located CIE xy:(0.160, 0.057), along different directions of the colour space. The back contour is the best fit ellipse that represents the average standard deviation for each colour direction. Reproduced from MacAdam (1942). **Page .63.**

Fig. 1.21 All 25 MacAdam's ellipses (scaled x10) illustrated in CIE 1931 colour space. Image adapted from photometrictesting.co.uk (accessed Nov 2011). **Page .64.**

Fig. 1.22 The Bone Macular pigment template showing the variation of Macular pigment density as a function of wavelength (nm). **Page .67.**

Fig. 1.23 The pigment density of the crystalline lens is plotted as a function of wavelength (nm). **Page .68.**

Fig. 2.1 The physical set up of the CAD system. **Page .71.**

Fig. 2.2 (a) and (b) The top row of (a) shows an example input luminance gradient, the bottom row shows the results that would be displayed on a non-gamma corrected monitor. The top row of (b) again shows an input luminance gradient, the second row shows the input after the gamma correction has been applied, the bottom row shows the corrected output image, i.e., the desired output image equals the input image (V =voltage, L =luminance). Figure adapted from siggraph.org (accessed Feb 2012). **Page .73.**

Fig. 2.3 The luminance outputs of the RGB phosphors as a function of LUT address. Each phosphor follows a power law as the voltage increases. **Page .74.**

Fig. 2.4 The spectral power distributions of the red, green and blue phosphors, indicated by the red, green and blue curves, respectively. **Page .75.**

Fig. 2.5 An example of a greenish CAD stimulus embedded in the patch of luminance noise. The dimensions of the luminance noise patch and entire display is indicated. **Page .77.**

Fig. 2.6 The transmission spectra of three neutral density filters with OD values of 0.1, 0.4 and 0.5. **Page .78.**

Fig. 2.7 A set of detection thresholds (Black squares) along with a fitted parallelogram (solid line), rectangle (dashed line), and ellipse (dotted curve). Reproduced from Porison *et al.* (1998). **Page .80.**

Fig. 2.8 16 CAD measured thresholds (black circles) shown in CIE xy space for observer SFR. The solid back curve is the contour of the fitted ellipse. The ellipse was measured for a target located at CIE xy: (0.265, 0.420) indicated by the cross. The non-fixed centre fitting algorithm calculated the ellipses centre to be located at CIE xy: (0.266, 0.419) indicated by the triangle. **Page .82.**

Fig. 2.9(a), (b) and (c) Examples of measured threshold data plotted (a) the CIE xy colour space, (b) a relative cone excitation space and (c) cone contrast space. **Page .86.**

Fig. 2.10 (a) and (b) L-, M- and S-cone contrast curves as functions of (a) CIE and (b) cone contrast colour angle, respectively. The insert indicates the approximate colours for each direction in cone contrast space. **Page .88.**

Fig. 2.11(a), (b) and (c) Examples of the MPOD system stimulus presented at a series of eccentricities: (a) zero, (b) +1.8° and (c) +7.8° (c). Image adapted from Barbur *et al.* (2010). **Page .91.**

Fig. 2.12 A typical MPOD profile, in the range from zero (peak MPOD) to 7.8° eccentricity (~zero MPOD). **Page .92.**

Fig. 3.1 Reddish, greenish, yellowish and bluish colour directions (R_t , G_t , Y_t and B_t) shown on a fitted ellipse contour. (x_o, y_o) are the CIE chromaticity co-ordinates of the fitted ellipse centre and (x_{bg}, y_{bg}) are the background/foreground CIE xy coordinates. **Page .97.**

Fig. 3.2 Mean measured ellipse data represented as [L-M]- vs. S-cone excitations plotted as a function of background luminance. The black dots represent the mean measured data; the green crosses represent the projection of these measured points onto the zero luminance plane for clarity. The fitted ellipses for each background are shown as red contours and the black solid line shows how points of constant chromaticity (CIE xy: (0.305, 0.323)) plot over different the luminance levels. **Page .99.**

Fig. 3.3 The changes required in L- and M-cone excitations for threshold in the reddish colour direction versus the L- and M-cone excitations produced by the backgrounds. **Page .100.**

Fig. 3.4 Change in S-cone excitation required to reach threshold in the blue colour direction versus the S-cone excitations produced by the backgrounds. The blue colour direction represents the mean orientation of the major axis of the threshold detection ellipse measured for each of the four subjects investigated in this study. The curve obeys a linear relationship (see Eq.3.6) for relative S-cone excitations above ~ 9 and a power law relationship with a coefficient of 0.56 (see Eq.3.7) for cone excitations below this value. Note that the corresponding changes in L- and M-cones are approximately zero when thresholds are measured in the blue colour direction. **Page .103.**

Fig. 3.5, 3.6, 3.7 and 3.8 The red contours show the predicted ellipses in CIE xy space, the mean measured are thresholds (black dots) are shown for comparison. The luminance levels shown are 1 cd m^{-2} (top left), 3 cd m^{-2} (top right), 8 cd m^{-2} (bottom left) and 24 cd m^{-2} (bottom right). **Page .105.**

Fig. 3.9 The mean errors for each set of predicted ellipse parameters (when grouped by background luminance level). Each error reflects the difference between the measured and the corresponding prediction for that parameter based on the mean fitted ellipse. The large errors are restricted to the semi-major axis and reflect the larger inter-subject variability in S-cone threshold excitation. **Page .107.**

Fig. 3.10 Graphical comparison of mean ellipses for the $n=4$ subjects (red) and $n=18$ subjects (black) groups, no significant differences exist. All ellipses have been scaled along their semi-major and -minor axes for clarity by a factor of 2. **Page .108.**

Fig. 3.11 CIE xy space showing the model predicted ellipses (red contours) and MacAdam's ellipse scaled up by a factor of 4.5. **Page .110.**

Fig. 3.12 The Cambridge Colour Test measured ellipses (black contours) shown in CIE xy space, along with the model predicted ellipses for the same chromatic locations and luminance. **Page .112.**

Fig. 4.1 Detection threshold ellipses measured for varying delay times between each CAD trail presentation. As the delay is increased the detection thresholds increase and then plateau at 2000 ms onwards. The black central ellipse was measured for comparison for the condition where the adapting field (BG) and foreground chromaticities were equal. **Page .117.**

Fig. 4.2 The time course of a CAD stimulus sequence, A: forced 3000 ms adaptation to background, B: CAD stimulus displayed on foreground of luminance noise, C: wait for subject to respond. **Page .118.**

Fig. 4.3 Both the red and black ellipses, shown in cone excitation space, are the results of using a red foreground at CIE xy:(0.3977, 0.3283). The red ellipse is the result of using the same red for the background adapting field, the black ellipse is the result using a white adapting field located at CIE xy : (0.305, 0.323). **Page .120.**

Fig 4.4 (a), (b) and (c) The coordinates of three of the adapting background fields used (large circles), the six measured detection threshold ellipses (small coloured circles) and the corresponding fitted ellipses (solid black lines). A shift in

alignment of the ellipse semi-major axes from the S-cone cardinal axis towards the direction of the adapting chromaticity can be observed. **Page .121.**

Fig. 4.5 An example of the coordinates of an adapting field and foreground combination are illustrated. The size and orientations of the $\pm\delta[L-M]$ and $\pm\delta S$ thresholds are illustrated with respect to the foreground chromaticity. The $\pm\delta[L-M]$ thresholds are defined as the distances from the foreground chromaticity to the ellipse surface (parallel to $[L-M]$ -cone excitation axis), the $\pm\delta S$ thresholds are defined as the distances from the foreground chromaticity to the ellipse surface (parallel to the S-cone excitation axis). X and Y represent the difference between the $[L-M]$ - and S-cone excitations of the adapting field and foreground ($[L-M]_{\text{for-ada}}$ and $S_{\text{for-ada}}$), respectively. X and Y are calculated from Eq.4.1 and Eq. 4.2, respectively. **Page .123.**

Fig. 4.6 The red and green circles represent the thresholds in the $+ [L-M]$ and $- [L-M]$ directions, respectively, for positive and negative $[L-M]_{\text{for-ada}}$ values. Note: the $\pm [L-M]$ axis is not exactly aligned with unique red and green (Philipona, 2006), but $+\delta[L-M]$ and $-\delta[L-M]$ can be considered to be detection thresholds in reddish and greenish colour directions, respectively. **Page .124.**

Fig. 4.7 The blue and yellow circles represent the thresholds in the $+S$ and $-S$ directions, respectively, for positive and negative $[L-M]_{\text{for-ada}}$ values. **Page .127.**

Fig. 4.8 An example of the coordinates of an adapting field and foreground combination is illustrated. The size and orientations of the $\pm\delta[L-M]_{\theta}$ and $\pm\delta S_{\theta}$ thresholds are illustrated with respect to the foreground chromaticity and ellipse orientation. The $\pm\delta[L-M]_{\theta}$ thresholds are defined as the distances from the foreground chromaticity to the ellipse surface (parallel to the ellipses semi-major axis), the $\pm\delta S_{\theta}$ thresholds as the distance from the foreground chromaticity to the ellipse surface (parallel to the ellipses semi-minor axis). X and Y represent the difference between the $[L-M]$ - and S-cone excitations of the adapting field and foreground ($[L-M]_{\text{for-ada}}$ and $S_{\text{for-ada}}$), respectively. **Page .130.**

Fig. 4.9 (a) and (b) The $+\delta L_{\theta}$ (a) and $-\delta M_{\theta}$ (b) thresholds are shown for detections that correspond to the reddish $+ [L-M]$ direction. **Page .132.**

Fig. 4.10 (a) and (b) The $-\delta L_{\theta}$ (a) and $+\delta M_{\theta}$ (b) thresholds are shown for detections that correspond largely to the greenish $- [L-M]$ direction. **Page .132.**

Fig 4.11(a) and (b) The $-\delta[L-M]_{\theta}$ (a) and $+\delta[L-M]_{\theta}$ (b) thresholds plotted as a function of difference between the adapting field (the background) and the foreground, i.e., $[L-M]_{\text{for-ada}}$. **Page .133.**

Fig. 4.12 Thresholds for the $\pm\delta S$ directions as a function of difference between foreground and background S-excitation. **Page .134.**

Fig. 4.13 The ellipse orientation is given by θ_{ellipse} and the angle between the adaptation point and foreground chromaticity coordinates is given by $\theta_{\text{ada-for}}$. **Page .137.**

Fig. 4.14 The relationship between the measured ellipse angle (θ_{ellipse}) and the angle between the foreground and adapting field angle ($\theta_{\text{ada-for}}$). **Page .138.**

Fig. 4.15 The relationship between the foreground and adapting field angle ($\theta_{\text{ada-for}}$) vs. the measured ellipse angle for a foreground to adapting field angle range of $0 \leq \theta_{\text{ada-for}} \leq 180$. **Page .140.**

Fig. 5.1 The full display ($22^\circ \times 24^\circ$) is shown along with the central $3.3^\circ \times 3.3^\circ$ patch of luminance noise where the moving chromatic stimulus is detected (not to scale). X indicates the thickness of the dark surround. **Page .146.**

Fig 5.2 The white discs plots the chromaticity coordinates of the white adapting background field, the red and blue crosses are the chromaticity coordinates of the red and blue foreground fields and the red and blue discs are the detection thresholds obtained with no border present. **Page .148.**

Fig. 5.3(a) and (b) Threshold sizes (CD) plotted as a function of border thickness for BJ and MRR. The thresholds were measured using reddish adapting background field and foreground. **Page .150.**

5.4(a), (b), (c) and (d) Threshold sizes (CD) plotted as a function of border thickness for BJ and MRR. (a) and (b) are thresholds produced using a combination of white adapting field and red foreground, (c) and (d) are thresholds produced using a combination of white adapting field and red foreground. **Page .151 & 152.**

Fig. 6.1 The weak relationship between peak macular pigment levels vs. the average macular pigment levels over the 2.8° of central vision. **Page .157.**

Fig. 6.2 Variations of fitted ellipse orientations in CIE space as a function of peak macular pigment levels. A non-significant trend exists ($r^2=0.56$, $p=0.054$). **Page .159.**

Fig. 6.3 Variations of fitted ellipse orientations in CIE space as a function of average central 2.8° macular pigment levels. A linear relationship ($r^2=0.67$, $p<0.05$) described by Eq. 6.2 is plotted as the solid black line. **Page .159.**

Fig. 6.4 The series of generated ellipses based on scaled values of the standard CAD observer's semi-major and -minor axes, the standard CAD observer ellipse would fall between ellipse x0.9 and ellipse x1.1. **Page . 161.**

Fig. 6.5(a), (b) and (c) The L-, M- and S-cone contrast curves plotted as a function of CIE angle (θ_{cie}); the greyscale corresponds to the grayscale used in Fig 6.4, for example the largest ellipse in Fig. 6.4 corresponds to the largest S-cone contrasts in Fig 6.4. **Page .162.**

Fig. 6.6 The standard CAD observer ellipse, centered at CIE xy: (0.305, 0.323), is shown at rot:0 i.e., not rotated, the other ellipses are shown rotated relative to this within the range -6° to 6° . **Page .164.**

Fig. 6.7(a), (b) and (c) The L-, M- and S-cone contrast curves contrast curves plotted as a function of CIE angle (θ_{cie}), the greyscale corresponds to the grayscale used in Fig 6.6. **Page .165.**

Fig. 6.8(a) The gradients of the L-cone contrast curve over the greenish colour direction is plotted. No significant relationship exists ($p=0.084$). **Page .167.**

Fig. 6.8(b) The gradients of the M-cone contrast curve over the reddish colour direction is plotted. No significant relationship exists ($p=0.10$). **Page .168.**

Fig 6.9(a) and (b) The significant exponential relationships between $L_{\text{grad_red}}$ and $MP_{2.8^\circ}$ (a) and $M_{\text{grad_green}}$ and $MP_{2.8^\circ}$ (b) are plotted. **Page .169.**

6.10(a), (b) and (c) Cone contrasts calculated with the Stockman-Sharpe (dashed lines) and individually macular pigment adjusted cone spectral sensitivity functions (solid lines) for subjects MOB, SFR and AT, respectively. **Page .173.**

Fig. 6.10(a), (b) and (c) S-cone contrast curves calculated using the Stockman-Sharpe (solid lines) and the individually MP adjusted S-cone spectral sensitivity functions (circles). Note the values of each are almost exactly equal. **Page .175.**

Fig 7.1 A constant pupil diameter is observed as the stimulus field size is varied from 1 to 24° . Reproduced from Atchison *et al.* (2011). **Page .180.**

Fig. 7.2 Pupil diameter a function of luminance level, as the luminance increases the pupil diameter decreases, but for a given luminance the pupil diameter is also dependant on the adapting chromaticity. **Page .184.**

Fig. 7.3 The mean pupil diameters (D_{pupil}) plotted as a function of $\log(\text{Rod excitation})$ ($R^2 = 0.82$, $p<0.05$), the fitted line is given by Equation 7.2. **Page .185.**

Fig. 7.4(a) and (b) The mean pupil diameters (D_{pupil}) plotted as a function of $\log(\text{L-cone excitation})$ ($R^2 = 0.68$, $p<0.05$) in (a) and $\log(\text{M-cone excitation})$ ($R^2 = 0.68$, $p<0.05$) in (b), the fitted lines are given by Equation 7.3 and 7.4, respectively. **Page .186.**

Fig. 7.5 The mean pupil diameters (D_{pupil}) plotted as a function of $\log(\text{Rod excitation})$ ($R^2 = 0.91$, $p<0.05$), the fitted line is given by Equation 7.5. **Page .187.**

Fig. 7.6 The mean pupil diameters (D_{pupil}) plotted as a function of $\log(\text{melanopsin excitation})$ ($R^2=0.63$, $p<0.05$), the fitted line is given by Equation 7.5. **Page .188.**

Fig. 7.7 21 repeated threshold measurements are plotted in CIE xy space for the 20 colour directions tested. The “+” indicates the location of the background and foreground chromaticity. **Page .191.**

Fig. 7.8 The coefficient of variation vs. CIE colour angle for observer BJ. The CoV remains low and independant of colour angle across the whole range. **Page .192.**

Fig 7.9(a) and (b) The L-, M- and S-cone contrasts (plotted as red, green and blue circles, respectively) as a function of cone contrast space angle are shown in (a). The L- and M-cone contrast curves from (a) are plotted alone in (b) for clarity. **Page .193.**

Fig. 7.10 The cone signal-to-noise ratios plotted as a function of cone contrast space colour direction, the mean value (~ 5.6) is indicated by the dashed line, the grey area indicated the 95% confidence interval. **Page .194.**

List of tables

Table. 3.1 Mean and maximum L-, M- and S-cone excitation percentage errors for model predicted increments and decrements in the reddish +[L-M] and yellowish - S directions. **Page .106.**

Table. 4.1 Parameters that represent the four $\pm[L-M]_{\text{for-ada}}$ vs. $\pm\delta[L-M]$ relationships (one per quadrant) shown in Fig 4.6, along with their linear correlation coefficients. **Page .124.**

Table. 4.2 The linear relationships between δS and $S_{\text{for-ada}}$ are outlined for each quadrant of Fig. 4.7, all $ps < 0.05$. **Page .127.**

Table. 4.3 The linear relationships between δS_{θ} and $S_{\text{for-ada}}$ are outlined for each quadrant of Fig. 4.12, all $ps < 0.05$. **Page .134.**

Table. 4.4 A comparison of fitting errors (%) for L-M and S detection in different directions relative to the fitted ellipses. **Page .141.**

Table. 7.1 The CIE xy coordinates of each of the tested chromaticities, the ticks indicate that the chromaticity was reproducible on the CRT display and hence pupil sizes at that chromaticity and luminance level were measured. **Page .183.**

Commonly used symbols and abbreviations

CAD	Colour Assessment and Diagnosis
MAP	Macular Assessment profile
MPOD	Macular Pigment optical density
MP _{peak}	Peak macular pigment optical density
MP _{2.8°}	Mean MP over central 2.8°
[L-M] _{cont}	[L-M]-cone contrast
L _{cont}	L-cone contrast
M _{cont}	M-cone contrast
S _{cont}	S-cone contrast
L _b	L-cone background excitation
M _b	M-cone background excitation
S _b	S-cone background excitation
L _t	L-cone excitation at threshold
M _t	M-cone background at threshold
S _t	S-cone background at threshold
L _{grad_red}	L-cone contrast gradient in the “reddish” direction
L _{grad_green}	L-cone contrast gradient in the “greenish” direction
M _{grad_red}	M-cone contrast gradient in the “reddish” direction
M _{grad_green}	M-cone contrast gradient in the “greenish” direction
a	Ellipse semi-major axis
b	Ellipse semi-minor axis
x ₀	Ellipse centre CIE x-coordinate
y ₀	Ellipse centre CIE y-coordinate
R _t	CIE “red” direction, relative to specified target coordinates
G _t	CIE “green” direction, relative to specified target coordinates
B _t	CIE “blue” direction, relative to specified target coordinates
Y _t	CIE “yellow” direction, relative to specified target coordinates
Q	CIE tristimulus to cone excitation transformation matrix
δL	L _b - L _t
δM	M _b - M _t
δS	S _b - S _t
CIE	Commission internationale de l'éclairage
cd m ⁻²	Candela per meter squared
θ _{ada-for}	Angle subtended between adapting field and foreground

Acknowledgements

I would like thank my two examiners Marisa Rodriguez-Carmona and Sophie Wuerger for making my viva a relatively enjoyable experience and additionally for providing insightful feedback on much of my presented data. Thanks also go to Chris Hull for giving up an afternoon to act as chairperson.

Many thanks go to John Barbur, my primary supervisor, for the long hours of interesting discussions we had covering many aspects of visual perception (and beyond), plus helpful practical advice and general support over the entire PhD. I hope we can collaborate in the future. Also many thanks go to Ted Sharpe, my secondary supervisor, I was a new comer to vision science upon starting my PhD and Ted gave be invaluable one to one tutorials on many aspects of vision and colour, I hope to see you again one day.

Thanks to fellow students and friends Wei, Matilda and Alessandro for almost always maintaining a productive and positive, but also relaxed, atmosphere in the postgraduate office. This work would not be possible without the help of the many observers that participated in hours of psychophysics, I thank all of you, especially MRR for often being the second observer in my $n=2$ experiments.

To Milo and Morgan who arrived during the process; while I cannot say you have supported me in anyway thank you both for being around and mostly keeping me “cheery”. Finally, thanks to Soph for all your support, I love you.

Declaration

I grant powers of discretion to the University library to allow this thesis to be copied in whole or part without further reference to me. This permission covers only single copies made for study purposes, subject to normal conditions of acknowledgement.

Abstract

When the light reflected from an object differs in spectral composition to the surrounding background these spectral differences are reflected in the excitation levels produced in each class of photoreceptor. The ability to see colours and to notice small colour differences is strongly affected by both the spectral composition and luminance level of the adapting light. Knowledge of the limits of colour detection is important in setting safety standards and guidelines in visually-demanding workplaces, as varying conditions of illumination and chromatic adaptation are often encountered in different working environments. It is therefore of both fundamental and practical interest to be able to predict accurately how a human observer's chromatic detection performance changes with both light level and chromatic adaptation. The Colour Assessment and Diagnosis (CAD) test was employed to measure colour detection threshold ellipses under different states of chromatic adaptation and background light levels. The advantage of this new technique is that it isolates the use of colour signals by embedding the isoluminant chromatic stimulus in dynamic luminance noise. These measured threshold variations were analysed in terms of changes in L-, M- and S-cone excitation levels required for threshold in different colour directions. Models based on the measured chromatic threshold data are proposed that are capable of reconstructing entire detection ellipses. These models were based on experiments where observers had colour thresholds measured around a series of different chromatic adaptation points, over a range of light levels (typically from 0.3 to 31 cd m⁻²), and additionally away from the adaptation point. The findings reveal the independent adaptation states of individual cone classes on measured thresholds, i.e., the threshold in a given cone class depends only on the signal produced by the background in that cone class and is independent of the adaptation state of the other cone classes and hence independent of chromaticity and light level. The effect of adapting different areas of the peripheral retina when thresholds are measured foveally was also investigated. No long range retinal interactions were observed. The results show that the adaptation state of the periphery has no effect on colour detection thresholds made in central vision. Variations in L-, M- and S-cone contrasts curves were simulated to assess the influence that detection ellipse size and ellipse orientation have on them. This revealed a correlation between the L-cone contrast curve gradient and the corresponding ellipse orientation. This was additionally shown to correlate with the central 2.8° mean value of macular pigment optical density, hence providing a new method of estimating macular pigment level from colour detection ellipses. Steady state pupil sizes were analysed with the rod and cone excitations that produced them. These data indicate that when chromatically adapted, the steady state pupil size correlates strongest with the S-cone signal, and is independent of the actual chromaticity and luminance levels involved. Cone signal-to-noise ratios were extracted from repeated threshold measurements for a series of colour directions. Analysis of these revealed the existence of a constant signal-to-noise ratios over the full range of colour directions tested relative to a whitish background. The results show that as the cone contrast level increases in a particular cone class so does the associated noise.

Chapter 1

Vision

1.1 Introduction

This chapter introduces the structure of the human eye, the function and connectivity to the brain, the visible light spectrum, the eye's function at varying luminance levels, colour and normal human colour vision.

1.2 The eye

The eye is an organ common to a wide variety of animals, including humans. It has evolved convergently in different forms in a variety of species over a series of isolated locations on Earth (Salvini-Plawen and Mayr, 1977). Its primary purpose is to receive incoming visual information, in the form of light, from the surrounding environment and convert it into a series of electrical signals which can be transmitted to the brain. The brain decodes these signals via a series of hierarchical processes within its visual areas providing a sense of vision; defined as the ability to process and interpret information from the environment based on these incoming light signals.

1.3 The human eye

The normal human has two eyes; they are approximately spheres measuring ~25mm along their anteroposterior axis. The two eyes are located on the front of the head separated with an average pupil-to-pupil distance of ~60mm. The vertical sides of the eye closest to the nose and temple are referred to as nasal and temporal, respectively. Possession of two eyes allows for binocular vision giving humans an enhanced depth perception; compared to single eye (monocular) organisms. The two eyes can fixate (gaze in a certain direction) on the same location within a scene. They can make fast abrupt movements together in a coordinated manner (saccade) and also smoothly track a moving target (smooth pursuit; Barnes (2008)). When fixating (staring) at a location small involuntary eye movements are made (micro-saccades); these are responsible for varying the incoming light signals to each retinal location, this continual variation in stimulation inhibits effects like Troxler's fading (Troxler, 1804), which can occur when the visual system adapts to the part of the scene (visual image) being fixated. Micro-saccades are small and unnoticeable, typically being less than 0.2° of visual angle. Fig. 1.1(a) is a superficial view of a living human's eye embedded in the orbit (the eye socket) of the skull. Fig. 1.1(b) is a sagittal view schematic of the eye, the anatomical structures labelled in Fig. 1.1(b) are described in turn below.

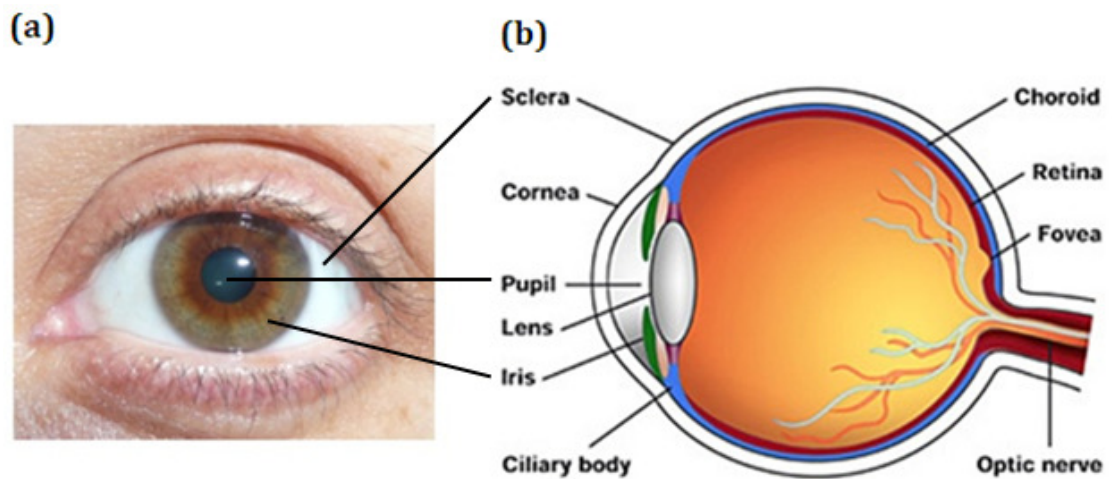


Fig. 1.1(a) and (b)

An anterior external view of a female human's left eye is shown in (a), a sagittal schematic of a human eye is shown in (b), adapted from healthy eyes (2012).

Sclera: The “white” of the eye. This is the outermost layer of the eye; it is composed of collagen and elastin (a connective tissue protein). Its primary purposes are to provide the eye with its semi-rigid approximately spherical topology, provide protection and also to provide secure attachment points for a series of six extraocular muscles. These muscles are used to move the eyes relative to the skull; this, for example, allows for the tracking of a moving target whilst also maintaining a fixed skull position.

Cornea: The cornea is a transparent outer layer of the eye, covering the iris and pupil. It is responsible for contributing ~70% of the eye's optical power (the lens providing the additional ~30%). The cornea, unlike the lens, has a fixed focusing power; the lens and cornea therefore work together with the cornea focusing the majority of incoming light and the lens making small adjustments by fine tuning this mostly focused light. In order to preserve its transparency the cornea does not

contain any blood vessels, instead its oxygen is supplied by the external air supply via the tear film.

Pupil: The pupil is the circular hole in the iris located at its centre; light entering the eye passes through this aperture before projecting on to the retina, therefore its size determines the amount of light reaching the retina. Pupil size can be influenced by a number of factors, three examples are given;

1. The pupillary light reflex, this is an involuntary physiological response that relates to the amount of light entering the eye. Under normal daylight illumination levels the pupil typically has a diameter of ~3 mm, under dark conditions when less light is available the pupil diameter will increase to compensate for the lack of light (up to ~8 mm).
2. Lysergic acid diethylamide (LSD), tends to cause an increase in pupil size relative to the normal size expected under the given lighting conditions, this is due to the pupillary dilator and constrictor muscles receiving activation and inhibiting signals, respectively.
3. Psychological factors, for example over the time course of object recognition pupil sizes have been shown to vary, correlating with the viewing of objects that are familiar and unfamiliar (Ioana *et al.*, 2011). Pupil size has also been shown to be dependent on a variety of other psychological factors such as example emotion (Harrison *et al.*, 2007) and attention (Daniels *et al.*, 2009).

Lens: The lens is a light transmitting convex structure located behind the iris and pupil. The lens is responsible for approximately 30% of the focusing power of the eye (the cornea providing the rest). The lens is elastic and can change shape when the ciliary muscles apply or relax a tension across it. When the lens shape, i.e., its

curvature, is varied its focal length is varied, so by varying the lens shape the eye can focus on near (relaxation of ciliary muscles) or far objects (contraction of ciliary muscles). This adjustment of lens shape is known as accommodation. Over the course of a human life the lens loses some of its transmittance by “yellowing”, this can have an effect on colour vision (discussed later).

Ciliary body: The ciliary body holds the lens in position. It is also responsible for applying a tensional force to the lens causing a change in lens shape and hence a change in optical power, this is the process of accommodation described above.

Iris: The iris surrounds the pupil and is responsible for adjusting the pupil size, in a circular type motion; it does this in response to a number of factors, one being the amount of incident light. The iris achieves this by use of its pupillary dilator and constrictor muscles which have the ability to increase and decrease the pupil size, respectively. Reducing the pupil size decreases the retinal illuminance, while increasing the pupil size increases the retinal illuminance. The iris is commonly coloured brown, green, blue or greyish, this colour is casually referred to as “eye colour”.

Choroid: The choroid is located between the retina and the sclera of the eye. The primary function of the choroid is to supply oxygenated blood to the retina. The choroid is composed of four layers, blood is supplied to the first outermost sub-layer of the choroid via the posterior ciliary arteries, this first layer contains a series of thick blood vessels which supply blood to the second choroid layer, this layer contains a series of smaller blood vessels that in turn supply blood to the third layer which is composed of a network of capillaries. These capillaries supply blood to the fourth (inner most) choroid layer that is known as Bruch's membrane, this provides a blood-retina barrier, but also allows metabolic waste from the

photoreceptors contained in the retina to be absorbed into the choroid layer to be transported away from the eye.

Retina: The retina covers the inner posterior portion of the eye. It is where an image of the external environment is projected; the retina is discussed in detail later in the chapter.

Optic nerve: The optic nerve connects the eye and brain, it transmits signals from ganglion cells from the retina directly to the brain. The point at which the optic nerve attaches to the retina is known as the blind spot, this is due to the absence of photoreceptors in this retinal region.

Fovea: The fovea is the ~1.5 mm (diameter) cone cell rich region of the retina, responsible for high acuity central vision; it is the region where colour sensitivity is greatest, due to this high concentration of cones and an almost complete absence of rods. The fovea is located within the macula lutea region of the retina - the yellow pigmented region close to the centre of the retina.

1.4 Connection to the brain

The eye, and more specifically the retina, is connected to the brain's primary visual area (the visual cortex) via the optic nerve, lateral geniculate nucleus (LGN) and a series of fibrous tracts known as the optic radiation, Fig. 1.2 illustrates these.

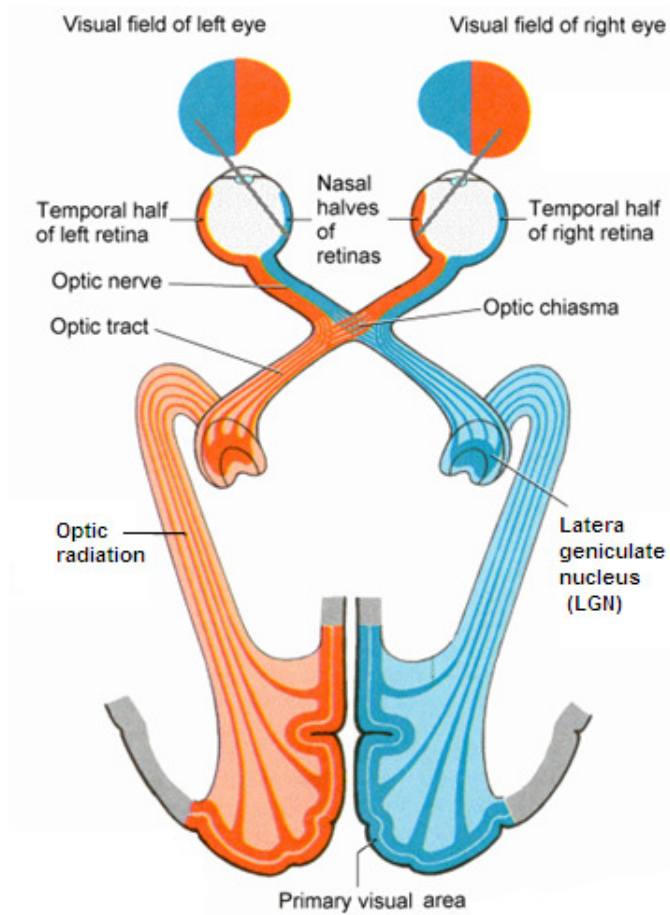


Fig. 1.2

A transverse slice through the series of physical connections from the eye to the primary visual area is illustrated. Image modified from Young (2007).

The retina is connected directly to the optic nerve via retinal ganglion cell axons, at the point of the blind spot, the optic nerve transmits its incoming visual signals to the optic chiasm, preserving information regarding their origin, i.e., the retinal location they originated from. The optic chiasm is located under the hypothalamus and at this point the retinal signals are split and transmitted to one of two different brain areas, either the right or left cerebral hemispheres. Information from the nasal halves of the retinas swap sides, being transmitted to the LGNs on the opposite side of the brain relative to their origin, referred to as contralateral. Visual information in the optic nerve from the temporal halves of the retinas do

not cross each other at the optic chiasm, remaining on the side they originated from, referred to as ipsilateral. This results in information from the right side of the visual field, on both eyes, being processed by the same side of the brain and the information from the left side of the visual field, of both eyes, to also be processed in the same side of the brain; this is illustrated by the blue and orange colour coding of Fig. 1.2. Beyond the optic chiasm the optic nerves become optic tracts. They transmit their incoming visual information into the thalamus where they are input into their corresponding lateral geniculate nuclei (LGN). The LGN is divided into six internal layers, the lower layers (1 and 2) are the magnocellular layers and the higher layers (3, 4, 5 and 6) are the parvocellular layers. A sublayer is also present known as the koniocellular layer. The cell types found in the LGN are discussed later. The LGN outputs a series of signals via interneurons (neurons that connect different neuron types together) along the geniculo-calcarine tract, this connects to the primary visual area within the occipital region of the brain where higher order visual processes occur. For example, in order to create a coherent representation of our visual environment the incoming visual information, i.e., a visual image of that environment, is segmenting through a series of rapid hierarchical stages. This takes place first at a lower level where, for example, visual mechanisms extract contours and edges (Mullen *et al.*, 2000) then figure-background organisation is performed (Xiaofeng *et al.*, 2006). These lower level processes are succeeded by high-level processes that can be dependent on, for example, memory access or semantic input in the case of object recognition (Martinovic *et al.*, 2011).

1.5 Photoreceptors

Photoreceptors are a class of neuron located in the retina. The pigment contained in photoreceptors absorbs photons from the external environment, and the energy of these photons is converted into a physiological electrical response via a membrane voltage change. There are two types of photoreceptor present in the retina of a normal human eye; rods and cones.

1.5.1 Rods

Rod cells are a type of photoreceptor. There are approximately 9×10^6 rods in a typical human retina (Curcio and Sloan, 1990). Rod cells are sparse in the central fovea, but found in high densities within the periphery of the retina. Under normal daylight lighting levels the rods saturate and are rendered visually inactive, under these conditions the cone system is relied on. Humans rely on rod cells for night vision, under dark conditions the cones are not sufficiently sensitive enough to be excited, also under intermediate (mesopic) conditions the rods are simultaneously active with the cone system. The anatomy of a rod cell is shown in Fig. 1.3. Rods and cones both contain an inner segment, an outer segment and synaptic ending. The synaptic ending creates a synapse to other retinal cells. Rods are narrower than cones with a cross section of approximately constant size. The outer segment consists of a series of closely layered discs, composed of the cell's membrane that is externally covered in rhodopsin, a photon absorbing photopigment. The inner segment contains the cell's nucleus; this contains the cell's genetic information in the form of deoxyribonucleic acid (DNA). The rods are orientated so that the outer

segment, containing the high concentration of rhodopsin, is located closest to the posterior of the retina.

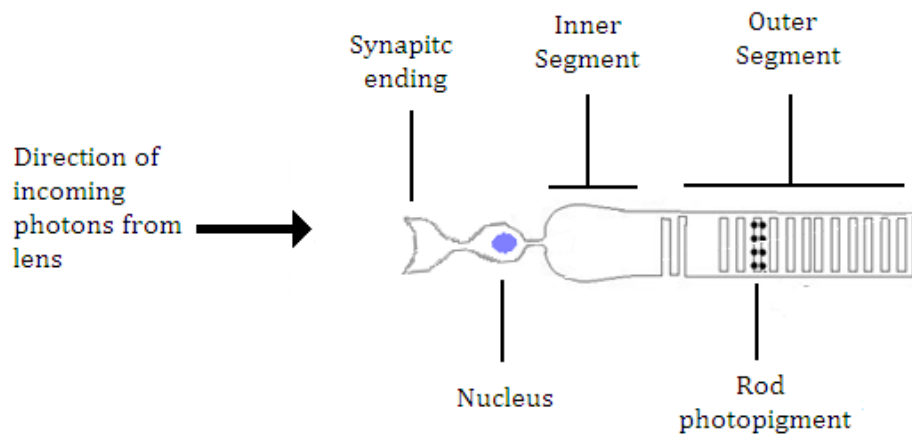


Fig. 1.3

A rod cell oriented relative to the direction of incoming photons. Diagram adapted from Heeger (2012)

1.5.2 Cones

Cone cells are a type of photoreceptor found in the retina. There are approximately 4.5×10^6 cone cells in the normal human retina (Curcio *et al.*, 1990). Cones are not as photosensitive as rods and hence not active in dark conditions, but are active under higher lighting conditions and responsible for colour vision. They are also responsible for high acuity in central vision, i.e., the ability to perceive fine detail. The anatomy of a cone cell is shown in Fig. 1.4, it is similar in structure to a rod cell (Fig. 1.3), but possessing a varying cross-sectional size. As with rods, cones are composed of an inner and outer segment and a synaptic ending which creates a synapse with other retinal cell types. Cones have a narrower outer segment compared to their inner segment, i.e., they are literally

cone shaped. The outer segment consists of a series of closely layered discs composed of cell membrane; these are externally covered in absorbing photopigment. The inner segment contains the cell's nucleus, which contains the cell's genetic information in the form of DNA. Like the rods, the cones are orientated so that their outer segment, containing the high concentration of photopigment, is located closest to the posterior of the retina. The cones are directionally sensitive to incoming photons; photons entering the pupil close to any part of its edge are less likely to be absorbed by a photoreceptor compared with photons entering the eye through the centre of the pupil, this is known as the Stiles-Crawford effect of the first kind (Stiles and Crawford, 1933) and accounts for reduced photon scattering at high light levels (Smith and Atchison, 1997).

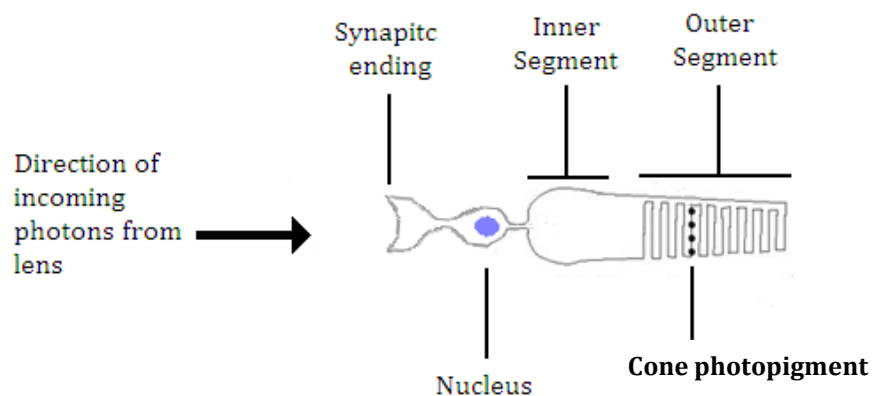


Fig. 1.4

*A cone cell oriented relative to the direction of incoming photons.
Diagram adapted from Heeger (2012).*

A normal human retina contains three types of cone cell that are sensitive to photons over three different, but partly overlapping wavelength ranges, thus making these individuals normal trichromats. The three types of cone cell are sensitive to either the long, medium or short wavelength regions of the visible

spectrum and are named L-, M- and S-cones, respectively. These sensitivity curves can be considered as a set of probability distributions that indicate the likelihood that an incoming photon of a particular wavelength (λ) will be absorbed by a particular cone type if it hits it. It is important to note that when a photon is absorbed by any cone type no information regarding its wavelength is transferred to the cone cell, just an absorption is registered. Fig. 1.5 plots the spectral sensitivities (also referred to as cone fundamentals) of the L-, M- and S-cones as a function of wavelength over visible spectrum ($\sim 390 \leq \lambda \leq 830$ nm) as measured by Stockman and Sharpe (1999; 2000). It is a common convention to plot the L-, M- and S-cones as red, green and blue curves, respectively, corresponding very approximately to the regions of the spectrum in which their peak sensitivity occurs. The peaks of the L-, M- and S-cone fundamentals are located at $\lambda = 570$, 543 and 442 nm, respectively, corresponding in reality to yellowish-greenish, greenish and violet chromaticities, respectively (these values are derived from tabulated data of the Stockman-Sharpe 2° fundamentals in 1nm stepsizes, see later). The L- and M-cones are sensitive over the whole $390 \leq \lambda \leq 830$ nm range, but are most sensitive at, and around, their peak values, with sensitivity tending to zero at the extreme ends of the spectrum; their peak values occur relatively close to together, with a mean separation across individuals of only ~ 30 nm. The S-cones are only sensitive over a range of lower wavelengths, Stockman-Sharpe only provide sensitivity data for S-cones in the range $390 \leq \lambda \leq 615$ nm, see the blue curve of Fig. 1.5.

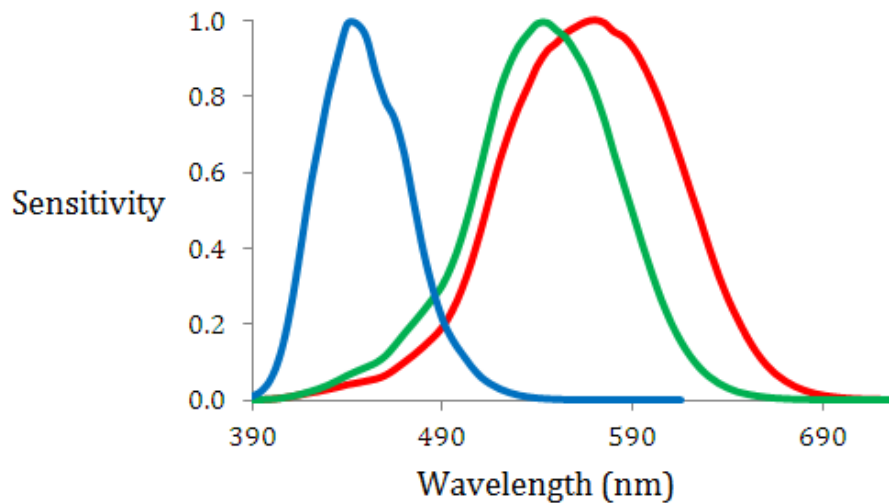


Fig. 1.5

The 2° Stockman-Sharpe cone fundamentals. The data were obtained from the Institute of Ophthalmology (University of London) Colour & Vision Research Laboratory (cvrl.org, accessed July 2011), the data was plotted using the 1nm step size option provided by the CVRL database.

Some humans have retinas containing more or fewer than the standard three L-, M- and S-cone types. For example, tetrachromats have four cone types (Jordan *et al.*, 2010) and colour defective humans may have two or fewer (McIntyre, 2002). Interestingly, having only two cone types has been shown to be advantageous under some conditions (Morgan *et al.*, 1992). The experiments reported later in this thesis were all performed using only normal trichromatic observers.

1.6 The retinal distribution of rods and cones and the cone

The distribution of rods and cones is not homogeneous over the retina which has consequences for both colour and night vision. Fig. 1.6 shows the distribution of rods and cones as a function of retinal eccentricity. In the fovea cone cells have a diameter in the range 1 to 4 μm (rod cells have a diameter of $\sim 1 \mu\text{m}$). The central

2° is the cone rich region, containing very few or no rods, the number of cones peaks at around 170×10^3 per mm^2 within this region, this density rapidly reduces with increasing eccentricity in all directions. Fig. 1.6 illustrates this in both the nasal and temporal directions. Conversely the number of rods rapidly increases with increasing eccentricity, peaking at $\sim 12^\circ$ with a value of $\sim 150 \times 10^3$ per mm^2 , this value then decreases out into the far periphery. In the nasal direction between $\sim 13 - 18^\circ$ there is a region that is absent in both rods and cones, this is known as the optic disc, i.e., where the optic nerve connects to the retina.

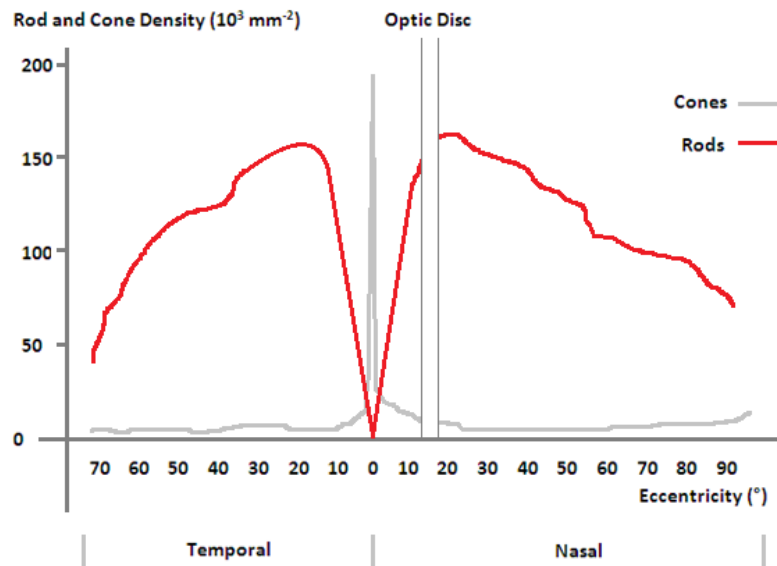


Fig. 1.6

The distribution of rods and cones as a function of eccentricity in the temporal and nasal direction. The area over the optic disc has a complete absence of rods and cones.

Within the central 2° foveal region of the retina the distribution of L-, M- and S-cones, within the cone mosaic is typically as follows; there is a complete absence of S-cones within the central 0.2 - 0.3° (Williams *et al.*, 1981), at higher eccentricities the S-cones are distributed occurring singularly but isotropically. The L- and M-cones both occur locally in clusters of the same cone type; these clusters of L- and M-cones are in turn distributed randomly on a global scale, this arrangement of

photoreceptors is known as the cone mosaic. Fig. 1.7 shows the arrangement of L-, M- and S-cones in the cone mosaic. S-cones, as described above, are sparse and on average accounting for only ~7% of all cones. The ratio of L/M cones has been measured *in vivo* using a variety of techniques (Krauskopf and Carroll, 2007) and found to vary over the relatively large range $1.1 \leq L/M \leq 16.5$ (Hofer *et al.*, 2005). On average the L/M ratio has been found to be at the lower end of this range at around ~2. Subjects with both very low and very high measured L/M ratios have been shown to also possess normal colour vision, indicating colour is not wholly dependent on the individual's L/M ratio. It has, however, also been demonstrated that humans with a symmetrical L/M ratio, i.e., $L/M = 1$, possess the highest chromatic contrast sensitivity (Gunther and Dobkins, 2002).

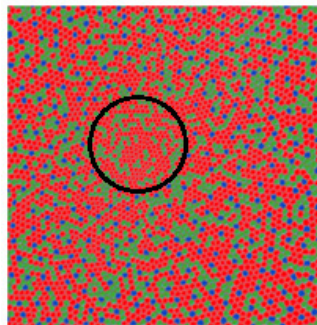


Fig. 1.7

The central ($\sim 1^\circ$) region of the normal human cone mosaic showing the arrangement of the L- (shown in red), M- (shown in green) and S-cones (shown in blue). S-cones are typically absent from the central $0.2 - 0.3^\circ$ (indicated by the black circle). Image adapted from Gegenfurtner and Sharpe (2000).

1.7 Other retinal cell types

Along with rod and cone cells there are many other varieties of non-photosensitive cells in the retina. They will be introduced in turn in the following sections.

1.7.1 Ganglion cells (RGCs)

The retinal ganglion cells (RGC) are located on the inner surface of the retina. They receive incoming information from the rod and cone photoreceptors via the bipolar and amacrine cells (see later). Retinal ganglion cells transmit incoming visual and non-visual information from the retina to various regions of the brain, for example the thalamus. RGCs vary with respect to their individual responses to incoming signals, but each RGC has a nerve fibre ending (axon) that collate and ultimately form the optic nerve, chiasm and tract, and hence provide a direct connection to the brain. The ratio of RGC to photoreceptors in the normal retina is ~100:1, one RGC on average receives input from ~100 rods and cones, however this value varies significantly as a function of retinal eccentricity. In the fovea, single RGCs can receive inputs from as few as five photoreceptors, whereas at high eccentricities in the periphery a RGC can have connections allowing input signals from more than 2000 photoreceptors to be received. The number of photoreceptor-RGC connections also has significant variation throughout the normal population. When at rest RGC have a certain base level firing rate, i.e., they have a non-zero action potential, when excited or inhibited an increase or decrease in the firing rate is observed, respectively.

1.7.2 Photosensitive retinal ganglion cells

Photosensitive Retinal Ganglion Cells (pRGC) represent ~3% of all ganglion cells found in the retina, they contain the photopigment Melanopsin and are dissimilar

to other ganglion cells found in the retina as they can be stimulated by photons but do not contribute to vision. They serve two main purposes;

1. they assist in the synchronisation of the circadian clock, with a period of ~24 hours, and
2. their output signal may also be used to control the pupillary light reflex.

1.7.3 Amacrine cells

The interneurons connecting the photoreceptors to the RGCs are the Amacrine cells, which contribute ~75% of input to the RGC with the bipolar cells (see below) providing the additional ~25%. They are located at the second synaptic retinal layer where bipolar cells synapse with RGCs. Similarly to the horizontal (see later), amacrine cells operate laterally affecting the outputs from the bipolar cells. There are ~40 types of amacrine cell with specialised tasks. Each type of amacrine cell connects with a particular type of bipolar cell, and in general uses a particular neurotransmitter, for example gamma-Aminobutyric acid (GABA). Amacrine cells supplement the function of the horizontal cells by contributing feedback to inhibitory surrounds to both the bipolar cell and RGCs. The “Rod amacrine cell” mediates the input signals from the rods under low light level conditions.

1.7.4 Bipolar cells

Within the retina the bipolar cells are located between the photoreceptors and RGCs, their primary function is to transmit signals from the photoreceptors to the RGCs. Bipolar cells can form synapses with only one type of photoreceptor per cell,

but are also able to receive incoming signals from the horizontal cells. The bipolar cells transmit these incoming signals to the RGCs either via a direct connection or via the amacrine cells. There is one particular type of bipolar cell that is able to connect directly to a rod cell, in addition to this there are approximately ten other bipolar cell subtypes. Under dark viewing conditions a photoreceptor cell will inhibit an ON bipolar cell and excite an OFF bipolar cell. Rod bipolar cells do not synapse with RGC directly, instead they synapse with the amacrine cells, which are able to excite ON bipolar cells and inhibit OFF bipolar cells. This allows the rods to transmit signals to the RGCs under low light level conditions. The OFF and ON bipolar cells synapse within the outer edge of the inner plexiform layer (see Fig 1.8) and the inner layer of the inner plexiform layer, respectively.

1.7.5 Horizontal cells

Horizontal cells are located in the outer plexiform layer of the retina and laterally connect neurons. They assist in the regulation of photoreceptor cell signals which allows the retina to adjust its sensitivity when external lighting levels change. There are three types of horizontal cell, some studies have shown a preference for these three horizontal cell types to be associated with a particular L-, M- or S-cone type, whilst other studies have shown no preference (Kolb *et al.*, 1994). The horizontal cells sum incoming signals from the cones and, based on these signals, regulate the amount of GABA that is required to be released back into the cone system, hence inducing hyperpolarisation within them. The horizontal cell (known as type II) can also receive incoming information from the rods.

1.8 Retinal layers

The different cell types introduced in the previous sections are present in the retina which is structured as follows (see Fig. 1.8); the pigment epithelium forms the outer edge of the retina and contacts the choroid, the choroid supplies the pigment epithelium with oxygenated blood and nutrients, for example, omega-3 acids and glucose, these in turn pass on to the retinal cells via the pigment epithelium. The pigment epithelium is also responsible for shielding the retina from excess incoming light. Next to the outermost pigment epithelium in the retina are the rod and cone photoreceptors, these form connections to the horizontal and bipolar cells at the outer plexiform layer. The bipolar cells connect with the RGCs at the inner plexiform layer, where amacrine cells also form interconnections across this interface. The output axons from the RGCs form a layer of nerve fibers that eventually converge forming the optic nerve which connects the retina to the brain.

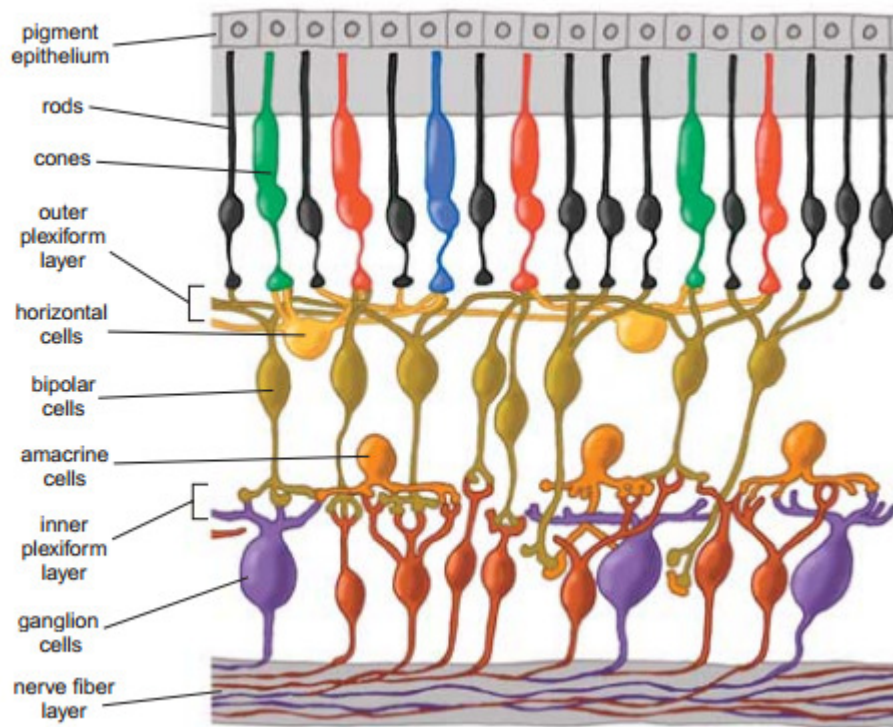


Fig. 1.8

A cross section of the retina, the structure and organisation of the different cell types are shown. Within this figure light would be entering through the pupil located at the bottom of the diagram, reaching the rods and cone lastly after all other cells. Image reproduced from American Scientist (Jan/Feb 2003).

1.9 The lateral geniculate nucleus

The two lateral geniculate nuclei (LGN) are located within the thalamus of the brain, its primary function is to relay the incoming visual signals it receives from the retina to higher brain areas via the optic radiation which connects the LGN to the primary visual cortex (V1). Humans have two pathways connecting the eye to the brain; they are the dorsal section of the LGN and the superior colliculus (SC). The LGN is organised into a series of six layers, the magnocellular (M cells), parvocellular (P cells) and koniocellular (K cells) pathways connect within and between these layers. The parvocellular pathway connects with LGN layers 3, 4, 5

and 6, they provide inputs from the L- and M-cones and are responsible for processing the reddish-greenish opponent pathway. The koniocellular cells layer themselves between the M and P cells; they receive input signals from the S-cones and are responsible for processing the bluish-yellowish opponent pathway. The signals that leave the LGN are input into different layers of the visual cortex; the signals from the magnocellular layers (1 and 2) and the parvocellular layers (3, 4, 5 and 6) are input into layer 4 of V1. This layer is subdivided with one section of it receiving the parvocellular input signal while another sub-section receives the magnocellular input signals. The koniocellular layers send their output signals to layer 4a in V1, while layer 6 of V1 feeds back into the LGN. The LGN also makes connections into higher visual areas, for example V2 and V3. This has been verified in blindsight studies using observers with lesions located in their visual cortex (Schmid *et al.*, 2010).

1.10 Electromagnetic radiation

Electromagnetic radiation is a form of energy; the energy is carried by particles, known as photons. The wavelength of these photons defines where on the electromagnetic spectrum the photons lie; a small portion of the electromagnetic spectrum contains photons that are visible to human observers, commonly referred to as visible light.

1.10.1 Photons

Electromagnetic radiation is composed of photons. These have an invariant mass of zero, a neutral charge and are considered stable in terms of particle decay. Photons can be emitted, for example, by a laser (as visible light) or a Computer Tomography (CT) scanner (in the form of X-rays). Photons can be absorbed, for example, by a living plant via the process of photosynthesis or by a photosensitive cell in an animal's eye. Photons can be reflected, this can occur when there is an abrupt change in refractive index between two mediums the photons are travelling through. For example, when a photon is travelling through air and incident onto glass the change in refractive index at the air-glass interface can cause some proportion of the incident photons to be reflected back into medium they came from. In this air-glass example some of the non-reflected photons will travel through the glass, this proportion of photons defines the transmittance of the glass, some non-reflected photons will also be absorbed the glass, the ratio of these to the total number of incident photons defines the absorption of the glass. A surface can be considered a Lambertian surface if the photons are reflected from it uniformly in all directions, that is, the light is reflected by the surface in such a way that the apparent brightness of the surface is independent of the observers viewing position.

1.10.2 Electromagnetic wavelength and frequency

An electromagnetic wave can be considered to have both wave-like and particle-like properties. Choosing when to consider photons as particles or waves is based largely on the context they are being examined in. For example when considering

electromagnetic radiation being detected by absorptions in a geiger-müller tube's sensor it makes most sense to consider them as particles. Wavelength, a measure of distance, is a commonly used parameter in vision science to describe visible light. Fig. 1.9(a) shows the whole electromagnetic spectrum in terms of wavelength (λ), illustrating the portion that is visible to humans, approximately the range $400 < \lambda < 700\text{nm}$. Fig. 1.9(b, inset) illustrates a sinusoidal wave indicating its wavelength.

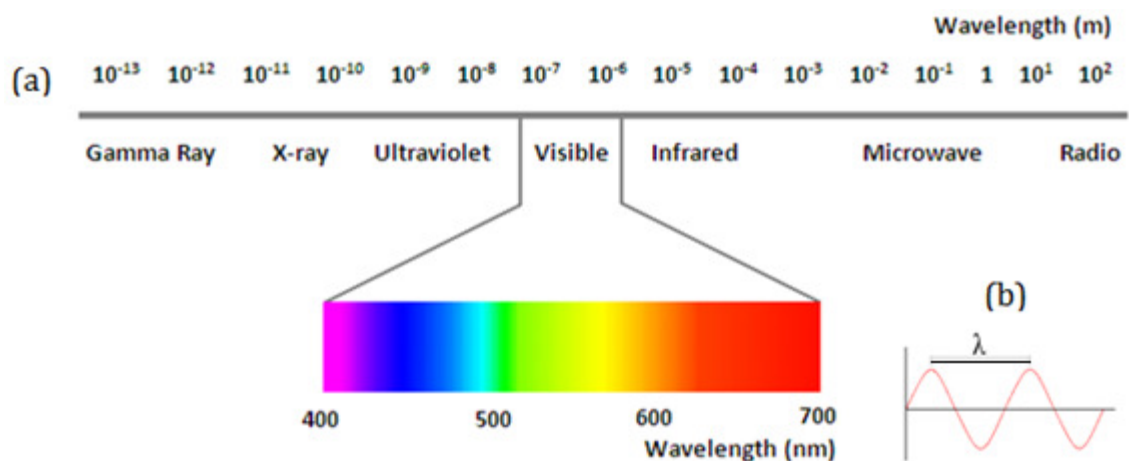


Fig. 1.9(a) and (b)

The electromagnetic spectrum (a), the visible region between ~ 400 and $\sim 700\text{nm}$ is shown expanded. A sinusoidal wave is shown in (b), one wavelength λ is indicated by the black horizontal bar.

It is important to note in Fig. 1.9(a) that as wavelength increases (from left to right) the frequency decreases. Frequency (f) is defined as the number of wavelengths per second, the common unit of which is the Hertz (where; $1 \text{ Hz} \equiv 1 \text{ cycles s}^{-1}$).

1.10.3 Photon speed and energy

All electromagnetic radiation travels with an equal speed, independent of its wavelength and hence its frequency. This speed is commonly referred to as the 'speed of light' (c); its value through a vacuum is $2.998 \times 10^8 \text{ m s}^{-1}$. This constant wave speed (light speed) is defined by the electromagnetic radiation wavelength and frequency (Eq. 1.1). The energy of a photon (E_p) is defined by Eq. 1.2, the energy can be calculated as a function of frequency or wavelength, the constant term (h) is Planck's constant ($h = 6.626 \times 10^{-34} \text{ m}^2 \text{ kg s}^{-1}$).

$$c = f \lambda = 2.998 \times 10^8 \text{ m s}^{-1} \quad \text{Eq. 1.1}$$

$$E_p = \frac{h c}{\lambda} = h f \quad \text{Eq. 1.2}$$

1.11 Luminance and retinal illuminance

Luminance (L) is a photometric measure of the amount of luminous intensity per unit area. Luminous intensity (I_v) is the power of the photons emitted per unit of solid angle; it is scaled by the luminosity efficiency function (see later) and hence takes into account the sensitivity function of the human eye. The unit of luminous intensity is the candela (cd); luminance is the luminous intensity per unit area and measured in cd m^{-2} . The retinal illuminance is defined by Eq. 1.3; where, L is the stimulus luminance level expressed in cd m^{-2} and P_{area} is the area of the pupil expressed in mm^2 . Retinal illuminance values are given in units of Trolands. Retinal illuminances, even under non-extreme light levels, span a large range they are therefore commonly quoted using the units of $\log_{10}(\text{Trolands})$.

$$R_i = L P_{\text{area}} \quad \text{Eq. 1.3}$$

1.12 Contrast

Contrast is the difference between the signal, e.g., a luminance, produced by a target (t) relative to its surroundings or background (bg). Three common definitions of contrast exist;

Weber contrast (C_{Weber}): Described by Eq. 1.4, where I_t and I_{bg} are the luminance levels of the target and background, respectively. Weber contrast is commonly used to describe the contrasts of small targets against large background surrounds.

Michelson contrast (C_{Mich}): Described by Eq. 1.5, where I_{max} and I_{min} are the highest and lowest luminance levels, respectively. Michelson contrast is commonly used to describe the contrast of large areas of differing luminance bordering each other.

Root mean square (C_{RMS}): Described by Eq. 1.6, this contrast type used to describe the contrast over a whole scene and is independent of the spatial frequency distributions within any visual scene. C_{RMS} contrast is defined as the sum of the standard deviations of each pixel's intensity over the whole scene, in the case of Eq. 1.6 the scene is assumed to be a rectangular image of area $A = ab$. The values of x and y are the x- and y-coordinates of each pixel in the image, the pixel intensities are in the range $0 \leq I \leq 1$ and have a mean value of \bar{I} .

$$C_{Weber} = \frac{I_t - I_{bg}}{I_{bg}} \quad \text{Eq. 1.4}$$

$$C_{Mich} = \frac{I_{max} - I_{min}}{I_{max} + I_{min}} \quad \text{Eq. 1.5}$$

$$C_{RMS} = \sqrt{\frac{1}{ab} \sum_{x=0}^{a-1} \sum_{y=0}^{b-1} (I_{xy} - \bar{I})^2} \quad \text{Eq. 1.6}$$

Contrast known as cone contrast, can be calculated individually for each cone type and then if desired combined into the total contrast for a given chromatic pathway, this is discussed in detail in chapter 2.

1.13 Sensitivity over various light levels

The human eye can be sensitive to light over a wide range of light levels (Boff *et al.*, 1986), this range is so large it is commonly plotted in log units, the range (base 10 log units) is illustrated in Fig. 1.10; this figure also shows the photopic and scotopic (see later) retinal illuminances corresponding to these light levels, where within these ranges the rods and cones are active, the active mode of vision (scotopic, mesopic or photopic), how visual acuity and colour vision vary over the range and also some examples of typical conditions when these light levels are present. Although the eye is safely capable of light detection that provides functional vision over a range of ~9 log units, in practice the eye is sensitive to an ~2 log unit “window” within this range at any given time, the light response of the eye is required to adapt when lighting conditions change (see later).

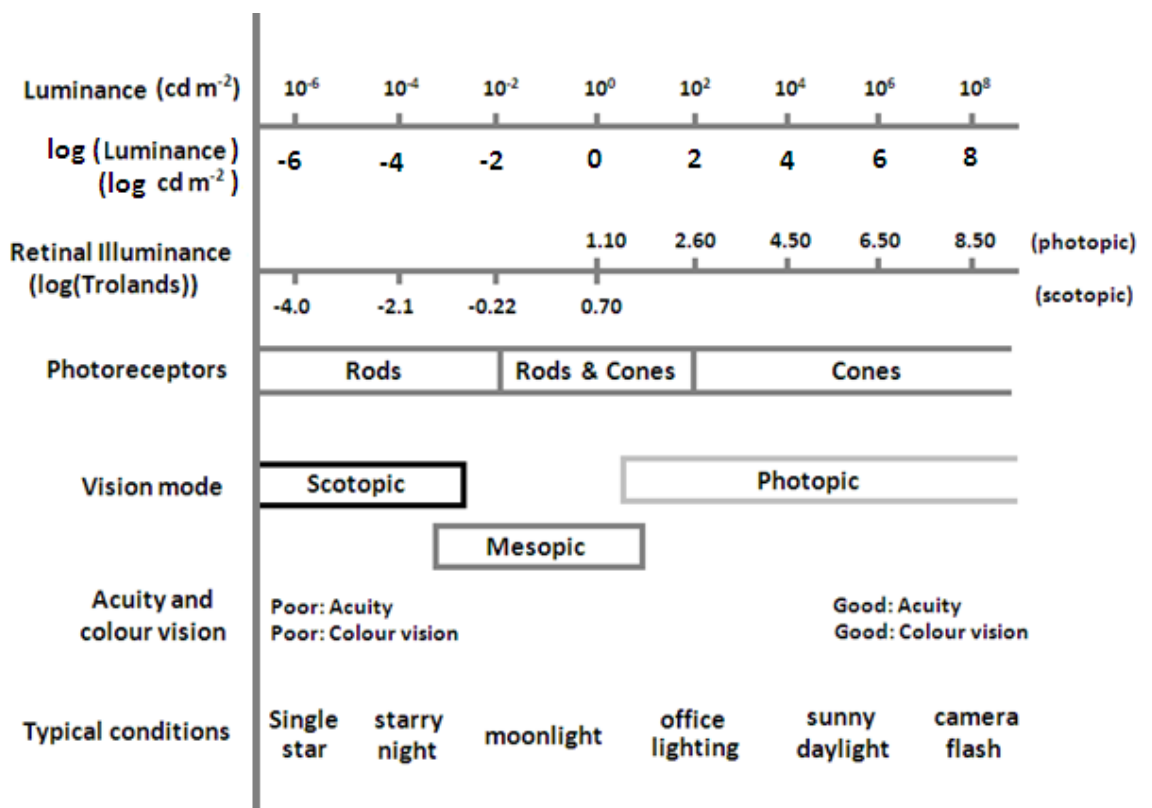


Fig. 1.10

Various properties of the human visual system as a functions of each other. Modified from Sacek (2006).

1.13.1 Photopic vision

Photopic vision is a mode of vision that utilises only the cone signals and occurs under conditions involving high light levels; all three cone types (L-, M and S-cones) are involved whilst the rods are not due to them being saturated. As photopic vision is only dependant on the cone system colour perception is good, as is sensitivity to high spatial frequencies, i.e., high visual acuity. There is a risk of damage if the retina is exposed to luminance levels greater than 10^8 cd m^{-2} for even short periods of time, for example solar maculopathy due to sunlight damage can occur (Arda, *et al.*, 2006) which may lead to a reduction in visual acuity (Kallmark and Ygge, 2005).

1.13.2 Scotopic vision

Scotopic vision is a mode of vision occurring at very low light levels, from $\sim 10^{-2}$ down to $\sim 10^{-6}$ cd m⁻²; these light levels correspond to the light level produced by a starry night sky down to the light level observed from a single star, respectively. Scotopic vision relies only on signals from rod cells; rod photoreceptors are ~ 100 x more sensitive to a single photon than cone cells (Okawa and Alapakkam, 2007). Under scotopic conditions the number of photons is insufficient to stimulate the cone system, so it remains inactive, hence under scotopic conditions an observer has no colour vision. An observer will experience very poor visual acuity due to the rods not being sensitive to high spatial frequencies. Rods are not present (or there are very few) in the central $\sim 2^\circ$ cone rich region of the fovea; therefore all aspects of vision under low scotopic lighting conditions are very poor to non-existent in the central visual field.

1.13.3 Mesopic vision

Mesopic vision is a combination of both photopic and scotopic vision bridging the gap between the photopic/scotopic (cone/rod) transitions. It occurs over the range $\sim 10^{-2}$ and ~ 3 cd m⁻²; these light levels correspond to low lighting conditions that are only slightly above dark conditions, they are often referred to as “twilight” (Stockman and Sharpe, 2006; Connolly, 2011). The mesopic vision mode is mediated by both the rod and cone systems; the lower light input to the cone system causes a reduction in colour sensitivity, but unlike scotopic vision, some colour perception is retained (Walkey *et al.*, 2005).

1.13.4 Purkinje shift

During the process of changing scene illumination conditions from high to lower light levels, the photoreceptors peak sensitivity shifts from the greenish/yellowish portion of the visible spectrum toward the low wavelength bluish region – this is known as the Purkinje effect/shift. This adaptation results in a difference in colour appearance; Fig. 1.11(a) and (b) simulates this shift. Under high luminance conditions, for example daytime skylight (photopic) illumination, blue bell flowers appear to be bright with a bluish/violet colour (Fig. 1.11(a)), but under evening twilight conditions (mesopic) with shift in sensitivity towards the blue end of the spectrum, they appear to have a more intensely saturated bluish/violet chromaticity (Fig. 1.11(b)).

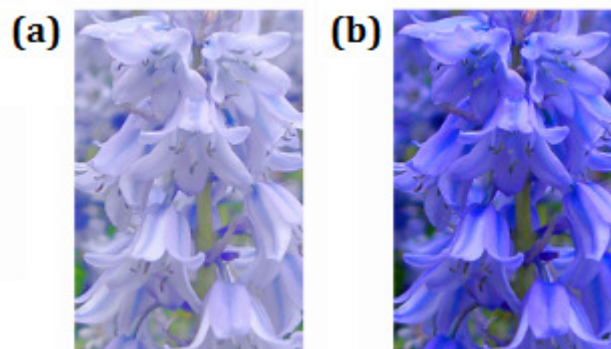


Fig. 1.11(a) and (b)

Blue bell flowers illuminated under daytime blue skylight (a) and evening twilight (b), the shift from (a) to (b) corresponds to a more intensely saturated bluish/violet colour being perceived.

This shift is due to the cones having their maximum sensitivity peak around the yellow region of the spectrum, but the rods having their peak sensitivity around the greenish/bluish region. The rods are more sensitive under low light conditions than the cones, but they do not contribute to colour perception, this accounts for a

colour normal observer's loss of colour perception as illumination levels within a scene decrease. The Purkinje effect occurs within the transition from cone-based photopic to rod-only scotopic vision, i.e., it occurs within the mesopic region when both cones and rods are active and contributing towards the visual image.

1.14 Luminosity efficiency function

The luminous efficiency function plots the mean photosensitivity of the photoreceptors (as expected under specified light level conditions) as a function of wavelength. The most recent estimate of the luminosity efficiency function (for daylight adapted conditions) is the $V^*(\lambda)$ function proposed by Sharpe *et al.* (2005), derived from the results of a series of flicker photometry experiments; it is plotted in Fig. 1.12. The original CIE 1924 $V(\lambda)$ function had been previously updated by Judd (1951) and then by Vos (1978); Vos made corrections to Judd's 1951 revision via an update to the 2^o CIE 1931 colour matching functions. Both the Judd and Vos modified $V(\lambda)$ functions result reflect an overestimate of the mean macular pigment optical density (MPOD) and this can result in elevated sensitivities in the low wavelength, bluish region of the visible spectrum being assumed; the $V^*(\lambda)$ corrects this overestimation. The $V^*(\lambda)$ is also scaled to the proportion of serine L(ser180) and alanine L(ala180) genotypes present in the population. For the 40 observers tested by Stockman and Sharpe 22 had the serine, 16 had alanine variant and 2 had both variants of the L-cone photopigment.

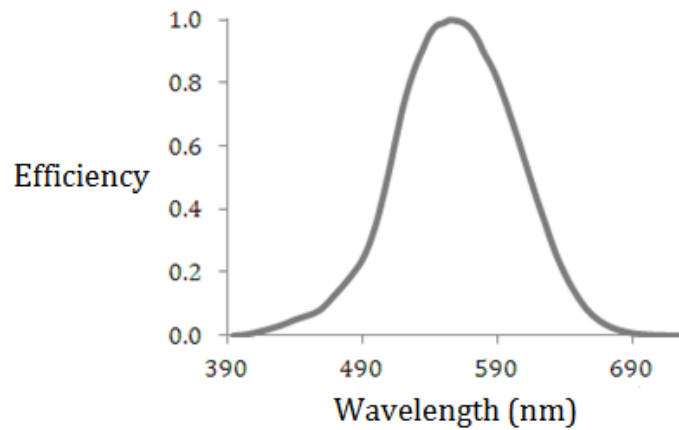


Fig. 1.12

The $V^(\lambda)$ function plotted over the visible spectrum. Data from CVRL database tabulated data in 1nm stepsizes.*

1.15 Colour

Colour is a visual perceptual property which is derived largely from the spectral distribution of incoming visible light that interacts with the photosensitive cells of the retina (rods and cones). The perception of colour can be greatly altered by changing the viewing conditions such as the light level or the surrounding colour relative to a target colour. The cells of the retina themselves can adapt to changes in viewing condition, which in turn can result in different colour percepts being experienced by the viewer. Colour can be measured using optical equipment (a spectroradiometer) and described mathematically in terms of coordinates in various colour spaces. These colour spaces can represent colour as pure radiometric quantities or take into account human physiology, for example the DKL space (Derrington *et al.*, 1984) represents colour in terms of the chromatic and luminance pathways. However, these colour spaces do not however fully explain colour appearance, that is, the perception of a particular colour to an observer.

1.15.1 Hue, brightness and saturation

A given colour can be described by the following three parameters or properties; the hue, brightness and saturation. Hue refers to what has traditionally been thought of as the “actual colour”, it can be described by casual naming a colour, for example, red, pink, etc, or formally within a colour space, for example with the colour angle parameter of the DKL colour space. Brightness is the perceived luminance of a colour. Saturation is a measure of the colourfulness (or intensity of a colour), for example in the CIE 1931 colours located towards the edge of the diagram (near to or on the locus) have a higher saturation than colours of a similar hue located towards the centre of the diagram. The cylindrical HSV colour space allows for visualisation of the relationship between these quantities. The H, S and V correspond to hue, saturation and value, respectively (value corresponds to the brightness as described above). Fig. 1.13 show the hue varying as the colour angle varies, for example, a greenish hue can be described with an angle of $\sim 120^\circ$, the saturation increases as the length of the vector from the central axis of the cylinder increases and the brightness (value) increases along the length of the cylinder from its base upwards.

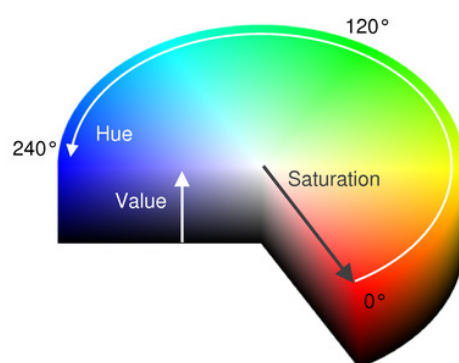


Fig. 1.13

The HVL colour space relating a colours hue, saturation and brightness (labelled as value). Image reproduced from the QT: Online newsletter (Adaptive Coloring for Syntax Highlighting, Helder Correia, 2010).

1.15.2 Additive and subtractive colour mixing

Two colours, composed of the light distributions C_1 and C_2 , can be added together resulting in a new colour being produced (C_3); C_3 can be said to be composed of a mixture of C_1 and C_2 . This mixing can be physically observed by projecting three primary coloured light sources (red, green and blue) on to a whitish surface. Cyan results from the mixing of blue and green, magenta is produced from the mixing of red and blue, and yellow is produced from the mixing of red and green. A whitish is produced by mixing red, green and blue, see Fig. 1.14(a). Note that no combination of two primaries can produce the third. This type of colour mixing is referred to as additive, as to produce the secondary colours of cyan, magenta and yellow, light is 'added' to the white reflecting surface. Colours can also be mixed in a subtractive manner; this involves the combining of colours, for example in the form of paint pigments, that remove certain wavelengths from the reflected light, resulting in new colours being produced. For example, cyan and magenta paint can be mixed to produce blue, cyan and yellow paint can be mixed to produce green and yellow and magenta paint can be mixed to produce red. Mixing all three cyan, magenta and yellow paints will remove almost all the reflected wavelengths resulting in a blackish; Fig. 1.14(b) illustrates this.

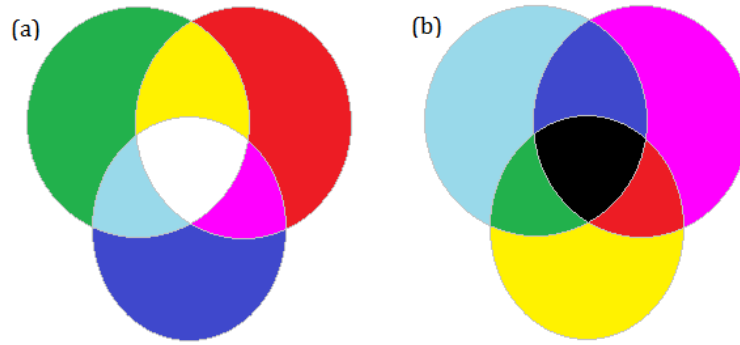


Fig. 1.14(a) and (b)

(a) Illustrates the additive colour mixing of the three red, green and blue primary light sources, (b) illustrates the subtractive mixing using the cyan, magenta and yellow as the primary coloured paint pigments.

The trichromatic (three cone types) nature of normal human vision allows for any colour C_x to be matched/produced by additively combining different intensities (i) of the red, green and blue primaries (R, G and B); this is illustrated by Eq. 1.7, where i_1 , i_2 and i_3 are the intensities of the R, G and B light sources, respectively.

$$C_x = R(i_1) + G(i_2) + B(i_3) \quad \text{Eq. 1.7}$$

1.16 Colour vision

Colour vision is the ability for an observer to perceive colour and is dependent on signals being received by the cone cells and subsequently being processed by higher order brain mechanisms to produce a coloured percept. Two complementary theories of colour vision coexist the trichromatic theory that states that three differently sensitive cell types (now known to be the L-, M- and S-cone cells) are required to explain the range of normal human colour vision. The second is the opponent process of colour vision which states that two sets of

chromaticities (reddish and greenish, and bluish and yellowish) are represented opposed to each other and are processed within two distinct chromatic pathways.

1.16.1 Trichromatic theory

A normal human observer possesses trichromatic vision due to the possession of three different cone cell types being present in their retinas (the L-, M- and S-cones); these cell types have varying sensitivity to photons of different wavelengths (λ) in different regions of the visible spectrum, as described earlier in the chapter. Two factors are responsible for determining the probability of a cone cell absorbing a photon; the luminous flux and the incoming photons wavelength (λ). Consider a retina with only one cone type and hence only one cone sensitivity distribution; when photons were absorbed by these cells the brain would only be able to make an intensity judgement and not a colour judgement as chromatic information is derived from comparisons of signals between different cone types. A brain connected to eyes with only one cone type would, for example, not be able to distinguish whether the incoming light source was of a high intensity at one wavelength or over a range of wavelengths it was not particularly sensitive to, or of a low intensity light at a wavelength or over a range of wavelengths, that it was very sensitive to. An eye with two types of cone is a vast improvement on a mono-cone celled eye, as it will (although in a limited capacity) have the ability to discriminate some combinations of incoming chromatic information and intensity via the ability to compare signals between cone types and hence allow for intensity and a limited colour range to be perceived. This type of observer with two cone types is known as a dichromat; dichromatic observers have the ability to make

colour matches for any colour they can perceive by mixing just two monochromatic (single wavelength) light sources. Trichromatic vision in normal humans is achieved by comparing differences in signals from three cone cell types, each with a different sensitivity curve.

1.16.2 Opponent process theory

The opponent process theory complements the trichromatic theory. Trichromatic theory simply shows that three cone types are required for trichromatic vision whereas as the opponent process theory explains the mechanisms that combine the signals from the cones. The sensitivities of the three cone types as a function of wavelength (λ) have some degree of overlap, especially the L- and M-cone sensitivity functions. It is more efficient, both physiologically and in terms of information theory, to process and transmit signals from the cones as relative differences between them rather than their absolute values. The opponent process theory describes three pathways that are formed from the individual L-, M- and S-cone signals (chapter 2 describes the method for calculating the L-, M- and S-cone signals/excitations and their corresponding contrast signals); they consist of two opponent chromatic pathways that process colour information and one luminance pathway that processes achromatic light and dark information. The two opponent pathways correspond approximately to a reddish-greenish and yellowish-bluish pathway, the signals in these pathways are described by Eq. 1.8 and 1.9, respectively, where RG is the signal in the reddish-greenish pathway and YB is the signal in the yellowish-bluish pathway, L_s , M_s and S_s are the input signals from the

L-, M- and S-cones, respectively. The signal in the luminance (Lum) pathway is given by Eq. 1.10 and is a function of L_s , and M_s .

$$RG = L_s - M_s \quad \text{Eq. 1.8}$$

$$YB = S_s - (L_s + M_s) \quad \text{Eq. 1.9}$$

$$\text{Lum} = L_s + M_s \quad \text{Eq. 1.10}$$

The way in which the signals from the L-, M- and S-cones combine is illustrated in Fig. 1.15; on the left hand side the input signals (L_s , M_s and S_s) from the retina are shown, these signals then combine according to the lines and +/- symbols; for example the L_s and M_s signals sum and are then subtracted from the S-cone signal (S_s) to form the S-(L+M) yellowish-bluish pathway. If the magnitude of the signal produced by summing L_s and M_s is less than S_s then the expression S-(L+M) will evaluate to a positive number, this will result in a bluish chromaticity being perceived (an S-(L+M) increment); if the expression evaluates to a negative number, when $S_s < (L_s + M_s)$, then a yellowish chromaticity will be perceived (an S-(L+M) decrement). The signals in the reddish-greenish and luminance pathways can also be increments or decrements, e.g., $+[L-M]$ and $-[L-M]$ correspond to a reddish-greenish increment and decrement, respectively.

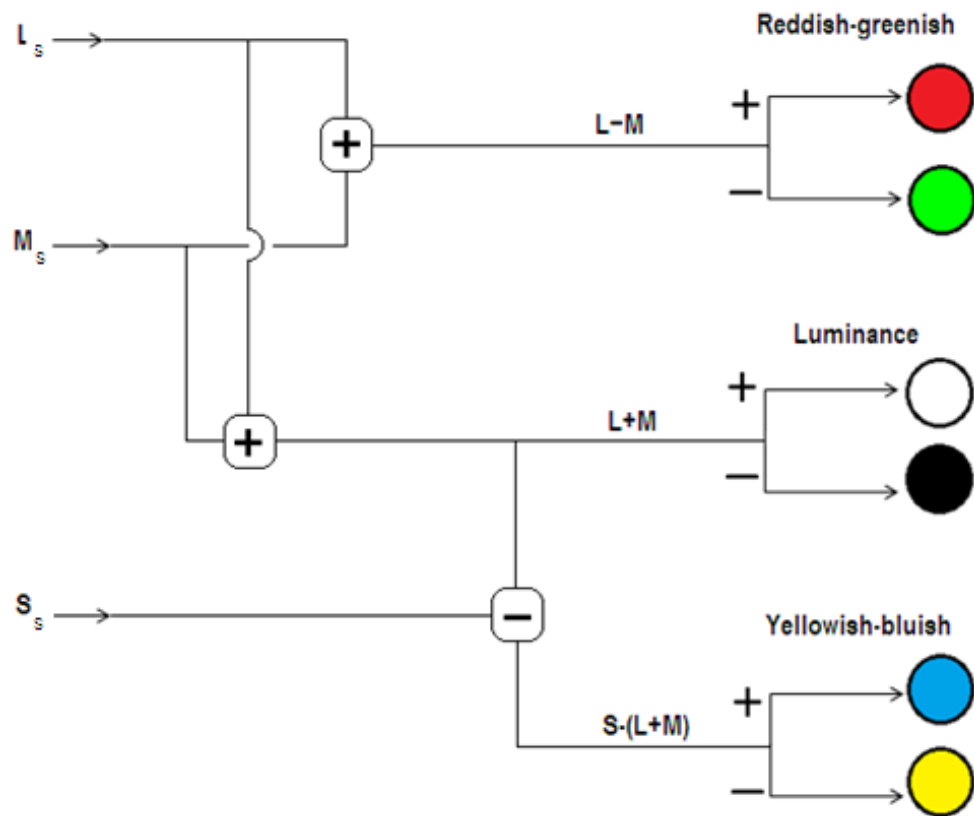


Fig. 1.15

The opponent process combines the L_s , M_s and S_s cone signals into the two opponent chromatic pathways and one luminance pathway. The +/- symbols in boxes denote that the signals are either being summed or subtracted. The +/- symbol not surrounded by boxes refer to the signal either being an increment or a decrement.

These three pathways can be represented by the Derrington-Krauskopf-Lennie (DKL) colour space, where each of the x-, y- and z-axes corresponds to the L-M, S-(L+M) and L+M pathway, see Fig. 1.16. The point at which $dkl(r, \theta, \phi) = dkl(0, 0, 0)$ is a defined achromatic point, for example, a white point given by illuminate D65 (Noboru and Robertson, 2005). Within the DKL colour space the angle θ describes the hue direction analogous to the hue direction of the HSL colour space. The actual colour angles chosen are arbitrary, but the reddish-greenish (L-M), and yellowish-bluish (S-(L+M)) axes are orthogonal. Relative to the achromatic point at (0,0,0), increments are made in the reddish (+[L-M]) and bluish (+[S-(L+M)])

directions; decrements can be made in the greenish ($-[L-M]$) and yellowish ($-[S-(L+M)]$) directions. Chromaticities, under normal conditions, are not perceived together if they lie on opposite ends of the same axes, i.e., a reddish-green or greenish-red; or a yellowish-blue or bluish-yellow will never be perceived simultaneously. The parameter \emptyset describes the luminance contribution; if \emptyset is constant and zero then changes in r and θ will result in isoluminant changes in chromaticity (saturation and hue) only. A luminance angle (\emptyset) of 90° corresponds to an increase in luminance, $\emptyset = -90^\circ$ corresponds to a decrease in luminance; whilst the excitations in the chromatic pathways is kept constant. Directions in DKL space can be defined that vary the signal in both chromatic pathways simultaneously (when; $\theta \neq 0$ and $\theta \neq 90$ and $\theta \neq 180$ and $\theta \neq 270$), or in all three pathways simultaneously (when; $\theta \neq 0, 90, 180$ or 270 , and $\emptyset \neq \pm 90$).

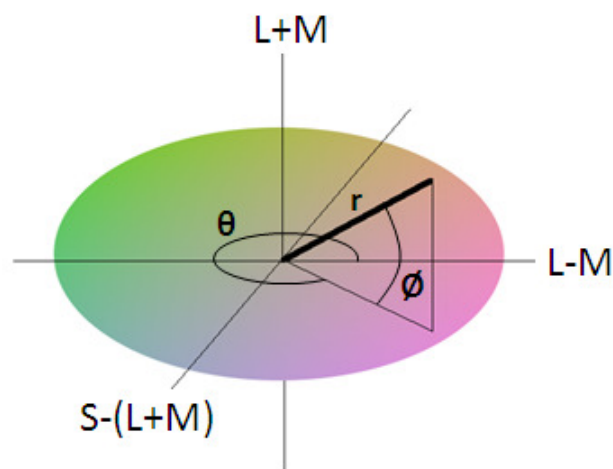


Fig. 1.16

The two chromatic and luminance pathways of the DKL colour space are represented. r is a vector, the length of which represents the difference of a chromaticity relative to point $(0,0,0)$, θ describes the chromaticity in terms of the angle between chromatic pathways and \emptyset represents the contribution of the luminance pathway.

1.16.3 Unique hues

Unique hues are defined as red, green, blue and yellow that contain no contamination in their appearance from the neighbouring opponent chromaticities; for example, unique blue is the blue that does not appear to contain any reddish or greenish in it so it has the appearance of a “pure” (unique) blue. It can be noted that the unique hues do not align with the two orthogonal axes representing the colour opponent pathways (Wuerger *et al.*, 2005), see Fig. 1.17. This is the reason the L-M pathway is referred to as reddish and greenish and the S-(L+M) pathway is referred to as yellowish and bluish, as the appearance along these axes do not appear uniquely as red, green, yellow and blue.

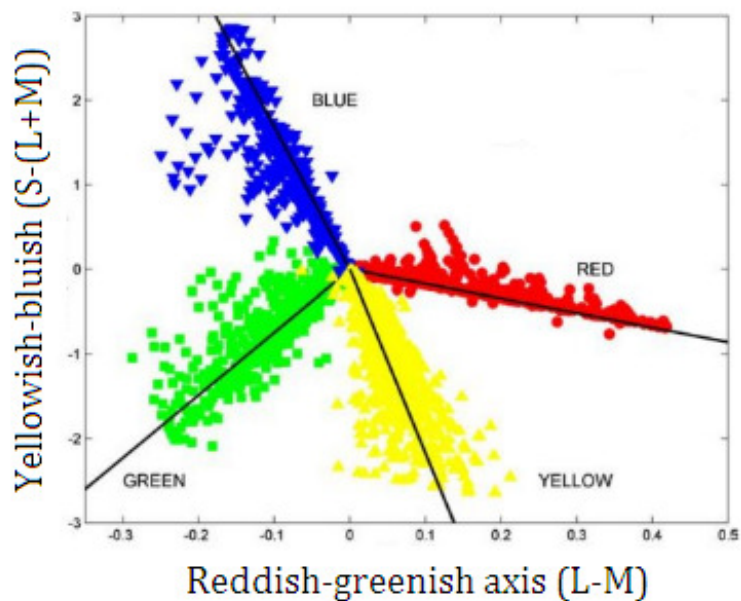


Fig. 1.17

Unique hue data shown relative to the L-M and S-(L+M) axes. Modified from Wuerger (2005).

1.16.4 The CIE 1931 colour space

In 1931 the Commission Internationale de l'éclairage (CIE), the international authority on lighting, illumination, colour and colour spaces, produced the CIE 1931 colour space, the 1931 CIE 2° standard observer and a set of colour matching functions (CIE, 1932). A series of colour metric experiments were performed by Wright and Guild (Wright, 1928; Guild, 1931) whose results were combined to form the CIE RGB colour space; this space was used as the basis for the CIE 1931 xy colour space. As the retina contains three cone types the L-, M- and S-cones that are sensitive in the long, medium and short wavelength regions of the visible spectrum, respectively. Therefore the range of colours distinguishable to a normal trichromatic observer can be described through the use of only three signals, one corresponding to each cone type. A set of tristimulus values, denoted by (capital) XYZ, are defined such that when two colours appear to match, they will have equal tristimulus X, Y and Z values. A colour match will always have matching tristimulus values even if the colours are metamers; that is two colours that are composed of unequal spectral power distributions but which produce matching colours. Fig. 1.18 illustrates the CIE 1931 colour space; the main horseshoe shaped locus corresponds to the spectral (single wavelength) colours is shown bounding space. The straight line connecting the two ends of this locus is known as the line of purples and connects spectral red and violet at opposites ends of the visible spectrum with a series of non-spectral purples.

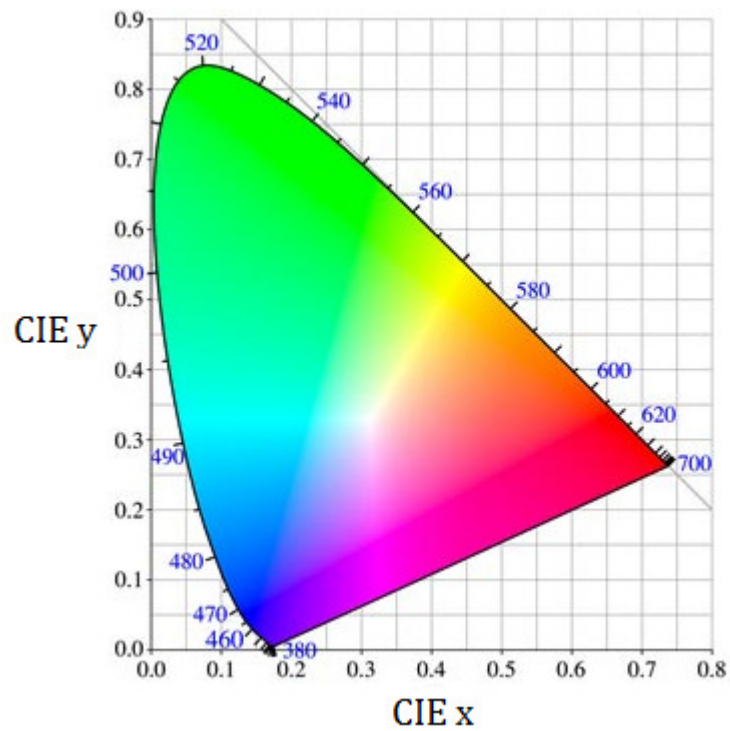


Fig. 1.18

The CIE 1931 xy chromaticity diagram. Image adapted from savory.de (Accessed July 2011).

1.16.5 CIE standard 2 deg standard observer and the colour matching functions

The spatial distribution of L-, M- and S-cones within the retina is not homogeneous (see the cone mosaic section); therefore the values of the tristimulus values will not be independent of the size of the field of view, i.e., how much of the scene is viewable. It was decided by the CIE commission to restrict the field of view to 2°. The functions corresponding to this CIE standard observer are defined by a set of colour matching functions (CMF); these CIE 2° CMFs are a set of three functions denoted by $\bar{x}(\lambda)$, $\bar{y}(\lambda)$ and $\bar{z}(\lambda)$, which are essentially the three spectral sensitivity curves of the CIE 2° standard observer when stimulated by light of wavelength λ to produce the tristimulus values X, Y, and Z. These functions are the definition of the

CIE standard observer. The three X, Y and Z tristimulus values for the CIE 2° standard observer for a given spectral power distribution $P(\lambda)$, i.e., chromaticity, are defined by Eq. 1.11, 1.12 and 1.13, respectively. In order to computationally calculate the X, Y and Z tristimulus values, for example in 1 nm increments, Eq. 1.11, 1.12 and 1.13 are converted into their corresponding discrete versions (Eq. 1.14, 1.15 and 1.16, respectively), over the range $400 \leq \lambda \leq 700$ nm.

$$X = \int_0^{\infty} P(\lambda) \bar{x}(\lambda) d\lambda \quad \text{Eq. 1.11}$$

$$Y = \int_0^{\infty} P(\lambda) \bar{y}(\lambda) d\lambda \quad \text{Eq. 1.12}$$

$$Z = \int_0^{\infty} P(\lambda) \bar{z}(\lambda) d\lambda \quad \text{Eq. 1.13}$$

$$X = \sum_{400}^{700} P(\lambda) \bar{x}(\lambda) d\lambda \quad \text{Eq. 1.14}$$

$$Y = \sum_{400}^{700} P(\lambda) \bar{y}(\lambda) d\lambda \quad \text{Eq. 1.15}$$

$$Z = \sum_{400}^{700} P(\lambda) \bar{z}(\lambda) d\lambda \quad \text{Eq. 1.16}$$

1.16.6 Wavelength discrimination

The classic wavelength discrimination experiment measures the just noticeable difference (JND) between two monochromatic light sources that arise due to small differences in their wavelength; the experimental procedure is as follows. A maxwellian view set up (Thibos, 1990) is used to display a bipartite field to an observer, see Fig. 1.19(a). One half of this field has a test monochromatic light of a

known wavelength displayed within it, the other half field has a light with a comparison wavelength. The wavelength of the comparison field is varied under the control of the observer, as the observer varies the wavelength they also make adjustments to the luminance of the comparison field attempting to maintain the whole field at a perceptually equal luminance level (brightness). The wavelength discrimination threshold is defined as the point when the two fields appear different independent of the luminance of the field (Pokorny and Smith, 1970). If the wavelength of the test field is λ , the wavelength of the comparison field is $\lambda + \Delta\lambda$. A typical plot of $\Delta\lambda$ as a function of λ is shown in Fig. 1.19(b), it approximately follows a “W” shape for human observers, with a central peak at ~ 540 nm, surrounded by two minima at ~ 490 and 580 nm. The curve rapidly increases at the two ends of the spectrum, for high wavelengths above ~ 630 nm and low wavelengths below ~ 470 nm, with an additional local maxima at ~ 450 nm. It can be noted from Fig. 1.19(b) that a JND can occur with a very small difference in wavelength ($\Delta\lambda$), this can be as low as ~ 1 nm over the bluish and yellowish regions of the spectrum. The “W” shape of this curve has been shown to have its minimum and maximum peaks correspond to the chromatic opponent (reddish-greenish: L-M and Yellowish-bluish: S-(L+M)) pathways (Zhaoping *et al.*, 2011).

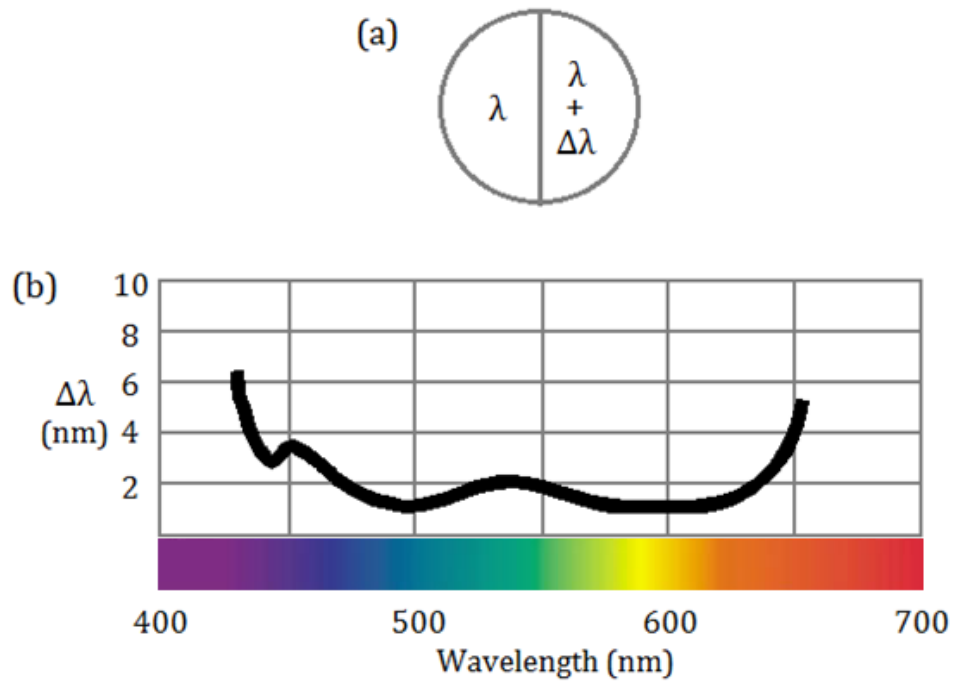


Fig. 1.19(a) and (b)

The classic wavelength discrimination experiment stimulus; the test field of wavelength λ (left) and the comparison field of wavelength $\lambda + \Delta\lambda$ (right). The typical "W" shaped plot obtained over the visible spectrum for λ vs. $\Delta\lambda$. Adapted from Wright and Pitt (1934).

1.16.7 Colour discrimination – MacAdam's ellipses

An early experiment that investigated the variation of colour discrimination thresholds was performed by MacAdam (1944); although the experiment was actually based on observers making a series of colour matches, the observers' errors provide a reflection of their colour discrimination thresholds. A fixed reference colour was presented and the observers' task was to adjust a second colour next to it until it matched the reference colour, both colours were presented next to each other in a 2° comparison field. Using the same reference colour the observers made repeated colour matches along different directions in colour space and standard deviations of the matches for a number of colour directions were

calculated. It was discovered that plotting the standard deviations of these matches with respect to the reference colour in the CIE 1931 xy chromaticity diagram produced an ellipse with the reference colour located approximately at its centre. In total, 25 reference colours were used and 25 corresponding ellipses produced. Fig. 1.20 shows a single MacAdam's ellipse from this 1942 study; the hollow points are the standard deviations of successive colour matches with respect to the chromaticity located at CIE xy: (0.160, 0.057), for a single observer (PGN), the best fitting ellipse that represents the discrimination contour is also indicated by the solid black line.

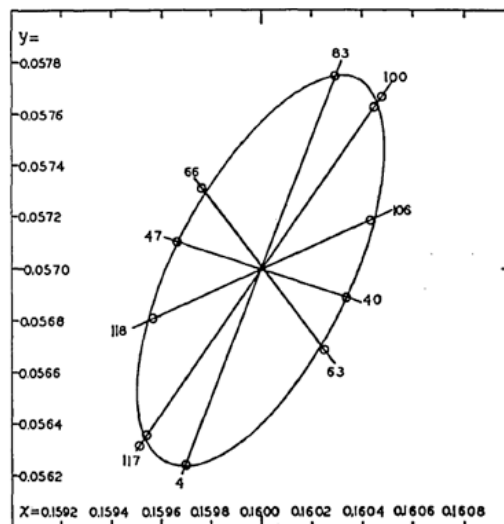


Fig. 1.20

A single MacAdam's ellipse; the white circles are the standard deviations for colour matches made with respect to the reference colour, located CIE xy:(0.160, 0.057), along different directions of the colour space. The black contour is the best fit ellipse that represents the average standard deviation for each colour direction. Reproduced from MacAdam (1942).

The reference and test fields were presented with a luminance of approximately 48 cd m⁻², over the course of the experiment it has to be assumed that some chromatic adaptation to the stimulus occurred. Fig. 1.21 shows all 25 fitted discrimination

ellipses (scaled by a factor of x10 for clarity). It is shown later that these data are consistent with the presented study in chapter 3 as well as a linear model of cone excitations.

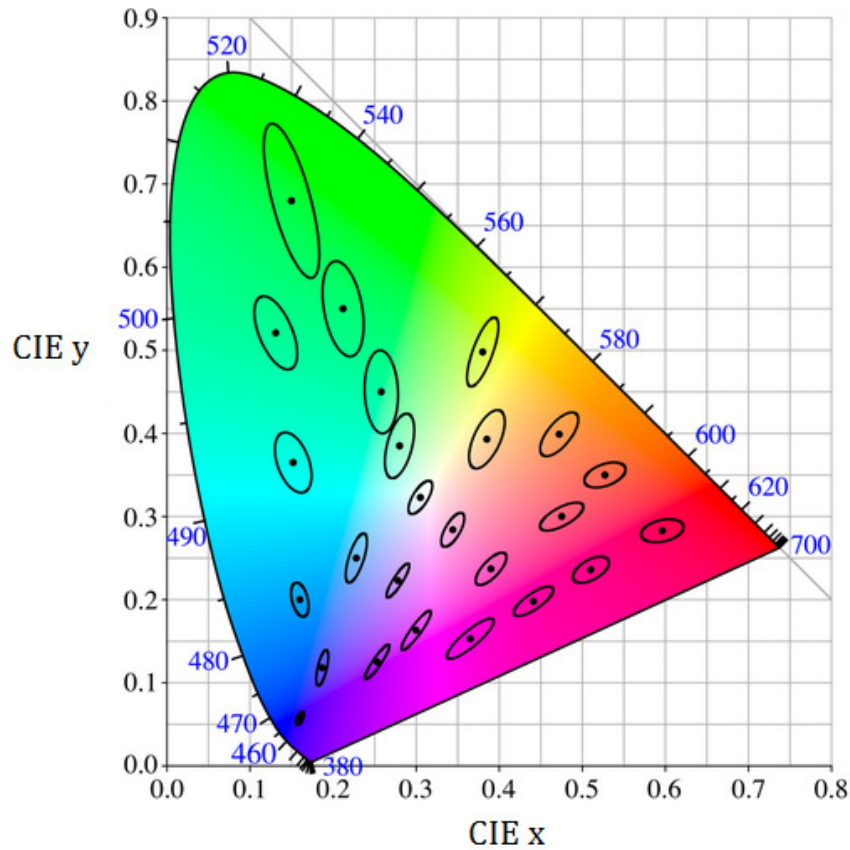


Fig. 1.21

All 25 MacAdam's ellipses (scaled x10) illustrated in CIE 1931 colour space. Image adapted from photometrictesting.co.uk (accessed Nov 2011).

1.16.8 Chromatic adaptation

When an observer is exposed to a particular chromaticity over time they will chromatically adapt to it, that is, their cone sensitivities adjust themselves in such a way as to become more sensitive to chromaticity changes at that given adaptation point. This adaptation can be described by the Von Kries model. This model

applies a gain (i.e., it changing the output signal relative to the input signal) to the sensitivity curve of each of the cone types independently; this is done in such a manner as to keep the adapted appearance of a reference achromatic (whitish) chromaticity constant. The gain is applied in such a way that it is dependent on the excitation within a particular cone class independently, for example, if the observer is exposed to an illuminant with only a bluish/violet component then the S-cone gain will reduce in response to the exposure to a greater degree than the L- and M-cones response. Colour constancy, the mechanism whereby an object's colour appearance remains constant under different illumination conditions, relies on independent variation of the gains on the L-, M- and S-cone sensitivity curves. The transformation from one illuminant to another can be approximately modelled based on the produced cone excitations (the method for calculating cone excitations is outlined in chapter 2), it can be described by Eq. 1.17. L, M and S are the cone excitations produced under the adapting illuminate; L_1 , M_1 and S_1 are the cone excitations produced under a second illuminant and $L_{1,achromatic}$, $M_{1,achromatic}$ and $S_{1,achromatic}$ are the cone excitations produced under the second illuminant which produces an achromatic percept.

$$\begin{bmatrix} L \\ M \\ S \end{bmatrix} = \begin{bmatrix} 1/L_{1,achromatic} & 0 & 0 \\ 0 & 1/M_{1,achromatic} & 0 \\ 0 & 0 & 1/S_{1,achromatic} \end{bmatrix} \begin{bmatrix} L_1 \\ M_1 \\ S_1 \end{bmatrix} \quad \text{Eq. 1.17}$$

1.16.9 Pre-photoreceptor filters

In order for light from an external light source incident on the eye to reach the retina it has to be transmitted by two important pre-receptoral filters. Firstly, incident light passes through the lens of the eye which, especially as an observer ages, can undergo a process of “yellowing”; this has the effect that it will filter some portion of the short wavelength light. The second is the filtering effect of the macular pigment (MP), this is a yellowish pigment that covers the central fovea, it also filters some portion of the short wavelengths of the incident light. These two filters are discussed in the next two sections.

1.17 Macular pigment density

Macular pigment (MP) is found on the inside surface of the retina, it is a yellow coloured pigment that typically covers the central 5 mm of the fovea. Fig. 1.22 shows the variation of MP density - it can be seen that it affects the short wavelength bluish region of the visible spectrum. Many templates have been proposed to describe the MP filtering effect (Vos, 1972; Wyszecki and Stiles, 1967; 1982), in general they suffered from an overestimate of the MP optical density. Bone *et al.* (1992) derived a template that was based on an experimental technique where lutein and zeaxanthin, the components of MP, were held in solution whilst their transmission properties were recorded over the visible spectrum with a spectrophotometer. The Bone template, shown in Fig. 1.22 was derived from these results and the Stockman-Sharpe cone fundamentals have the Bone template (scaled to a peak value of 0.35) factored into them (Sharpe and Gegenfurter, 2001). It has been proposed that its purpose is to filter out harmful high energy

blue light which could potentially damage the retina over long exposure times, this is commonly referred to as the “blue light hazard” (Sparrow *et al.*, 2002).

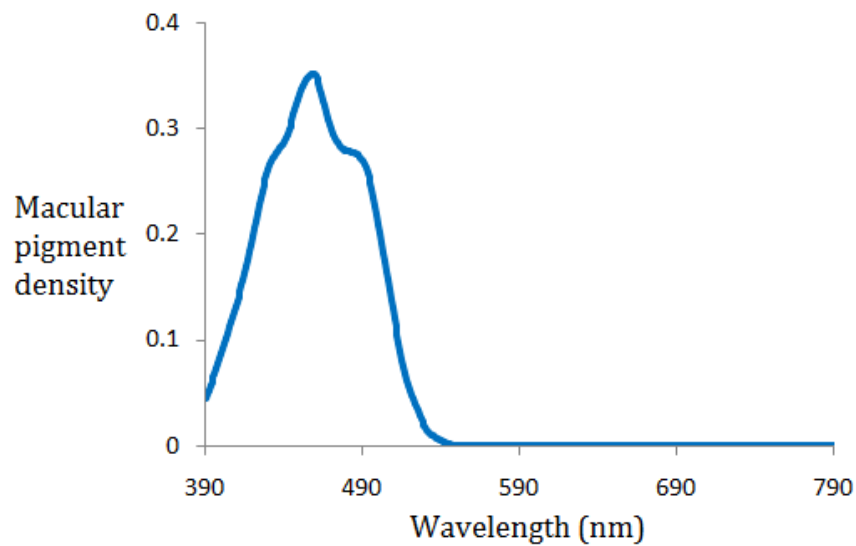


Fig. 1.22

The Bone Macular pigment template showing the variation of Macular pigment density as a function of wavelength (nm).

1.18 Lens pigment density

Similarly to the effect provided by the macular pigment, the yellowing of the crystalline lens within the eye also filters incident short wavelength blue light. The template provided by van Norren and Vos (1974) representing the mean absorption due to the lens has also been factored into the Stockman-Sharpe cone fundamental functions (Sharpe and Gegenfurtner, 2001); this curve is plotted in Fig. 1.23. This curve has been shown to vary over the course of an observer’s lifetime; as they grow older and hence have longer exposure times to natural light the greater the yellowing.

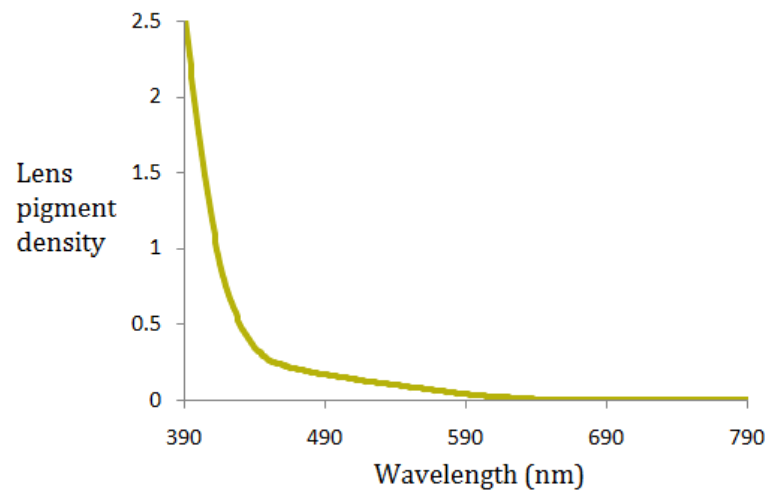


Fig. 1.23

The pigment density of the crystalline lens is plotted as a function of wavelength (nm).

Chapter 2

Materials, methods and data processing

2.1 Introduction

This chapter describes the hardware, experimental procedures and data analysis methods used in this study. The Colour Assessment and Diagnosis (CAD) test is the most used system and is hence given most attention; the P_Scan-100 pupil measurement system and the Macular Assessment Profile (MAP) test are also described.

2.2 The Colour Assessment and Diagnosis (CAD) test

The CAD test was developed at City University and employs dynamic luminance contrast noise (Barbur *et al.*, 1992; Birch *et al.*, 1992). All CAD test graphics and controlling software was programmed in C++ and runs under DOS and Windows (Microsoft Corporation) operating systems. The test allows psychophysical measurement of human chromatic detection thresholds. This is achieved by displaying a series of moving chromatic stimuli, embedded within a grid of dynamic luminance contrast noise; observers make judgments on the direction of travel of these stimuli and via a series of interleaved staircases and observer responses a final set of chromatic detection thresholds, in terms of CIE 1931 chromatic displacements (CD), are produced. A series of CDs are normally

produced for a set of CIE xy colour directions relative to some given background coordinates allowing an elliptical contour to be computationally fitted. Many parameters within the CAD test can be manipulated providing a convenient testing system for data collection in the following colour vision studies. For example, the chromaticity and luminance of both the foreground (within which the stimuli is presented) and background, along with temporal properties of the stimuli, such as the velocity of the stimuli can be varied.

2.2.1 CAD test equipment

The stimulus was displayed on a Sony Multiscan 500PS Trinitron monitor, which has a screen size of $27^\circ \times 22^\circ$ (viewing distance: 70 cm) and a frame rate of 75 Hz. The monitor was driven by an ELSA Gloria XL 30-bit graphics card. The controlling software ran on a desktop PC running MS-DOS; the choice of operating system for this study was to eliminate the risk of context switching and hence ensure accurate timing for stimulus generation and display. Observers responded to the stimuli by pressing one of four buttons on a handheld control pad which was connected to the PC via an Amplicon PC30AT multifunction data acquisition card. A Zeiss chin and forehead rest were used for convenience and to maintain a fixed eye-to-monitor viewing distance (70 cm); this chin and forehead rest is enclosed within a 'head box' which contains additional equipment used for measuring and tracking the pupil (discussed later in the chapter). Fig. 2.1 is a schematic of the physical CAD system set up; the observer is indicated (grey) with their head in the 'head box' (purple), resting against the chin and forehead rests, the CRT display is

positioned with its screen at approximately the same vertical level as the observers eyes, with a horizontal separation of 70 cm.

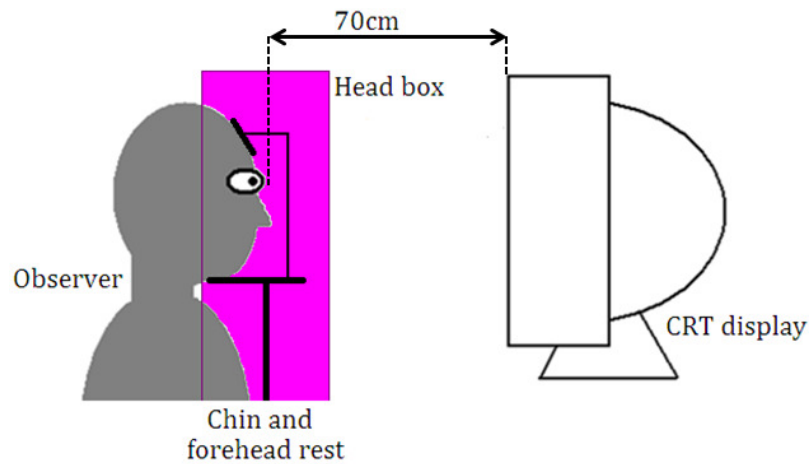


Fig. 2.1

The physical set up of the CAD system.

2.2.2 Monitor calibration

In order to reliably reproduce chromaticities and luminance levels the CRT display requires calibration. The calibration involves two stages outlined in the next two sections; first the luminance gamma correction followed by the measurement of the spectral power measurement of the red, green and blue phosphors (RGB phosphors).

2.2.3 Gamma correction

The RGB phosphors of the display increase their luminance output as the voltage applied to the RGB phosphor guns is increased. The relationship between the

luminance outputs of the phosphors and the applied voltage is non-linear; it typically follows a power relationship - the power of which is referred to as the 'gamma'. It is important to correct for this non-linearity as the displayed colour saturation and hue vary with changes in gamma, in addition without correction most images will be displayed too dimly. Fig. 2.2(a) shows that when displaying the input image (top row) with no gamma correction applied, the output image (bottom row) will not be reproduced correctly. Fig. 2.2(b) shows the same input image (top row), along with the gamma correction to be applied (middle row) where the output image (bottom row) equals the desired output given the input image, i.e., the input and output images are equal.

The three RGB phosphors have different luminance output ranges; these are plotted in Fig. 2.3, the output luminance of the three RGB phosphors is plotted as a function of applied voltage. It can also be observed that at the maximum gun voltage ($V_{\max}=700$ mV) the green, blue and red phosphors are at their maximum output luminance values of ~ 79 , ~ 21 and ~ 10 cd m⁻², respectively. For each phosphor in isolation, each luminance increment is displayed on screen and measured using a luminance meter and these luminance values are stored in a look up table (LUT). The graphics card makes use of the LUT in order to calculate the required voltage that needs to be applied to each phosphor gun in order produce a particular desired luminance level for each pixel on the display screen.

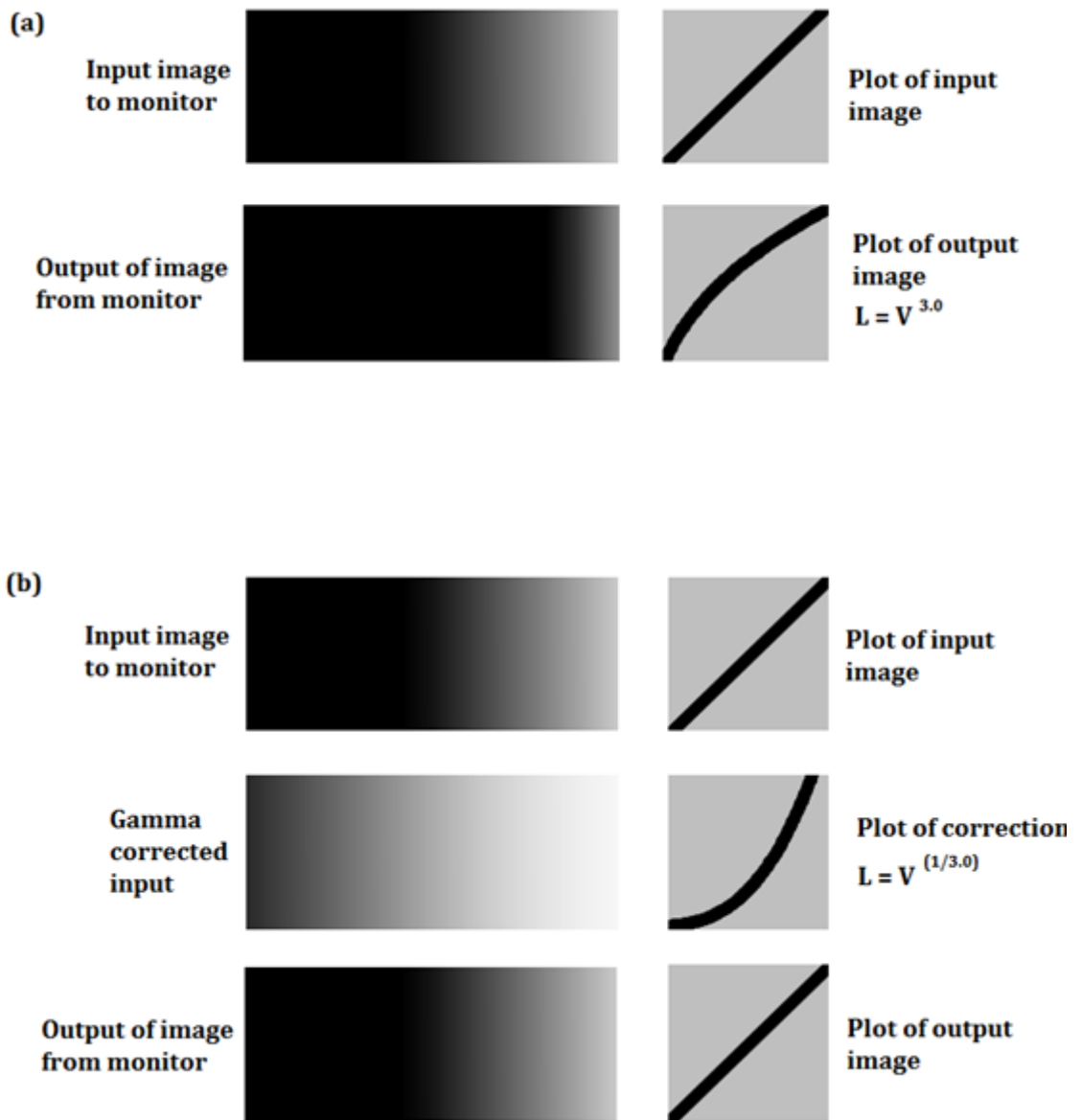


Fig. 2.2 (a) and (b)

The top row of (a) shows an example input luminance gradient, the bottom row shows the results that would be displayed on a non-gamma corrected monitor. The top row of (b) again shows an input luminance gradient, the second row shows the input after the gamma correction has been applied, the bottom row shows the corrected output image, i.e., the desired output image equals the input image (V =voltage, L =luminance). Figure adapted from siggraph.org (accessed Feb 2012).

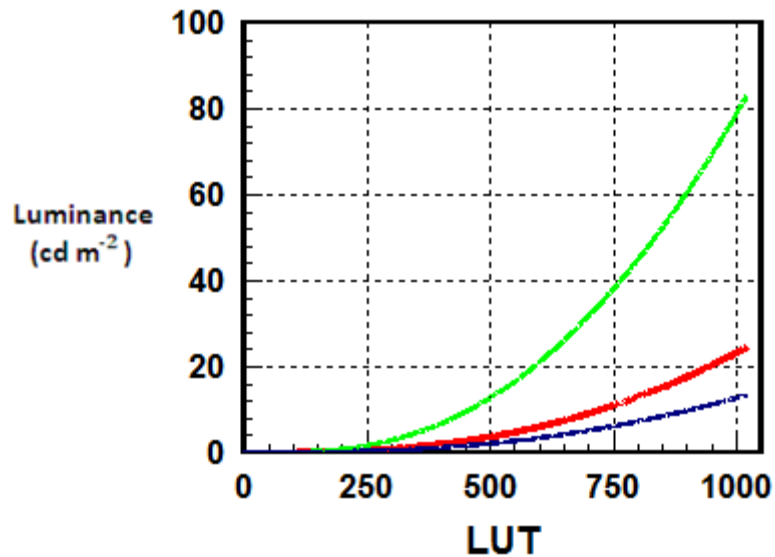


Fig. 2.3

The luminance outputs of the RGB phosphors as a function of LUT address. Each phosphor follows a power law as the voltage increases.

2.2.4 Red, green and blue monitor phosphor calibration

In addition to the gamma correction that takes care of the luminance component of any output display signal; the spectral power distributions are also required for calibrated chromatic output on the display. A spectroradiometer along with custom controlling software to display each of the RGB phosphors in isolation was used to achieve this; the spectroradiometer recorded the spectral power distribution of the RGB phosphors in isolation over the visible spectrum, in 1 nm increments. The measured spectral power distributions are plotted in Fig. 2.4, the plot is colour coded so that red corresponds to the red phosphor, green corresponds to the green phosphor and blue corresponds to the blue phosphor.

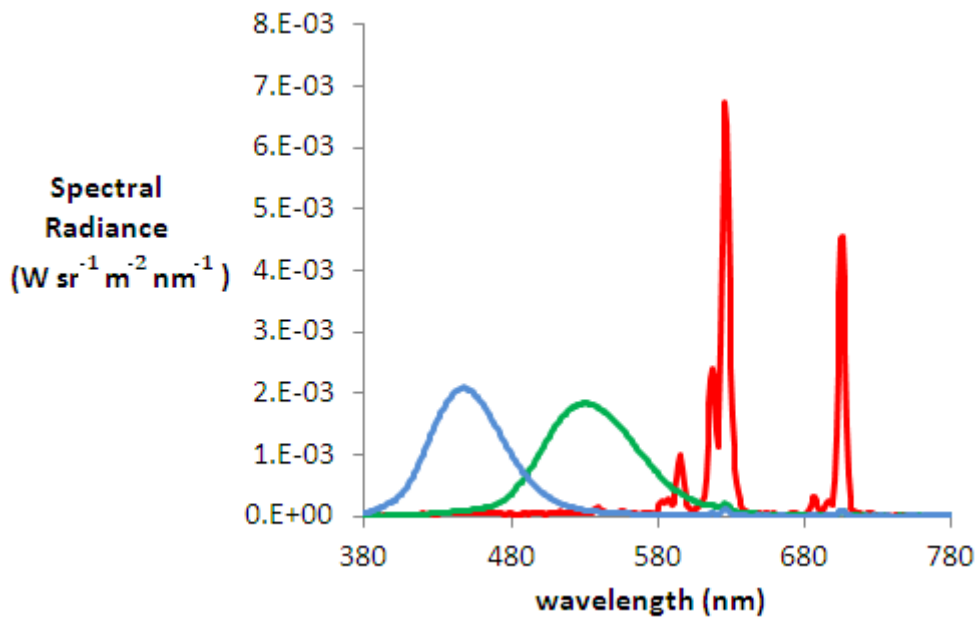


Fig. 2.4

The spectral power distributions of the red, green and blue phosphors, indicated by the red, green and blue curves, respectively.

These spectral power distributions are used to calculate the entries in a colour look up table (cLUT). When the CAD system is required to display a particular chromaticity the cLUT can be consulted to determine the correct RGB values to be used. These are then transformed by the graphics card into the appropriate gun voltages for each pixel on the CRT display.

2.2.5 CAD stimulus and experimental procedure

The CAD test uses spatiotemporal luminance noise to isolate the use of colour signals (Barbur, 1992 and 2003). The latest version of the test employs a 5 x 5 square array of checks which move diagonally, in a randomly selected direction (four possibilities). The stimulus moves at a constant speed of $\sim 4^\circ \text{ s}^{-1}$ over a

visual angle of $\sim 2.9^\circ$; movement is across a slightly larger square region of $\sim 3.3 \times 3.3^\circ$ defined by the dynamic luminance contrast noise. The stimulus chromaticity, as specified by its CIE 1931 xy coordinates, has the same mean luminance as the checks of the square target area. The Euclidian distance between target and stimulus chromaticities (CD) provides a measure of colour signal strength. Sixteen or twenty different directions in CIE space relative to the positive CIE x-direction (defined as zero degrees) were normally specified for testing. The thresholds were measured along each direction using one interleaved staircase per direction tested. For each trial presentation the stimulus direction of travel was chosen randomly; the stimulus always started in one of the four corners of the larger patch of luminance noise (the 'foreground' or 'target area') and moved diagonally towards the opposite corner. A larger surround, i.e., the rest of the display, subtended $27^\circ \times 22^\circ$ (the 'background'). The observers detect the coloured stimulus when displayed on the foreground which is in turn surrounded by the uniform background. Fig. 2.5 shows an example of a chromatic CAD stimulus embedded in the patch of luminance noise. The observers are instructed to press any button when unable to detect the coloured stimuli. Multiple presentations of the same stimulus, within the interleaved staircases, were tested to ensure that the chance of the subject guessing the direction of motion correctly when they had not detected the stimulus was less than 1 in 16. About 90 seconds of adaptation to the uniform background field preceded each testing block. When testing at low light levels ($< 3 \text{ cd m}^{-2}$), subjects dark adapted for 20 minutes, this was in order to ensure the cones had dark adapted past the start of the dark adaptation curve plateau (~ 7 minutes) and the rods were also adapted. When testing at lower light levels a neutral density filter (see next section) was placed in front of the observer's eye. This allowed the actual luminance level of the display to be kept

relatively high, while presenting the stimulus, foreground and background at a lower luminance level. The full spectral transmittance of the filter was used together appropriately when calculating the luminance/chromaticities of the displayed stimuli.

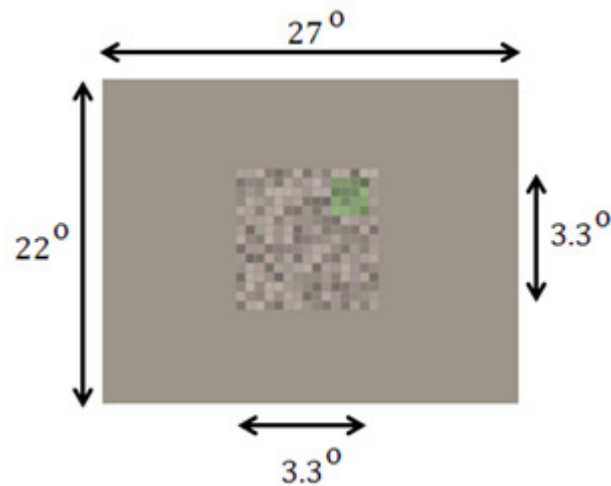


Fig. 2.5

An example of a greenish CAD stimulus embedded in the patch of luminance noise. The dimensions of the luminance noise patch and entire display is indicated.

2.2.6 Neutral density filters

An ideal neutral density filter reduces the intensity of each wavelength present in the incident light and transmits this reduced intensity spectrum without changing its chromatic content, i.e., it can reduce the luminance only. The optical density (OD) of the filter is given by the negative \log_{10} of the ratio of light intensity transmitted to that incident on the filter. Fig. 2.5 plots the transmission spectra of three typical neutral density filters, with OD nominal values of 0.1, 0.4 and 0.5. They were employed when testing observers on the CAD system when the required luminance was below 3 cd m^{-2} ; this allows high luminance to be

physically displayed on the CRT, whilst a low luminance stimuli is presented to the observers.

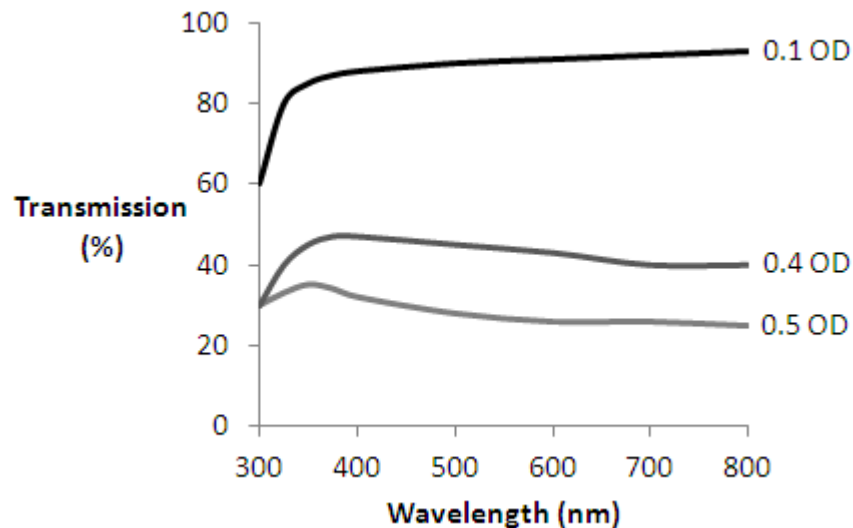


Fig. 2.6

The transmission spectra of three neutral density filters with OD values of 0.1, 0.4 and 0.5.

2.3 Data processing

Once a set of CAD detection thresholds are measured, the thresholds can be converted into a relative cone excitation space, a cone contrast space or left unprocessed as CIE 1931 colour space coordinates and examined in terms of the measured chromatic displacements (CD). The cone excitation and cone contrasts method can reveal detection threshold variations in terms of the opponent L-M vs. S mechanisms; ellipses can be fitted in any of these spaces in order to visualise a mean contour describing the detection thresholds. An additional method is to display the individual L-, M- and S-cone contrasts as a function of the angle they subtend in a given colour space, this could be CIE, cone excitation or cone contrast;

these plots are referred to as cone contrast curves. The following sections describe these methods further and provide examples of each; they are all used in later chapters for analysis/modelling.

2.3.1 The use of ellipses

Chromatic threshold ellipses are commonly used to describe colour matching, discrimination and detection data (Brown and MacAdam, 1949; Wyszecki and Fielder, 1971; Dischler and Valberg, 2006). This is largely due to the goodness-of-fit of the ellipse equations to the raw measured data. Some researchers, however, have expressed the opinion that ellipses are not the best descriptors of the data (Nagy, 1998). Poirson *et al.* (1990), investigated the fitting of other basic parametric shapes to colour threshold detection data. In addition to ellipses, rectangles and parallelograms were fitted to their data. They found that ellipses and rectangles could indeed be fitted to the data with the same degree of error, this is due to the geometric similarities of ellipses and rectangles. Parallelograms however could be fitted with a lower degree of error than both the ellipses and rectangles, it was hypothesised that this was due to parallelograms being a generalised rectangle and hence providing extra degrees of freedom for the fitting algorithm. Fig. 2.7 is reproduced from Poirson *et al.* (1990) and shows an example of a set of measured detection thresholds (black squares), along with three different geometrical fitted shapes (a parallelogram, rectangle and ellipse).

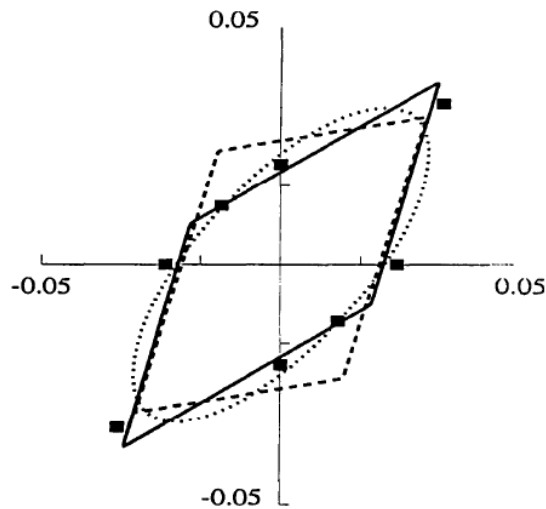


Fig. 2.7

A set of detection thresholds (Black squares) along with a fitted parallelogram (solid line), rectangle (dashed line), and ellipse (dotted curve). Reproduced from Porison et al. (1990).

The use of rectangles was rejected as a good descriptor by Porison, even though they mathematically approximate the data to a high degree of precision, as they do not provide a means of identifying physiological visual mechanisms. Although visual mechanisms could be identified from the parallelogram they did not improve upon the fitted ellipse. It was decided to use the ellipse paradigm in the following investigations to describe the measured colour detection data; this would aid with the comparison to historical data and it also appears to be the most physiologically likely.

2.3.2 Fitting algorithm

In order to fit an ellipse to a set of data there are a variety of fitting methods that could be employed, for example Porrill (1990), Gander (1981; 1994) and Rosin (1999). The entire set of fitting algorithms considered for use in this study employed a least squares technique (Björck, 1996). The main consideration in

choosing a fitting algorithm was whether to use a method that employed a fixed or non-fixed centre, i.e., would the coordinates of the centre of the ellipse be input parameters to the algorithm? It was decided to use a non-fixed centre for a number of reasons. Ellipses in the following experiments were measured over a wide (>2.5 log units) range of luminance levels. The measured detection ellipses become significantly asymmetric over the lower light levels tested (<3 cd m⁻²), mainly due to an increased threshold in the yellow direction, as also shown previously by Brown (1951). These observations reflect differences in sensitivity for increments and decrements in S-cone signals at low light levels (Walkey *et al.*, 2001; Yebra *et al.*, 2001). Non-fixed centre fitting methods preserve this yellow-blue ($\pm S$) asymmetry elongation when it occurs. The method outlined by Fitzgibbon *et al.* (1999), was chosen for all ellipse fitting. This method takes the raw measured data points as its inputs, and outputs a result set containing the semi-major axis, semi-minor axis, orientation (semi-major axis relative to the abscissa) and the coordinates of the fitted ellipse centre. Due to the possibility of a yellow-blue asymmetry, the centre of the fitted ellipses are not necessarily in the same position as the foreground chromaticity coordinates being considered. The maximum number of raw threshold data points to be fitted at any one time was 20, i.e., one blocks worth of data; for datasets of this size the fitting computation time was negligible (<1 second on a standard desktop PC). Fig. 2.8. shows an example of a set of CAD measured detection thresholds and their corresponding fitted ellipse in CIE xy space (the coordinates of the CDs were used as inputs). The thresholds were measured relative to the target at CIE xy: (0.265, 0.420), over 16 equally space directions.

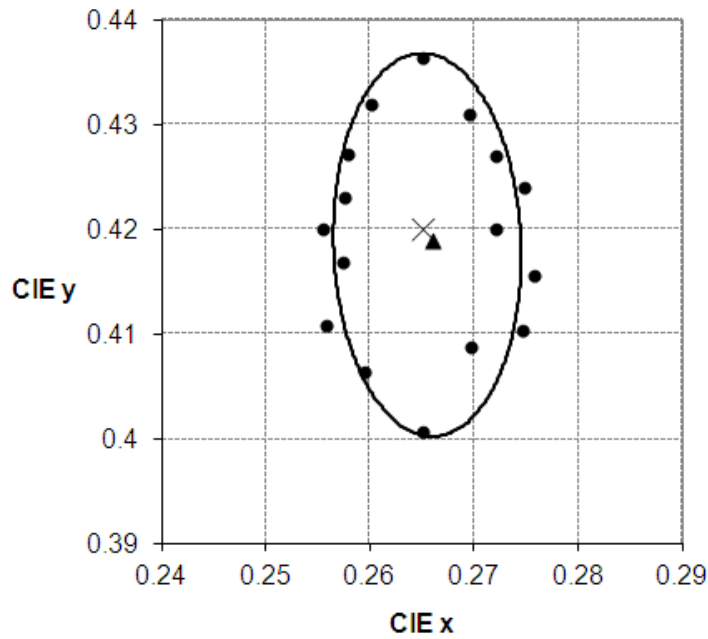


Fig. 2.8

16 CAD measured thresholds (black circles) shown in CIE xy space for observer SFR. The solid black curve is the contour of the fitted ellipse. The ellipse was measured for a target located at CIE xy: (0.265, 0.420) indicated by the cross. The non-fixed centre fitting algorithm calculated the ellipses centre to be located at CIE xy: (0.266, 0.419) indicated by the triangle.

2.3.3 Cone excitations and contrasts

When light emitted from the stimuli on the CRT display differs in spectral composition to the surrounding target field, these spectral differences are reflected in the excitation levels produced in each of the L-, M- and S-cones. The first step to determine the cone excitation values is the trivial conversion of the CIE xy chromaticity coordinates (small xy) of the chromaticity in question, displayed with a particular luminance level (L), into its corresponding CIE X, Y and Z tristimulus values (big XYZ), this is achieved using the triplet of standard CIE equations given by Eq. 2.1, 2.2 and 2.3 (Hunt, 1989), Eq. 2.2 indicates the relationship between the Y tristimulus parameter and luminance level, the units of which should be specified (cd m⁻² will be used throughout the following experiments).

$$X = \frac{Y}{y} x \quad \text{Eq. 2.1}$$

$$Y = L \quad \text{Eq. 2.2}$$

$$Z = \frac{Y}{y} (1 - x - y) \quad \text{Eq. 2.3}$$

Where, x and y are the CIE xy chromaticity coordinates of the stimuli (or foreground/background). If the stimulus has a spectral power distribution given by $I(\lambda)$ and the spectral sensitivities of the L-, M-, and S-cones are given by $L(\lambda)$, $M(\lambda)$, and $S(\lambda)$ then the photon absorptions rates $L_{\text{absorption}}$, $M_{\text{absorption}}$, and $S_{\text{absorption}}$ of the L-, M-, and S-cones for a stimulus composed of the spectrum $I(\lambda)$ can be defined as by Eq. 2.4, 2.5 and 2.6, respectively.

$$L_{\text{absorption}} = \int_{390}^{830} I(\lambda) L(\lambda) d\lambda \quad \text{Eq. 2.4}$$

$$M_{\text{absorption}} = \int_{390}^{830} I(\lambda) M(\lambda) d\lambda \quad \text{Eq. 2.5}$$

$$S_{\text{absorption}} = \int_{390}^{830} I(\lambda) S(\lambda) d\lambda \quad \text{Eq. 2.6}$$

Each integral has limits from 390 to 830 nm corresponding to the visible portion of the electromagnetic spectrum and $L(\lambda)$, $M(\lambda)$, and $S(\lambda)$ are the Stockman-Sharpe cone sensitivity curves (Stockman, Sharpe and Fach 1999 ; Stockman and Sharpe, 2000).

A 3 x 3 transformation matrix (Q) can be derived that is capable of converting a triplet of X, Y and Z tristimulus values into a set of L-, M- and S-cone excitations. The transformation matrix Q is produced by multiplying the spectral power

distributions of the red, green, and blue phosphors ($R(\lambda)$, $G(\lambda)$ and $B(\lambda)$, respectively) of the CRT display and the Stockman-Sharpe L-, M- and S-cone fundamentals ($L(\lambda)$, $M(\lambda)$, and $S(\lambda)$, respectively) over the visible spectrum (this was done in 1 nm intervals of λ). The XYZ tristimulus values can then be transformed into their corresponding L_{ex} -, M_{ex} - and S_{ex} -cone excitations by simply multiplying by matrix Q, see Eq. 2.7 (Golz, 2003; Brainard, 2002).

$$\begin{bmatrix} L_{ex} \\ M_{ex} \\ S_{ex} \end{bmatrix} = Q \begin{bmatrix} X \\ Y \\ Z \end{bmatrix} \quad \text{Eq. 2.7}$$

$$\text{where; } Q \sim \begin{bmatrix} 0.17 & 0.53 & -0.02 \\ -0.16 & 0.49 & 0.04 \\ 0.02 & -0.04 & 1.04 \end{bmatrix}$$

The inverse matrix Q^{-1} (Eq. 2.8) can be used for the reverse transformation, i.e., the conversion of L-, M- and S-cone excitations to X, Y and X tristimulus values.

$$\begin{bmatrix} X \\ Y \\ Z \end{bmatrix} = Q^{-1} \begin{bmatrix} L_{ex} \\ M_{ex} \\ S_{ex} \end{bmatrix} \quad \text{Eq. 2.8}$$

Within the field of vision science the concept of contrast is usually defined in three common ways; Michelson (Michelson, 1927), root-mean-square (Peli, 1990) and Weber (Whittle, 1994) contrast (see chapter 1). When defining the L-, M- and S-cone contrasts in the following experiments the Weber contrast method is always employed. This is the most appropriate method of defining contrast values when considering a small stimulus (subscript: 'stimulus') against a larger foreground/background field with a constant and uniform luminance (subscript: 'bg'). The L-, M- and S-(Weber) cone contrasts ($L_{contrast}$, $M_{contrast}$ and $S_{contrast}$, respectively) are defined by Eq. 2.9, 2.10 and 2.11;

$$L_{contrast} = \frac{L_{stimulus} - L_{target}}{L_{target}} \quad \text{Eq. 2.9}$$

$$M_{contrast} = \frac{M_{stimulus} - M_{target}}{M_{target}} \quad \text{Eq. 2.10}$$

$$S_{contrast} = \frac{S_{stimulus} - S_{target}}{S_{target}} \quad \text{Eq. 2.11}$$

The subscripts 'stimulus' and 'target' represent the excitations produced in that particular cone class by a particular stimulus and target chromaticity combination (or stimulus and background, if the target and background are equal). Using this CIE xy to cone contrast transformation method, the colour detection thresholds measured in the CIE xy colour space can be converted into either an opponent (L-M vs. S) relative cone excitation or cone contrast space. Fig. 2.9(a), (b) and (c) show an example of a measured threshold ellipse plotted CIE xy, a relative cone excitation and cone contrast space, respectively.

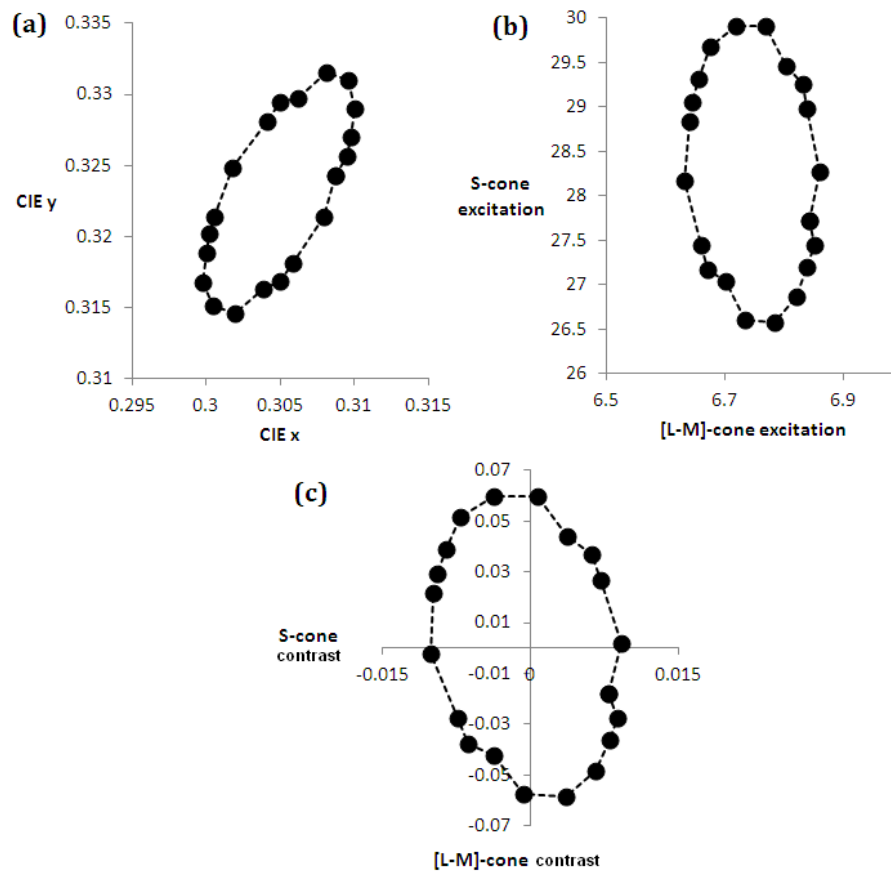


Fig. 2.9(a), (b) and (c)

Examples of measured threshold data plotted (a) the CIE xy colour space, (b) a relative cone excitation space and (c) cone contrast space.

2.3.4 Cone contrast curves

In order to visualise individual cone contrasts, cone contrast curves can be used. These are plots that show the three L-, M- and S-cone contrasts as a function of chromatic angle. They can be calculated for ellipses in any colour space that an ellipse can be displayed in. Fig. 2.10(a) shows the L-, M- and S-cone contrasts curves obtained from the threshold data displayed in Fig. 2.9(a). Fig. 2.10(b) shows the L-, M- and S-cone contrasts for the same set of thresholds but for the angles as defined by the ellipse in Fig. 2.9(c), i.e., an ellipse in L-M vs. S opponent

cone contrast space. In Fig. 2.9(a) an angle of zero degrees refers to the positive CIE x-direction. The minimum of the S-cone excitation curve occurs at approximately 62 and 242°. The minima at 62° corresponds to the maximum negative S-cone contrast and represented detections being made in the yellowish CIE colour direction, the maxima at 242° corresponds to the maximum S-cone contrast and represented detections being made in the bluish CIE colour direction, both relative to the target chromaticity at CIE xy: (0.305, 0.323). At these points the L- and M-cone contrasts are approximately zero, implying no L- or M-cone contrast is required and the S-cones in isolation are making the detection. Detections in the greenish and reddish colour directions, with respect to the target are made within the regions from approximately 110° to 200° (greenish) and 310° (wrapping around passed 360°) back to 40° (reddish), respectively. In these regions the L- and M-cone contrasts remain relatively constant, while the S-cone is shown to be at most half its peak values. Fig. 2.10(b) plots the variation of L-, M- and S-cone contrasts as a function of cone contrast space angle; zero degrees is defined by the positive [L-M]-cone contrast direction. It can be observed that the S-cone contrasts minima and maxima values lie at 90 and 270°, respectively; these directions correspond to S-cone detections in the yellowish (-S) and bluish (+S) colour directions, the S-cones are active in isolation from the L- and M-cones at both of these points. It can be noted that the S-cone maxima and minima are broader when plotting the cone contrasts as a function of CIE colour angle and the regions between these points the L- and M-cone contrasts are less parallel.

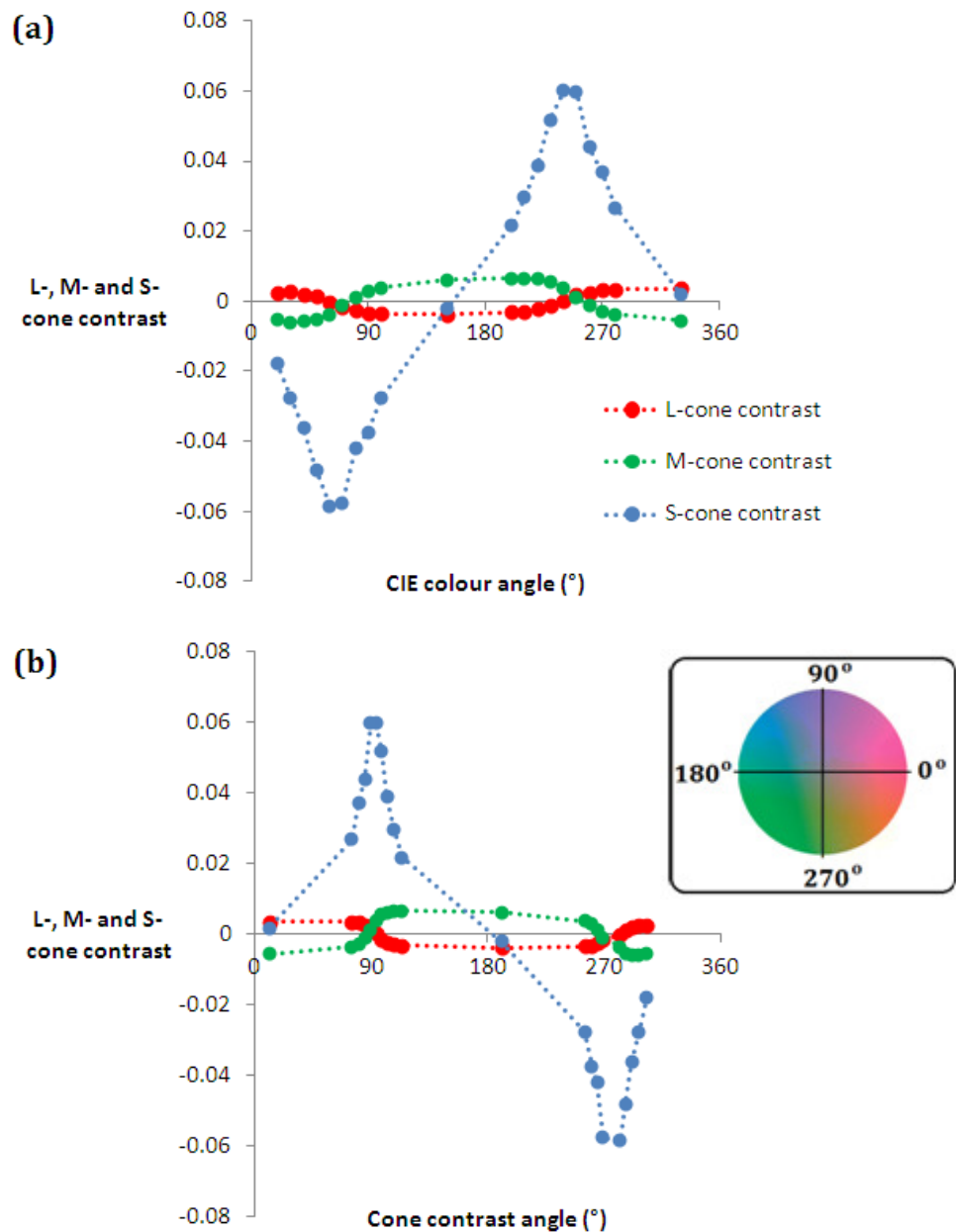


Fig. 2.10 (a) and (b)

L-, M- and S-cone contrast curves as functions of (a) CIE and (b) cone contrast colour angle, respectively. The insert indicates the approximate colours for each direction in cone contrast space.

2.4 P_scan-100 pupillometry system

The P-Scan-100 pupillometry system (Barbur *et al.*, 1987) was initially designed and realised in order to measure and track pupil size and direction over time. In

the investigation presented later in Chapter 7 it was employed to record the steady state pupil size (diameter) produced when observers view a series of chromaticities over a range of light levels. The 'head box' described earlier in the chapter where observers' position their head during the CAD test (Fig. 2.1) contains the hardware for this system. An infrared light source consisting of pulsed light emitting diodes (LEDs) were arranged in such a way as to illuminate the observers' pupil but minimise the reflections from the cornea. Images of the eye were recorded, at a rate of 20 Hz, using a photon camera and relayed to a video processing adapter board slotted directly into the controlling desktop PC. In order to segment the pupil from within each image the system relies on the difference in intensity between the pupil and iris; the system extracts the coordinates along the pupil-iris border from within 64 pre-selected monitor scan lines, these values are stored for use during the pupil size calculation. This data representing the circular contour of the pupil had best fitting circles applied to it in order to obtain an estimate of the pupil diameter. In order to measure the steady state pupil size a series of images are obtained over a few thousand milliseconds, during this time the pupil size will fluctuate so a mean value is calculated from the total of the images recorded (along with an associated standard deviation).

2.5 The macular assessment profile (MAP) test

The experiment presented in Chapter 6 required a measure of individual observers macular pigment optical density (MPOD); in order to obtain these measurements a heterochromatic flicker photometry (HCFP) technique was employed. The Macular Assessment Profile (MAP) test was implemented on a CRT display and

provides a rapid and convenient means to MPOD (Barbur, *et al.*, 2010; Rodriguez-Carmona *et al.*, 2006). The MAP test uses an optical notch filter to separate the outputs of the three RGB phosphors of the CRT display into two components. One component is absorbed maximally by the macular pigment (MP) and is derived only from the spectrally modified blue phosphor gun: the 'test beam'. The other is based on a combination of red and green phosphor luminances and consists largely of long-wavelength light that is not absorbed by the MP: the 'reference beam'. The luminance of the reference beam is set at 20 cd m⁻² and its modulation depth is fixed at 20%. The MAP test makes use of the advantages of the visual display to produce stimuli of varying size at a number of randomized locations, generating counter-phased sinusoidal modulations of the two stimulus beams. The frame rate of the display was 140 Hz and the stimulus modulation frequency was 15 Hz. The high temporal modulation frequency employed ensures that at threshold the activity of the luminance flicker detection mechanism that relies only on the L and M cone signals is isolated. The stimulus was presented as a short burst of flicker of approximately 500 ms duration and the observer's task was to simply report the presence or absence of perceived flicker. A modified staircase procedure with variable step sizes was used to measure the mean luminance of the test beam needed to cancel the perception of flicker generated by the reference beam. The MAP test was used to measure the MPOD along a number of specified locations from -7.8° to +7.8° eccentricity. The test stimulus changes from a disc of 0.36° diameter when presented at the fovea, to a sector annulus when presented at one of six discrete locations on either side of fixation across the horizontal meridian: ±7.8°, ±6.8°, ±3.8°, ±2.8°, ±1.8° and ±0.8°. The width of the test annulus also increases systematically with eccentricity to facilitate the detection and the nulling of luminance flicker. Fig. 2.11 shows examples of the stimulus when presented at

fixation (a), at $+1.8^\circ$ (b) and $+7.8^\circ$ (c); four guides are shown that assist the observers to maintain fixation which are present on screen throughout the testing procedure.

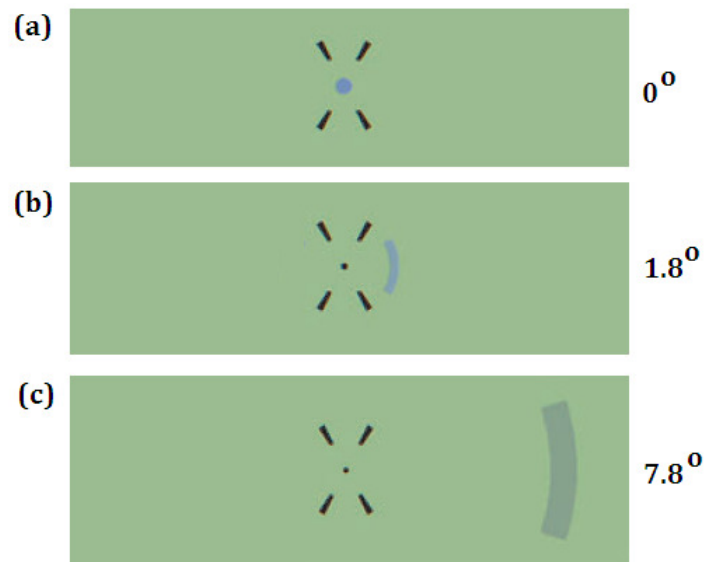


Fig. 2.11(a), (b) and (c)

Examples of the MPOD system stimulus presented at a series of eccentricities: (a) zero, (b) $+1.8^\circ$ and (c) $+7.8^\circ$ (c). Image adapted from Barbur et al. (2010).

Five set of randomly interleaved, repeat measurements were taken at each spatial location investigated, and these values are referenced with respect to 7.8° eccentricity; this is based on the assumption that the MP density at 7.8° is negligible. The test was performed at a viewing distance of 70 cm and the stimulus was presented only to the right eye. Similar measurements made with the left eye confirmed previous findings showing a positive correlation in MPOD values between the two eyes of a single observer (Robson *et al.*, 2003). The MAP test was validated (Barbur, *et al.*, 2010) against MP measurements using a modified

Moreland anomaloscope (Moreland and Kerr, 1979). This instrument employs a narrow, short-wavelength beam with a peak output at 460 nm measuring the peak MPOD. The MAP test, on the other hand, employs a broader, short-wavelength beam slightly underestimating the peak MPOD. A simple photometric model that predicts how the mean optical density of the MP, measured with the MAP test, relates to its peak density (i.e., the optical density at 460 nm), was developed. Following correction for peak optical density, the results obtained on the two instruments were found to be in close agreement (Rodriguez-Carmona, 2006). Fig. 2.12 shows an example of the variation of measured MPOD as a function of eccentricity for a typical observer. Two useful parameters are extracted from these profiles and form the basis of the analysis in chapter 6, they are the peak MPOD value (MP_{peak}) and the mean MPOD over the central 2.8° of visual angle ($MP_{2.8^\circ}$).

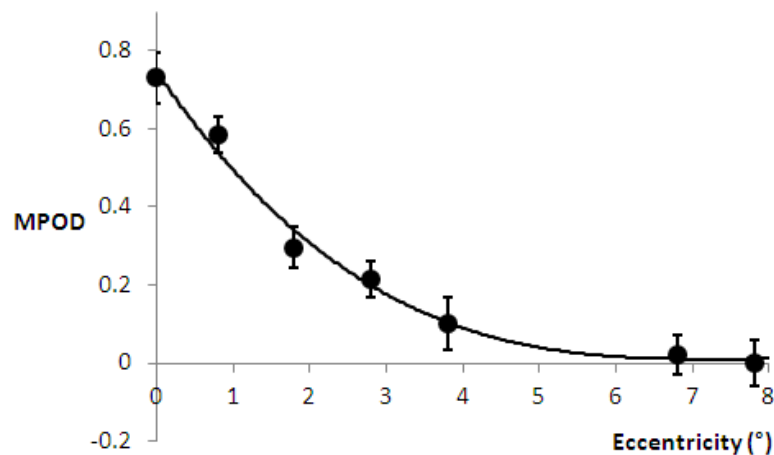


Fig. 2.12

An MPOD profile for an observer with a higher than average peak MPOD, in the range from zero (peak MPOD) to 7.8° eccentricity (\sim zero MPOD).

Chapter 3

Colour detection thresholds as a function of chromatic adaptation and light level

3.1 Introduction

This chapter describes how colour threshold discrimination ellipses were measured for several states of chromatic adaptation and for a range of luminance levels using the Colour Assessment and Diagnosis (CAD) test. An analysis of these results was carried out by examining the cone excitation and contrast changes required for threshold along the four cardinal cone excitation signal directions ($\pm[L-M]$ and $\pm S$). These directions correspond roughly to reddish ($+[L-M]$), greenish ($-[L-M]$), bluish ($+S$) and yellowish ($-S$) chromaticities, but do not correspond to the directions in colour space corresponding to unique red, green, blue and yellow (Wuerger *et al.*, 2005). The results reveal a strong linear relationship between the excitations induced by the adapting background field in each cone class and the corresponding changes needed for threshold detection. These findings suggest that the cone excitation change for threshold detection of colour signals is always the same for a given background excitation level (in any cone class); independent of the excitations generated in the other cone classes. These observations are then used to develop a model to predict colour detection thresholds for any specified background luminance and chromaticity within the

range of values investigated in this study ($0.3 \leq \text{luminance} \leq 31 \text{ cd m}^{-2}$) and chromaticities within the gamut of a typical CRT displays over that luminance range.

3.2 Background

When the light reflected from an object differs in spectral composition to the surrounding background field, these spectral differences are reflected in the excitation levels produced in each class of photoreceptor. The colour discrimination performance of the human eye is strongly affected by both the luminance level and the spectral composition of the adapting light (Yeh *et al.*, 1993; Yebra *et al.*, 2001). Knowledge of the limits of colour discrimination is important in setting safety standards and guidelines in visually-demanding workplace environments, for example in aviation, rail and maritime transport. Varying conditions of illumination and chromatic adaptation are employed in different working environments; these conditions will affect chromatic detection (Loomis and Berger, 1979; Hita, 1989). It is therefore of both fundamental and practical interest to be able to predict accurately how a subject's colour detection performance changes with light level and chromatic adaptation. These threshold variations are analysed in terms of changes in L-, M- and S-cone excitation levels required for threshold in the red, green, yellow and blue colour directions.

3.3 Selection of background chromaticities and luminance levels

Two main factors determined the choice of chromaticities for the twelve backgrounds employed in this study. The first was the chromaticities and the output luminance range of each of the monitor phosphors. At higher luminance levels the gamut of chromaticities available is reduced (Morovic, 2008) and this limits the choice of background chromaticities for which colour detection thresholds could be measured. The second factor is the massive increase in colour detection thresholds at lower luminance levels (Walkey *et al.*, 2001). This increase can cause the thresholds to fall outside the gamut of the display. The twelve background chromaticities were chosen to cover as much of the display gamut as possible within its chromaticity and luminance limits, while also ensuring that the measured colour detection thresholds fall within these limits. Colour threshold ellipses could be measured for nearly every selected background in the range 1 to 31 cd m⁻². At the lowest light level investigated, 0.3 cd m⁻², only four of the 12 backgrounds could be measured. A spectrally calibrated neutral density filter of optical density 1 log unit was employed when testing at luminance levels of 3 cd m⁻² and below.

3.4 Experimental procedure and data processing

Four subjects took part in this study; all had normal colour vision according to the CAD test. All subjects had 6/6 vision or better and wore appropriate refraction

lenses if required. Each observer carried out a CAD test run for each background chromaticity and luminance level employed in the study. Ninety seconds of adaptation to the uniform background field preceded the tests, in addition, for the lowest background luminance levels ($<3 \text{ cd m}^{-3}$), subjects dark adapted for 20 minutes first. The testing was carried out over a number of sessions of ~ 45 minutes each. For each background and luminance level, the measured thresholds were averaged for each of the 16 colour directions tested, collapsed over all subjects. The measured ellipses become asymmetric at the very low light levels, mainly due to an increased threshold in the yellow direction, as also shown previously by Brown (1951). These observations reflect differences in sensitivity for increments and decrements in S-cone signals at low light levels (Walkey *et al.*, 2001; Yebra *et al.*, 2001). The non-fixed centre ellipse fitting algorithm (Fitzgibbon *et al.*, 1999) was applied to the mean raw thresholds for each condition; this preserved any asymmetric elongations. This yielded a result set containing the semi-major ellipse axis (a), the semi-minor ellipse axis (b), the orientation (θ) of the semi-major axis relative to the abscissa and the fitted ellipse centre coordinates (x_0, y_0). R_t, G_t, B_t and Y_t were then calculated for each ellipse using standard parametric ellipse equations Eq. 3.1(a) and Eq. 3.1(b) (Salomon, 2005), where θ is the ellipse orientation and t is any angle in the range $0 \leq t \leq 360^\circ$.

$$X(t) = x_0 + a \cos(t) \cos(\theta) - b \sin(t) \sin(\theta) \quad \text{Eq. 3.1(a)}$$

$$Y(t) = y_0 + a \cos(t) \sin(\theta) + b \sin(t) \cos(\theta) \quad \text{Eq. 3.1(b)}$$

The yellowish, greenish, bluish and reddish thresholds being the colour directions

θ° , $(\theta+90)^\circ$, $(\theta+180)^\circ$ and $(\theta+270)^\circ$, respectively, relative to the background coordinates, in an anti-clockwise direction in CIE 1931 space. When transformed into [L-M] vs. S-cone excitation space, the reddish, greenish, bluish and yellowish threshold directions correspond to the cardinal directions $+[L-M]$, $-[L-M]$, $+S$ and $-S$, respectively. Fig.3. 1 shows the positions of these thresholds relative to the background chromaticity (x_{bg}, y_{bg}) in CIE xy space.

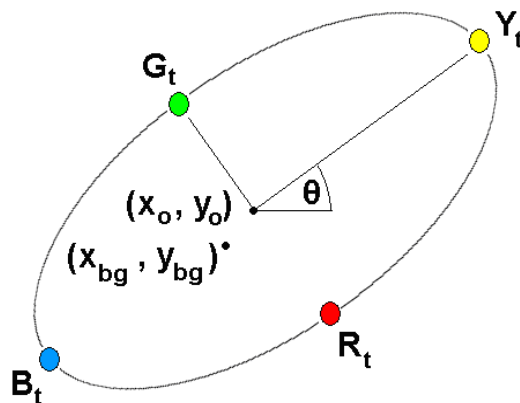


Fig. 3.1

Reddish, greenish, yellowish and bluish colour directions (R_t , G_t , Y_t and B_t) shown on a fitted ellipse contour. (x_o, y_o) are the CIE chromaticity coordinates of the fitted ellipse centre and (x_{bg}, y_{bg}) are the background/foreground CIE xy coordinates.

These four CIE threshold coordinates along with the CIE background coordinates (not fitted ellipse center co-ordinates) were transformed into their corresponding CIE XYZ tristimulus values (Hunt, 1998). These in turn, were then transformed into L-, M- and S-cone excitations using the method outlined by Golz and MacLeod (2003), see chapter 2. This method was verified by calculating cone excitations from first principles. The computation was performed by individually integrating the product of the L-, M- and S-cone fundamentals and the corresponding spectral radiance distributions needed to generate the specified background and

foreground chromaticities, over the visible spectrum. This procedure yielded the excitation in each cone class produced by foregrounds and backgrounds which were found to be within 0.5% of the corresponding values computed using the Golz and MacLeod matrix method.

3.5 Results

All mean CAD measured ellipses in CIE space were transformed into the [L-M]- vs S-excitation space and are shown in Fig 3.2. This plot shows the [L-M]- vs S-cone excitations in the horizontal plane as a function of background luminance (cd m^{-2}) over a series of isoluminant slices in the vertical plane. A linear model of cone excitation is assumed and hence the cone excitation proportions remain constant as the background luminance level varies, i.e., the relative values of L:M:S. This means that the ratio of [L-M]- to S-cone excitation will also stay constant. For a given background chromaticity the coordinates of the background excitations in the [L-M]- vs. S-cone excitation plane occur along a straight line as a function of background luminance. This curve will always point in the direction of the origin $([L-M], S, \text{Luminance}) = (0, 0, 0)$. Hence a diagonal straight line can be plotted through the 3D excitation space that represents a constant chromaticity, but varying luminance. This is illustrated by the black solid line in Fig. 3.2, for a whitish background located at CIE xy: (0.305, 0.323) over a range of luminance levels.

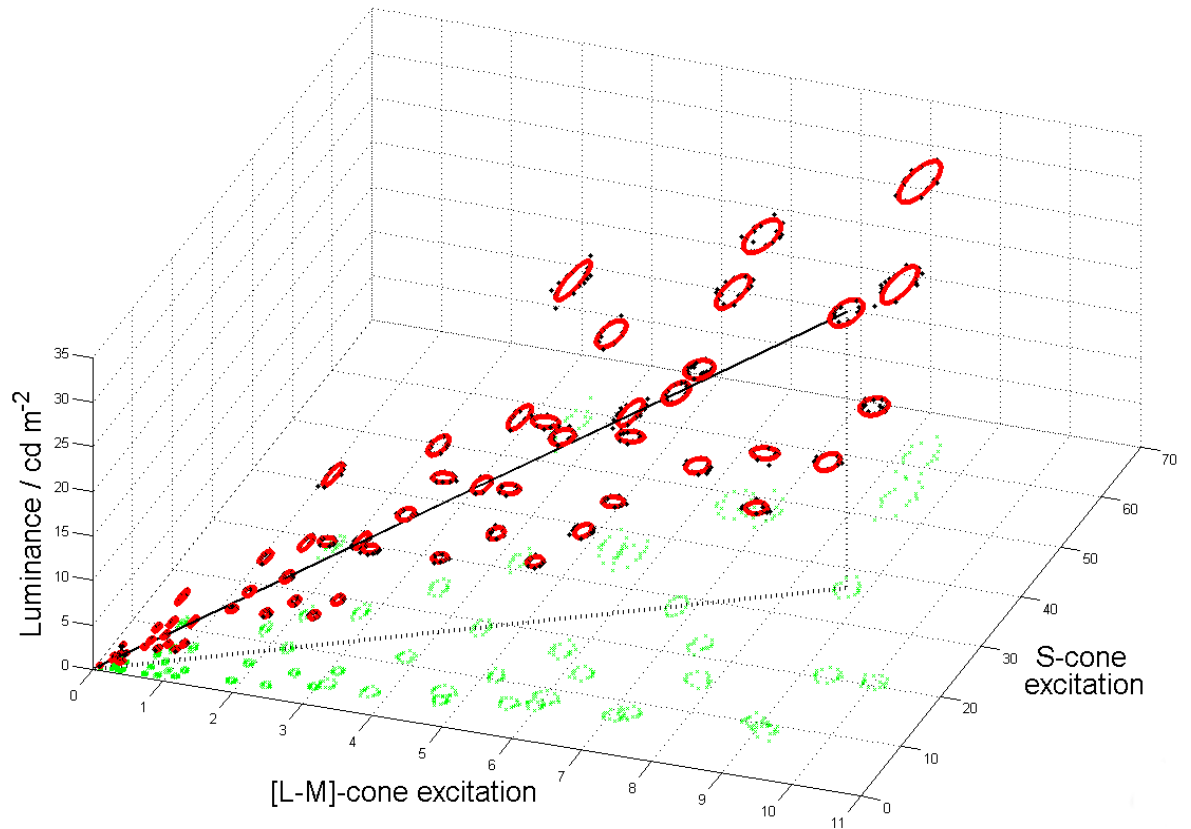


Fig. 3.2

Mean measured ellipse data ($n=4$) represented as [L-M]- vs. S-cone excitations plotted as a function of background luminance. The black dots represent the mean measured data; the green crosses represent the projection of these measured points onto the zero luminance plane for clarity. The fitted ellipses for each background are shown as red contours and the black solid line shows how points of constant chromaticity (CIE $xy: (0.305, 0.323)$) plot over different the luminance levels.

3.5.1 Variation in detection thresholds

The L-, M- and S-cone excitations were calculated for each background (L_b , M_b and S_b , respectively), at each luminance level, along with the corresponding L-, M- and S-cone threshold excitations (L_t , M_t and S_t , respectively) in the $\pm[L-M]$ and $\pm S$ directions of cone excitation space. These thresholds are defined by R_t , G_t , B_t and Y_t , respectively (as shown in Fig. 3.1).

3.5.2 L- and M-cones

The changes in L- and M-cone excitations required for threshold in the reddish +[L-M] direction are illustrated in Fig. 3.3. The x-axis represents the excitations produced in the L- and M-cones (L_b and M_b) by the different background chromaticities over the luminance range employed. The y-axis plots the increments in L- and M-cones needed to reach threshold (δL and δM , respectively, where $\delta L = L_t - L_b$ and $\delta M = M_t - M_b$). The slight clustering of the data points along the curves corresponds to the different background luminance levels tested.

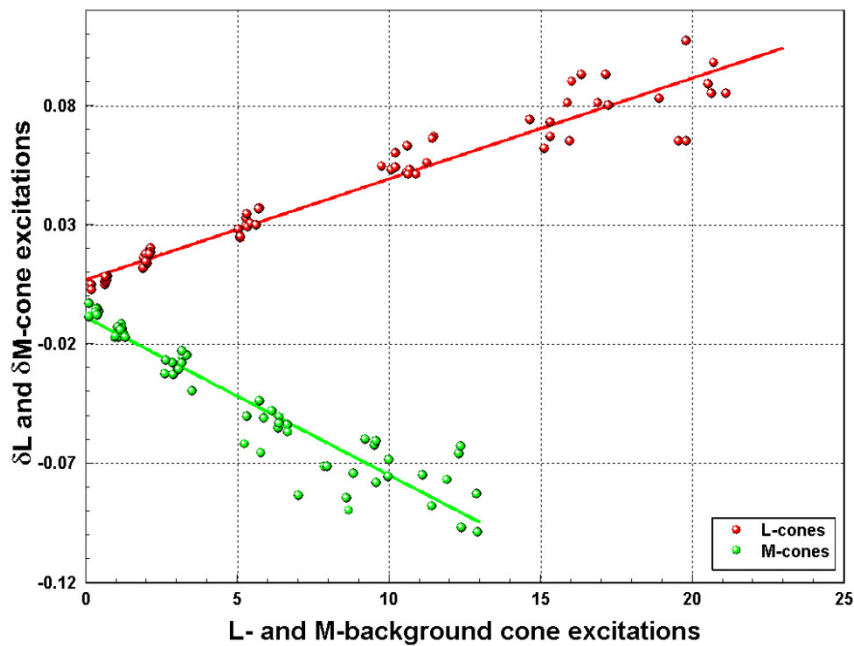


Fig. 3.3

The changes required in L- and M-cone excitations for threshold in the reddish colour direction versus the L- and M-cone excitations produced by the backgrounds.

The data show a strong linear relationship between the L- and M-cone excitations produced by the background and the corresponding excitation changes required

for threshold for all chromatic backgrounds and luminance levels in the measured range ($r^2 = 0.94$ and 0.90 for the L-cone and M-cones, respectively). Eq. 3.2 and 3.3 are based on Fig. 3.3 and are used by the model to predict the amounts by which the stimulus L-cone excitation must increase (Eq. 3.2) and the corresponding M-cone excitation must decrease (Eq. 3.3) to reach threshold in the reddish direction, both as a function of the background excitations.

$$\delta L(L_b) = 0.0042 L_b + 0.0071 \quad \text{Eq. 3.2}$$

$$\delta M(M_b) = -0.0066 M_b - 0.0086 \quad \text{Eq. 3.3}$$

Similar sets of curves were produced for the greenish $-[L-M]$ direction. From these plots Eq. 3.4 and 3.5 were determined; these equations predict the increments and decrements in M- and L-cone excitations, respectively, required to reach threshold when S-cone changes are absent or negligible.

$$\delta L(L_b) = -0.0044 L_b + 0.0084 \quad \text{Eq. 3.4}$$

$$\delta M(M_b) = 0.0069 M_b + 0.0081 \quad \text{Eq. 3.5}$$

Comparing the coefficients in these four equations (Eq. 3.2, 3.3, 3.4 and 3.5), it can be determined that for all background chromaticities and light levels tested, the L- and M-cone excitation changes required for threshold are approximately equal in magnitude, but opposite polarity in the reddish and greenish directions.

3.5.3 S-cones

Provided the relative S-cone excitation produced by the background is above ~ 9 excitation units (see x-axis of Fig. 3.4), the change in the excitation of S-cones needed to reach threshold in the bluish colour direction follow a similar linear relationship ($r^2=0.96$, $p<0.05$), see Eq. 3.6, as the L- and M-cones for the reddish/greenish colour directions. Below this value, the relationship between the S-cone excitation produced by the background and the change in S-cone excitation (δS) required for threshold can be described by the power curve give by Eq. 3.7 ($r^2=0.87$, $p<0.05$). The background luminance levels that produced these low excitations ranged from 0.3 to 24 cd m^{-2} ; this wide range is due to some background chromaticities being displayed at low luminance levels producing similar S-cone excitations to different background chromaticities displayed at high luminance levels. The two equations needed to predict the threshold excitation increments in S-cones as a function of background excitation for the yellowish direction are given below by Eq. 3.6 and 3.7.

$$\delta S(S_b) = 0.05 S_b + 0.64, \text{ for } S_b > 9 \quad \text{Eq. 3.6}$$

$$\delta S(S_b) = 0.32 S_b^{0.56}, \text{ for } S_b \leq 9 \quad \text{Eq. 3.7}$$

Fig. 3.4 plots the measured S-cone increments at threshold as well as the fits of Eq. 3.6 and 3.7. The corresponding changes in L- and M-cones in the bluish direction have also been calculated, they were shown to remain at zero over the whole range tested, i.e., they are independent of S-excitation increments. A similar set of equations was also produced to predict the S-cone excitation change required in the yellowish -S colour direction.

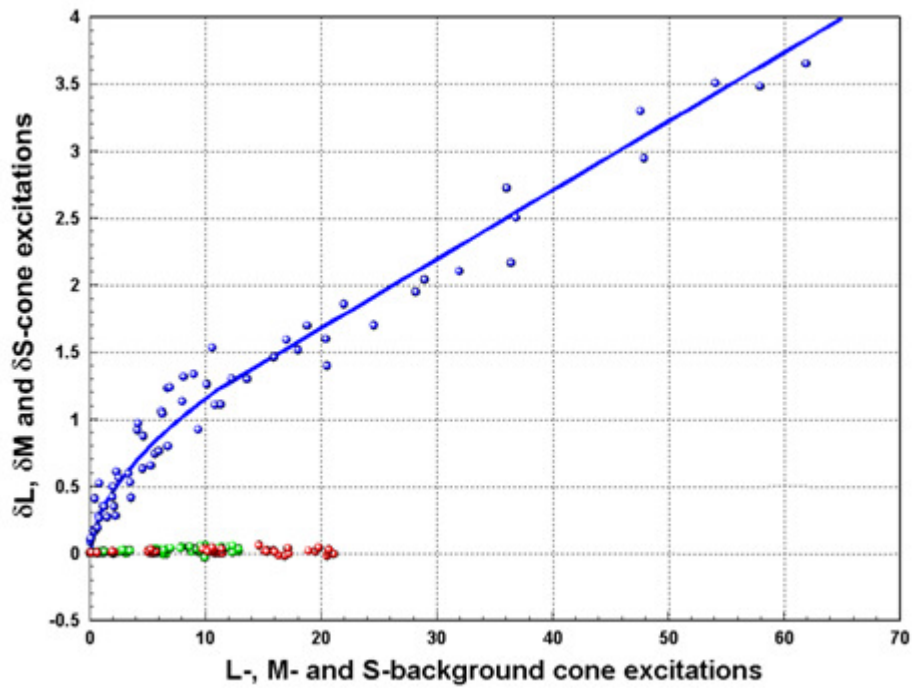


Fig. 3.4

Change in S-cone excitation required to reach threshold in the blue colour direction versus the S-cone excitations produced by the backgrounds. The blue colour direction represents the mean orientation of the major axis of the threshold detection ellipse measured for each of the four subjects investigated in this study. The curve obeys a linear relationship (see Eq.3.6) for relative S-cone excitations above ~ 9 and a power law relationship with a coefficient of 0.56 (see Eq.3.7) for cone excitations below this value. Note that the corresponding changes in L- and M-cones are approximately zero when thresholds are measured in the blue colour direction.

3.6 Reconstruction of ellipses

A model was constructed that attempted to predict the threshold ellipses. The orientation of the measured fitted ellipses in the [L-M]- vs. S-cone excitation space was found to be $90 \pm 1.1^\circ$ (mean \pm SD) relative to the +[L-M] axis. In view of this small variation the model always assumed the ellipse orientation in excitation space to be 90° ; this alignment of the semi-major axes parallel with the S-cone excitation axis is consistent with Boynton *et al* (1986). Along with the ellipse

orientation, the four thresholds in the $\pm[L-M]$ and $\pm S$ directions were calculated using the previously determined relationships that describe the changes in cone excitation required for threshold for each colour direction. Based on these four thresholds and the fixed 90° orientation, ellipse parameters could be calculated. When using Eq. 3.2 and 3.3 to predict the total $+ [L-M]$ excitation change in the reddish direction, the mean error between measured data and predicted threshold excitations was $8.9 \pm 6.2\%$ (mean \pm SD). The corresponding error in the greenish direction for the $- [L-M]$ excitation decrement was found to be $8.5 \pm 7.1\%$ (mean \pm SD). As the CIE 1931 diagram is popular and used in many industries (Shevell, 2003; Valberg, 1995) the ellipses were transformed back into CIE space for visualization using the inverse of the XYZ to LMS transformation matrix. Fig. 3.5, 3.6, 3.7 and 3.8 show the mean measured ellipse data (black dots) in CIE xy space for background luminance levels of 1, 3, 8 and 24 cd m⁻², respectively. The predictions of the model are shown in Fig. 3.5, 3.6, 3.7 and 3.8 as red contours.

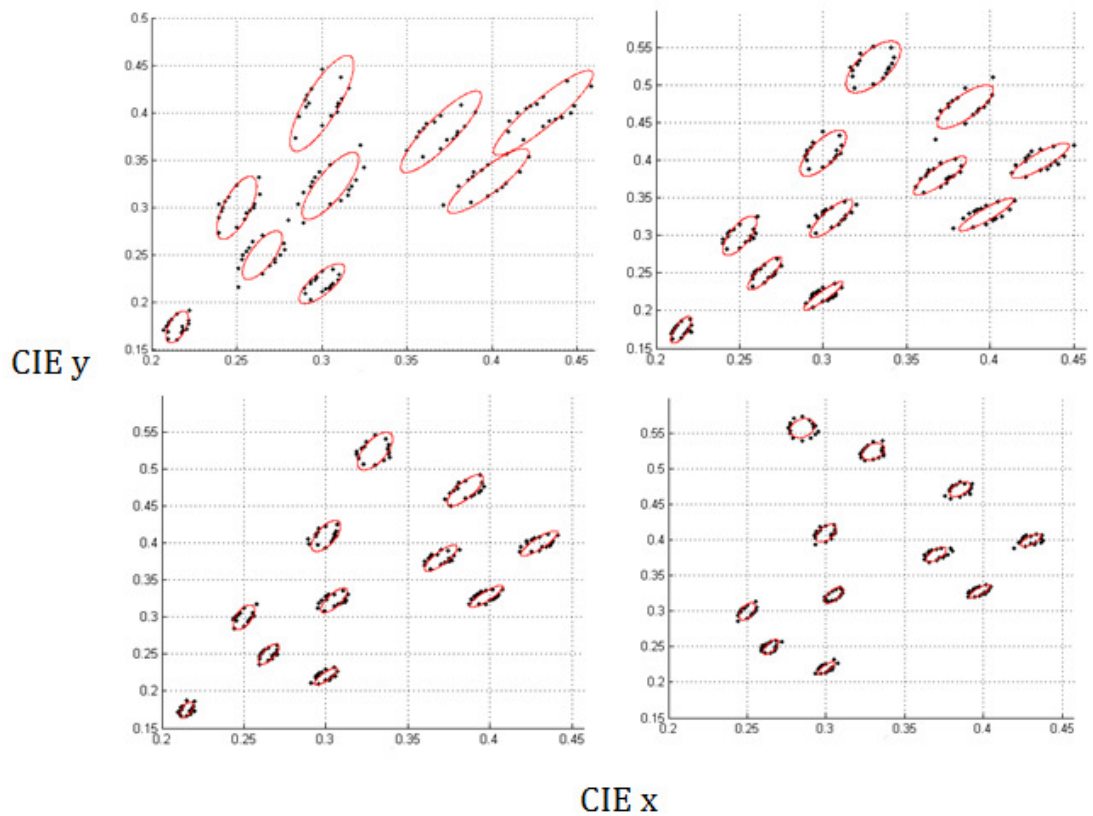


Fig. 3.5, 3.6, 3.7 and 3.8

The red contours show the predicted ellipses in CIE xy space, the mean measured are thresholds (black dots) are shown for comparison. The luminance levels shown are 1 cd m⁻² (top left), 3 cd m⁻² (top right), 8 cd m⁻² (bottom left) and 24 cd m⁻² (bottom right).

To assess the differences between the measured and predicted thresholds, the predicted cone excitations required for threshold for the points G_t , R_t , Y_t , B_t shown in Fig. 3.1 were compared to the corresponding excitations computed for the fitted data. The results reveal the smallest differences for the reddish colour direction and the largest differences for the yellowish directions, as outlined in Table. 1.

Colour Direction	Cone Class	Mean±SD (%)	Maximum Error (%)
Reddish	L	0.49±1.13	5.36
	M	1.27±2.80	13.13
	S	1.93±1.67	6.94
Yellowish	L	0.67±1.32	6.46
	M	0.74±1.46	7.34
	S	4.51±2.55	9.57

Table. 3.1

Mean and maximum L-, M- and S-cone excitation percentage errors for model predicted increments and decrements in the reddish +[L-M] and yellowish -S directions.

The maximum errors occur when predicting the threshold excitations for the lowest background luminance level (0.3 cd m⁻²). These errors combine when ellipses are predicted in CIE space. Fig. 3.9 shows the percentage differences between predicted and fitted ellipse parameters in CIE space as a function of background luminance. At luminance levels above 3 cd m⁻² there is no significant change in the accuracy of the predicted ellipse parameters. The mean errors for the predicted semi-major and -minor axes and also the ellipse orientation above 3 cd m⁻² are ~ 6.8%, 5.6% and 5.7%, respectively. Below 3 cd m⁻² the errors are larger, particularly for the ellipse semi-major axis; consistent with measured thresholds along this axis showing an increased inter-subject variability.

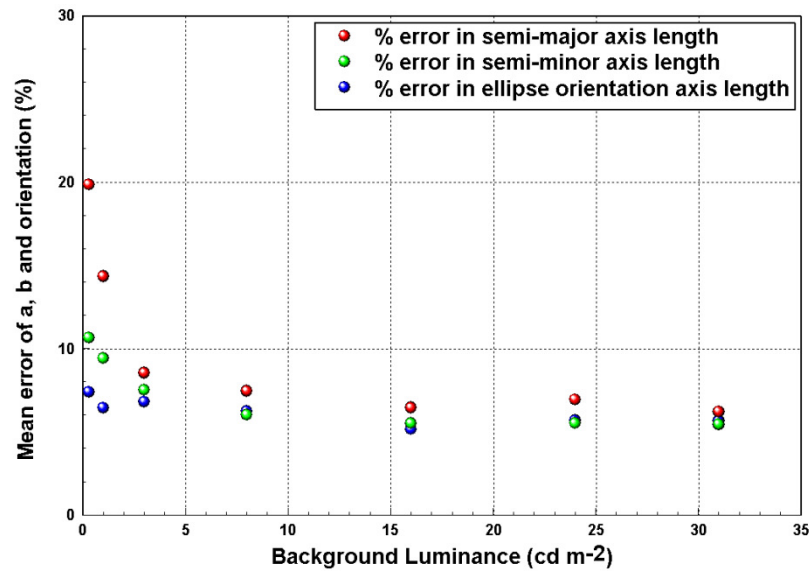


Fig. 3.9

The mean errors for each set of predicted ellipse parameters (when grouped by background luminance level). Each error reflects the difference between the measured and the corresponding prediction for that parameter based on the mean fitted ellipse. The large errors are restricted to the semi-major axis and reflect the larger inter-subject variability in S-cone threshold excitation.

3.7 Additional data for detections made at 24 cd m⁻²

An additional set of data was collected for the 24 cd m⁻² luminance condition. This was achieved by measuring detection threshold ellipses over the range of chromaticities initially measured at 24 cd m⁻² for an additional n=18 subjects. Fig. 3.10 shows the mean fitted detection ellipses for this n=18 group (black contours) along with the n=4 group (red contours) that participated in the full experiment. Note that for clarity the ellipses shown in Fig. 3.10 have been scaled up by a factor of 2 along the semi-major and -minor axes. Between the two groups no significant differences exist in terms of semi-major or -minor axis lengths, ellipse orientation, or (CIE x, CIE y) centre coordinates.

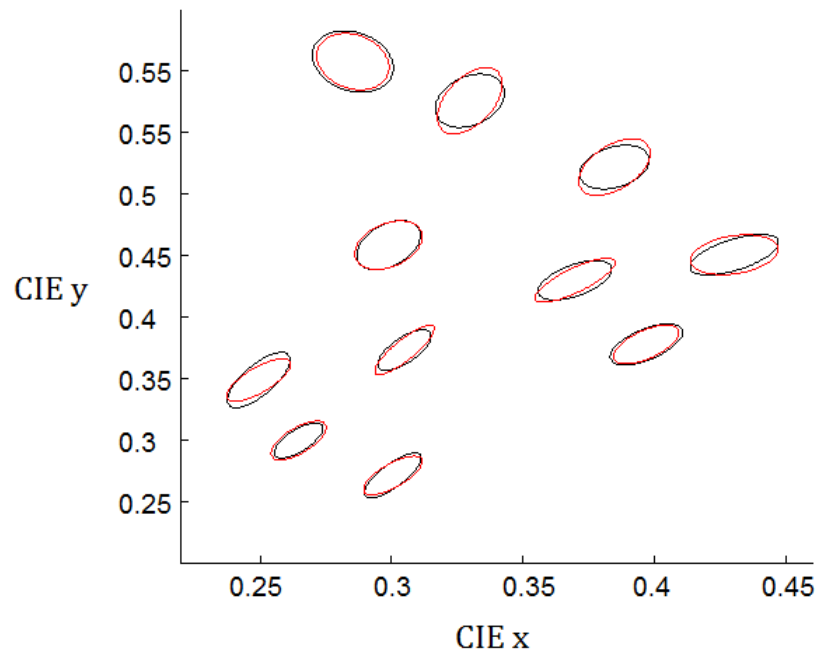


Fig. 3.10

Graphical comparison of mean ellipses for the $n=4$ subjects (red) and $n=18$ subjects (black) groups, no significant differences exist. All ellipses have been scaled along their semi-major and -minor axes for clarity by a factor of 2.

3.8 Comparison with MacAdam's ellipses

MacAdam performed an experiment in which observers made a series of colour matches (MacAdam, 1944). A fixed reference colour was presented and the observers' task was to adjust a second colour next to it in a 2° comparison field until it matched the reference colour. The observers made repeated colour matches, using the same reference colour, along different directions in colour space and the standard deviations of the matches for a number of colour directions were calculated. It was discovered that plotting the standard deviations with respect to the reference colour on the CIE 1931 chromaticity diagram produced an

ellipse. In total 25 reference colours were used, hence 25 ellipses were finally calculated from the data. The reference and test fields were presented at a luminance of approximately 48 cd m^{-2} ; over the course of the experiment it has to be assumed that some chromatic adaptation to the stimulus occurred. Performing the same analysis, as presented in section 3.7, on MacAdam's data, similar relationships between the excitations produced by the reference field and the change in cone excitations required to produce the standard deviation MacAdam measured in the reddish, greenish, yellowish and bluish colour directions were found. The luminance range used in this investigation was 0.3 to 31 cd m^{-2} , so it did not include any experimental measurements at 48 cd m^{-2} ; which was the luminance level MacAdam used. The above relationships were, however, used to predict ellipses at 48 cd m^{-2} in CIE xy space in order to test the validity of the relationships at this higher light level. There is a significant difference in size between MacAdam's ellipses and the ellipses measured using the CAD test. This is largely due to them being measures of different parameters; MacAdam's method produces a set of standard deviations estimated from repeated matches used to quantify thresholds, whereas the CAD test method measures colour detection thresholds using a four-alternative, forced-choice procedure based on two-down, one-up staircase method (Levine, 2000). It was found that the predicted ellipse for "MacAdam's white", located at CIE xy: (0.305, 0.323), was larger than the corresponding MacAdam's ellipse by a factor of ~ 4.5 , both along the semi-major and -minor axes. Fig. 3.11 shows the model-predicted threshold ellipses (red contours) and the scaled MacAdam's ellipses (black contours). No significant difference is found between the ellipse parameters (semi-major axis, the semi-minor axis and ellipse orientation in CIE xy space) for the predicted and MacAdam's ellipses once the scaling factor of ~ 4.5 is applied to each MacAdam

ellipse. This implies the model has validity above the measured 31 cd m^{-2} luminance level.

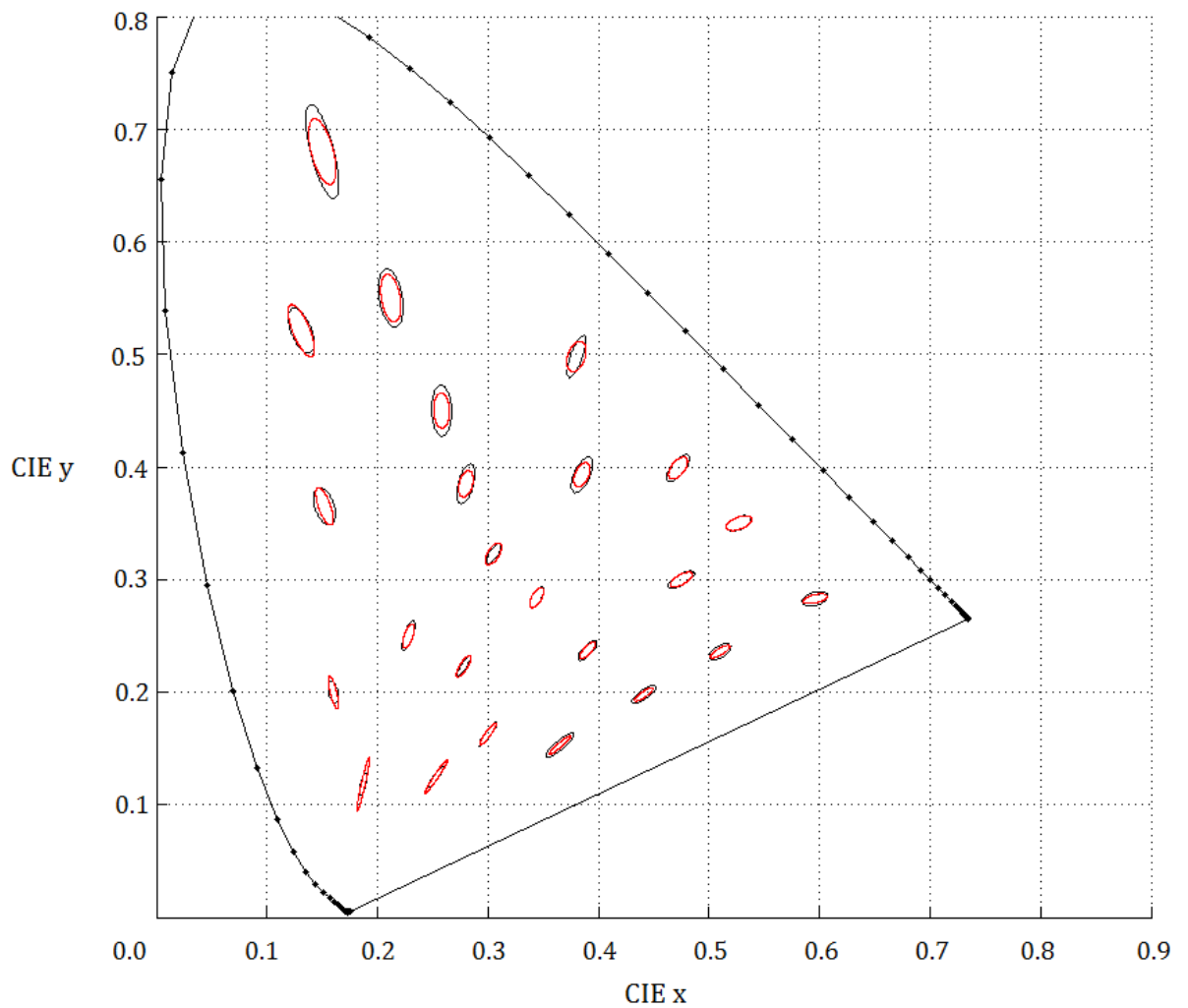


Fig. 3.11

CIE xy space showing the model predicted ellipses (red contours) and MacAdam's ellipse scaled up by a factor of 4.5.

3.9 Comparison with the Cambridge Colour Test

A dataset was supplied by Marcelo Fernandes Costa (University of São Paulo, Brazil), it was originally collected and used in a study on colour vision in adults and children (Ventura *et al.*, 2002). The dataset consists of a series of semi-major

and semi-minor ellipse axes and ellipse orientations for threshold ellipse measured using the Cambridge Colour Test for five different colour locations. The data were collected using a sample of 84 observers with an age of 29.3 ± 12.0 years (mean \pm SD) in the range 17 – 60. The measurements were made monocularly with 73 observers using their right eye. The Cambridge Colour Test uses the CIE 1976 v'u' colour space; the ellipses were therefore transformed from this space into the CIE 1931 xy space (see chapter 2) and compared to the model ellipse predictions for the same chromatic locations at an equal luminance level (29 cd m^{-2}). Fig. 3.12 shows the Cambridge Colour Tests measured ellipse (black contours) and the model predicted ellipses for the corresponding chromatic locations (red contours). A suitable single factor was not found that could scale all the Cambridge Colour Test measured ellipses to make them comparable to the predicted ellipses along both the semi- major and -minor axes. This is most clearly illustrated by the almost equal red-green threshold, but very different yellow-blue thresholds for the ellipse at CIE xy: (0.351, 0.342) (centre ellipse in Fig. 3.12). These differences are potentially due to two main factors. The first is the difference in methods for acquiring thresholds; the CAD test measures detection thresholds via the detection of a small moving chromatic stimuli, whereas the Cambridge Colour Test is more comparable to a visual search (with fixation) task where observers attempt to detect the gap of a Landolt-C. The second factor is that the state of chromatic adaptation will be different during blocks of testing using the Cambridge Colour Test as it does not use a chromatic background and the interleaved staircases will greatly reduce any adaptation to the target stimuli.

The monocular and binocular conditions employed between the two tests was considered as a possible explanation to account for some of the difference in threshold magnitudes and unequal [red-green]:[yellow-blue] ratios. It has, however, been previously shown for the Cambridge Colour Test that no significant differences arise due to monocular or binocular testing conditions, eye dominance or testing order (i.e., learning/practice does not affect the measured thresholds) (Ventura *et al.*, 2006). This is not, however, the case with CAD threshold ellipses which show lower thresholds under binocular viewing conditions.

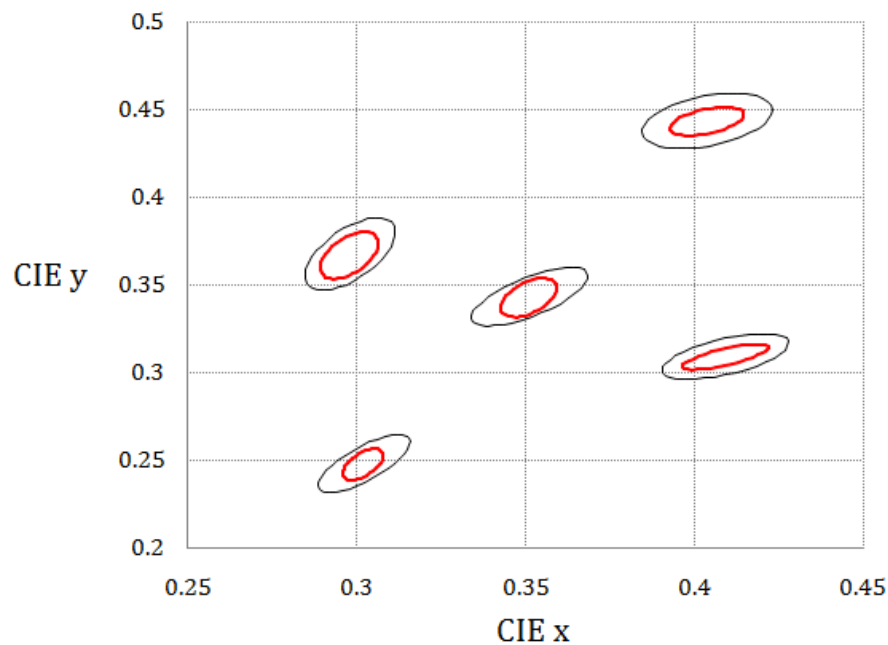


Fig. 3.12

The Cambridge Colour Test measured ellipses (black contours) shown in CIE xy space, along with the model predicted ellipses for the same chromatic locations and luminance.

3.10 Discussion and conclusion

It has been shown that even when the differences in chromatic adaptation are large, a strong linear relationship exists between the background L-, M- and S-cone excitations and the corresponding increments required for threshold in each colour direction over all or the majority of the luminance range tested. This corresponds to the linear relationships existing over at least 2 log units for the L- and M-cones and slightly less for S-cones, but a correction can be applied at low light levels to extend the predictive range of the model for the S-cone increments and decrements. Using these derived relationships it is possible to predict the cone excitations required for threshold detection of colour signals in the reddish, greenish, yellowish and bluish colour directions, at least within the chromaticity range and luminance levels associated with typical display applications. These excitations can be used to predict the discrimination ellipse parameters in CIE space with small errors of $\sim 6\%$ over most of the range. Predictions of yellowish and bluish thresholds are less accurate below 3 cd m^{-2} , but these thresholds also show larger inter-subject variability when measured experimentally.

At a high background luminance level, the L-cone excitations of the stimulus in the reddish and greenish colour directions need only increase/decrease by $\sim 0.4\%$ (see Fig. 2.10), but for threshold to be reached at the lower luminance levels the increase needed can be as large as $\sim 1.4\%$. The M-cone excitation of the stimulus also only requires a small change for threshold in the reddish and greenish directions. A change of only $\sim 0.65\%$ is required at the highest light levels, but at the lowest light levels this change can be as large as $\sim 2.3\%$. The S-cone excitation at threshold requires much larger changes typically an increase/decrease of $\sim 6\%$ relative to the signals generated in S-cones by the background for either the

yellowish or the bluish colour directions. However this change can be as large as ~25% for background luminance levels below 3 cd m⁻².

The data show that provided the background cone excitation in a particular cone class remains unaltered, changes in chromatic adaptation are equivalent to changes in luminance. For example, the L-, M- and S-cone excitations produced by the background CIE (x, y): 0.305, 0.323 at a luminance of 24 cd m⁻² are 15.98, 9.23, and 28.22, respectively. The L-, M- and S-cone excitations produced by the background CIE (x, y): 0.215, 0.175 at the lower luminance of 8 cd m⁻² are 5.31, 3.52 and 28.98, respectively. Due to this particular difference in chromaticity and luminance there is a large difference in the L- and M-cone excitations that the two backgrounds produce (33.2% and 38.1% respectively). These two conditions of chromatic adaptation produce almost identical S-cone excitations of 28.22 and 28.98 (a difference of only 2.6%). The S-cone excitation required for threshold in the blue colour direction for the first background is 30.17, and 31.02 for the second background (a difference of only 1.2%). There are also small differences between the S-cone excitation required for threshold in the red, green and yellow colour directions between the two states of 1.0%, 1.2% and 0.1%, respectively. These observations suggest that when threshold detection of coloured signals is involved, the state of chromatic adaptation only affects the measured thresholds through changes in absolute cone excitation levels. No significant interaction of signals generated in different cone classes is therefore involved. The result suggests that cone signal changes needed for threshold detection are always the same for a given background cone excitation level (in any cone class); and are independent of the excitation generated in the other cone classes.

Chapter 4

Effect of the adapting field on chromatic sensitivity

4.1 Introduction

This chapter describes how the investigation performed in chapter 3 was extended to examine how colour detection thresholds change in different colour directions for combinations of adapting background fields and foregrounds of differing chromaticities. The method employed for measuring these threshold ellipses is similar to the method described in chapter 3. The Colour Assessment and Diagnosis (CAD) test was used following the procedure described in chapter 2 except two parameters were varied;

- The background adapting field was isoluminant (24 cd m^{-2}), but not of an equal chromaticity relative to the foreground; this allowed investigation of any effect this difference would have on the ellipse parameters.
- A delay was added between each trial presentation to ensure the subject had sufficient time to re-adapt to the background field chromaticity and were not actually chromatically adapting to the foreground chromaticity (see re-adaptation time control experiment, section 4.2).

It was found that using an isoluminant adapting field and foreground combination that differed in chromaticity greatly affected the magnitude of detection thresholds and orientation of detection ellipses; this is consistent with and extends some earlier findings reported by Krauskopf and Gegenfurtner (1999).

4.2 Re-adaptation time control experiment

A control experiment was performed to determine the delay time required between each trial presentation. This was to ensure the observers remained adapted to the background field and to minimise any chromatic adaptation to the foreground during each CAD presentation, ensuring the subject remained chromatically adapted to the background chromaticity. The adapting field chromaticity used to test this was CIE xy: (0.305, 0.323) and the foreground chromaticity was a greenish colour at CIE xy : (0.285, 0.558). Detection ellipses were measured for a series of different delay times between each trial presentation from 0 to 3000 ms; during this delay the observers were exposed only to the uniform background. The measured detection ellipses are shown, in CIE xy space, in Fig. 4.1. The smallest central black ellipse is shown for comparison and is the measured ellipse produced when both the background and foreground are located at CIE xy : (0.285, 0.558). Note the top left side thresholds for the 1000, 2000 and 3000 ms delay ellipses appear unchanged; this is simply due to the display gamut limit being reached in this direction (indicated by the black solid line). The results show that as the delay between presentations increases (and hence the time available to re-adapt to the background adapting field increases), the measured thresholds increase. The measured thresholds are shown to increase until the delay is 2000 ms, at which point they plateau. Based on this observation, a fixed 3000 ms delay between presentations of the foreground was introduced into the CAD testing procedure; during this delay the subject viewed the background adapting chromaticity only. This 3000 ms second delay meant that the foreground would only be displayed for ~25% of the time each CAD stimulus sequence was presented.

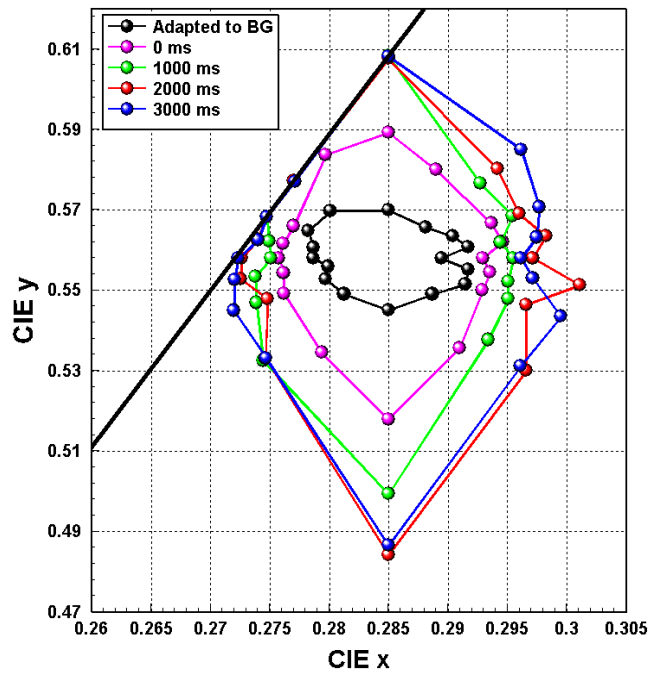


Fig. 4.1

Detection threshold ellipses measured for varying delay times between each CAD trail presentation. As the delay is increased the detection thresholds increase and then plateau at 2000 ms onwards. The black central ellipse was measured for comparison for the condition where the adapting field (BG) and foreground chromaticities were equal.

4.3 Method and data collection

A series of seven different adapting background field chromaticities were chosen. These were distributed over the available display gamut at 24 cd m^{-2} in order to maximise the spacing between them, while still allowing the entire detection ellipse to be measurable with the gamut. Before each CAD test run the subject was chromatically adapted to the background chromaticity, by exposing them to it for ~ 90 seconds. Fig. 4.2 shows the time course of one stimulus sequence; A: the

subject is exposed to 3000ms of the background adapting field only, B: the moving stimulus is displayed (~700ms), embedded in the foreground chromaticity grid of luminance noise, C: the background chromaticity only is displayed until the subject submits their response regarding the direction of motion of the stimulus; the subject is then exposed to another 3000 ms of the background only (A), in order to maintain chromatic adaptation to it. This is repeated until a threshold in each of the colour directions being tested has been demined (see chapter 1).

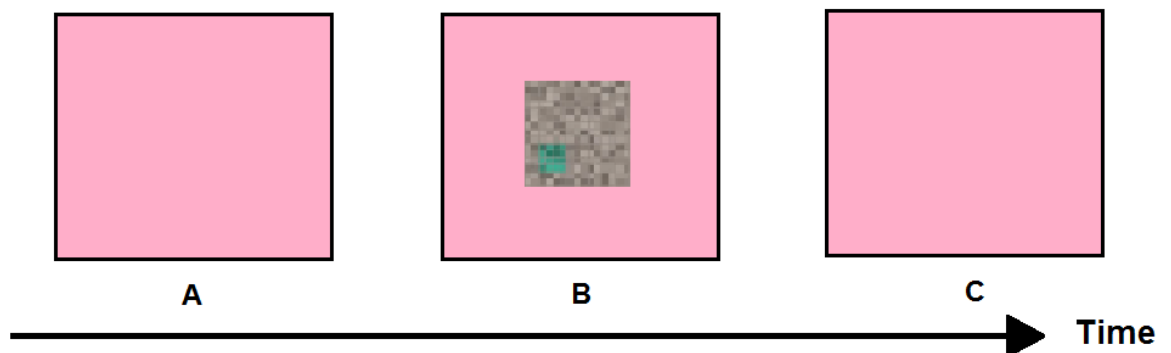


Fig. 4.2

The time course of a CAD stimulus sequence, A: forced 3000 ms adaptation to background, B: CAD stimulus displayed on foreground of luminance noise, C: wait for subject to respond.

Measuring a detection ellipse for each combination of foreground and background yielded a dataset of 42 (6x7) ellipses per observer. The added 3000 ms delay between each stimulus sequence increased the time taken to measure each detection ellipse from ~12 minutes to ~25 minutes.

4.4 Observer BJ

Due to the extended data acquisition time (>17 hours in total) only one observer took part in the study (the author BJ). Comparing BJ to the standard normal CAD observer (Barbur *et al.*, 2006), a difference in detection ellipses as measured at CIE xy : (0.305, 0.323) was found to be $\sim 3\%$ along both semi-major and -minor ellipse axes and $\sim 1^\circ$ in orientation, making them a close match in sensitivity.

4.5 Results

The results of the experiment reported in chapter 3 showed that when the foreground and background chromaticity are equal the measured detection ellipses were found to align themselves, along their semi-major axes, with the cardinal S-cone excitation axis. Detection ellipse parameters measured for combinations of different adapting background fields and foreground chromaticities were found to exhibit two main differences to those measured with equal background and foreground chromaticities. The first is an elevation of detection thresholds in all directions i.e., larger detection ellipses are produced (both major and minor axes). The second difference is that, depending on the relative direction between the foreground and background chromaticity, a large change in ellipse orientation can be observed. Fig. 4.3 illustrates this using two fitted ellipses in [L-M]- vs. S-cone excitation space. The black point corresponds to a whitish chromaticity at CIE xy : (0.305, 0.323) and the red point corresponds to a red at CIE xy : (0.3977, 0.3283). Both ellipses were measured using the red as the foreground. The black ellipse was measured with the background adapting field displayed set CIE xy : (0.305, 0.323) (white) while the red ellipse had the

background adapting field displayed as CIE xy: (0.3977, 0.3283) (red). The red ellipse shows (in agreement with chapter 3) that if the subject is adapted to a background field and makes detections based on a foreground of equal chromaticity then the measured ellipse will be aligned parallel to the cardinal S-cone excitation axis. For an adapting and foreground field combination that differ in chromaticity, the elevation of detection thresholds, along with the change in ellipse orientation relative to the cardinal axes is observed as illustrated by the black ellipse. The orientation shift more closely aligns the detection ellipse's semi-major axis towards the adaptation point; this is consistent with the results of Krauskopf and Gegenfurtner (1992).

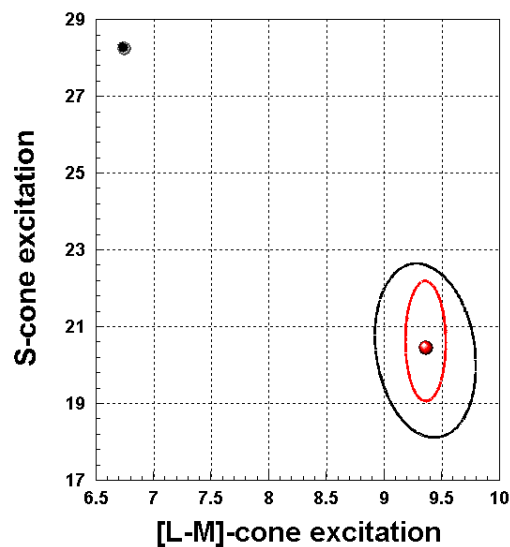


Fig. 4.3

Both the red and black ellipses, shown in cone excitation space, are the results of using a red foreground at CIE xy:(0.3977, 0.3283). The red ellipse is the result of using the same red for the background adapting field, the black ellipse is the result using a white adapting field located at CIE xy : (0.305, 0.323).

Fig. 4.4(a), (b) and (c) show three of the seven adapting background fields used, along with the six corresponding measured detection ellipses per adapting field displayed around their foreground chromaticity. The colour scheme used in Fig.

4.4(a), (b) and (c) approximately indicate the adapting field and foreground chromaticities.

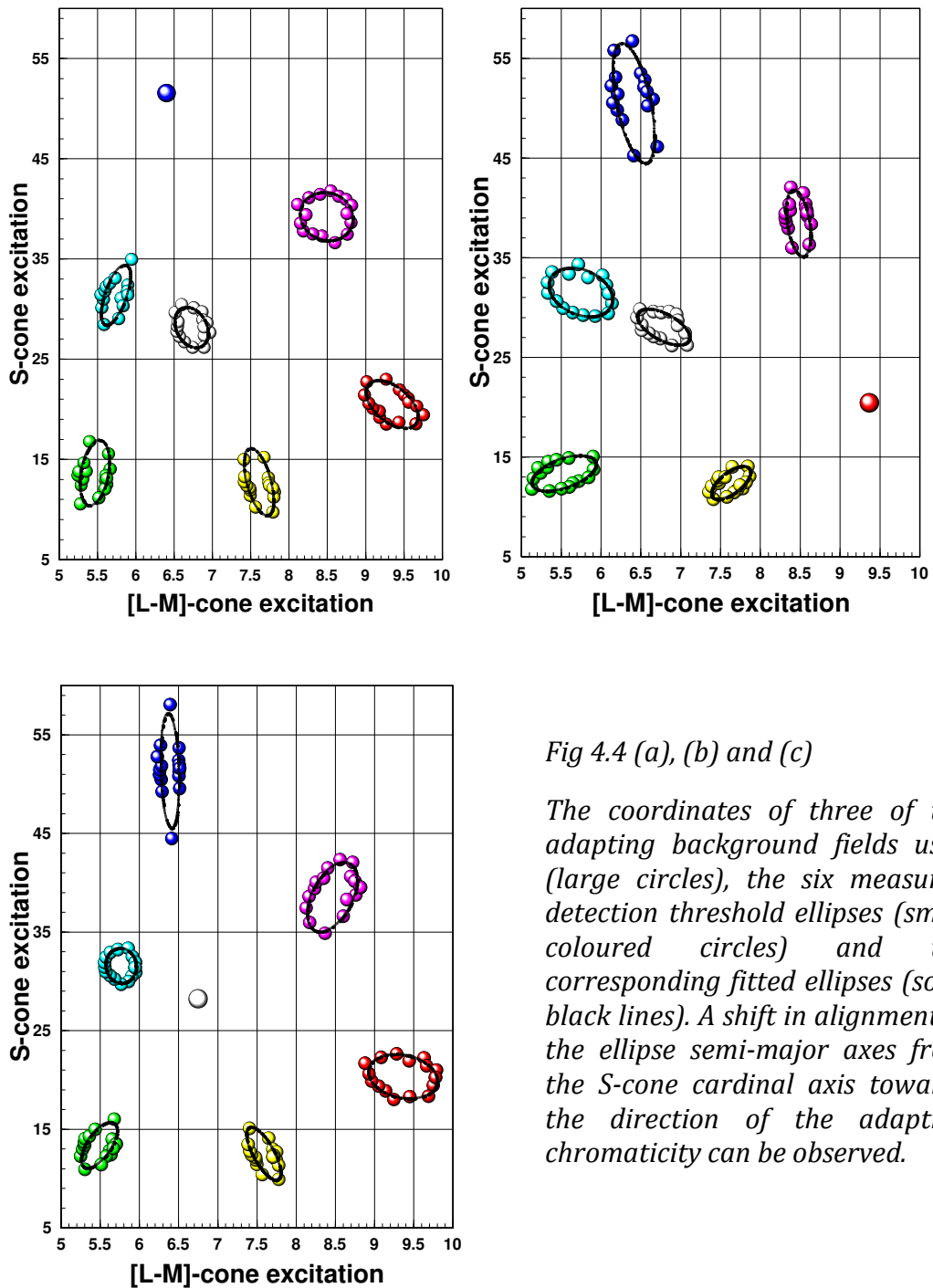


Fig 4.4 (a), (b) and (c)

The coordinates of three of the adapting background fields used (large circles), the six measured detection threshold ellipses (small coloured circles) and the corresponding fitted ellipses (solid black lines). A shift in alignment of the ellipse semi-major axes from the S-cone cardinal axis towards the direction of the adapting chromaticity can be observed.

4.5.1 Variation of thresholds along cardinal L-M and S axes

Ellipses were fitted to all measured data and four thresholds ($\pm\delta[L-M]$ and $\pm\delta S$) were calculated from them using the general parametric ellipse equations in cone excitation space. The calculated thresholds were defined such that the length of the straight line connecting the foreground coordinate and the surface contour of the ellipse (in both positive and negative, and parallel and perpendicular direction, i.e., $\pm\delta[L-M]$) thresholds are determined when $\delta S=0$ and $\pm\delta S$ thresholds when $\delta[L-M]=0$, with respect to the foreground coordinate. As some ellipses displayed a large asymmetry, the centre coordinate of the fitted ellipse did not necessarily equal the coordinate of the foreground chromaticity; the thresholds were always calculated relative to the foreground coordinates. The differences between the foreground and adapting field [L-M]- and S-cone excitations were also calculated parallel and perpendicular to the [L-M]-axis, respectively. An example of a fitted ellipse along with the adapting field and foreground chromaticities is illustrated in Fig 4.5. The difference between the adapting field and foreground excitations, in terms of [L-M]- and S-cone excitations ($[L-M]_{\text{for-ada}}$ and $S_{\text{for-ada}}$) along the cardinal excitation axes, are given by Eq. 4.1 and Eq. 4.2, respectively, where, the subscript $_{\text{ada}}$ refers to the adapting field, the subscript $_{\text{for}}$ refers to the foreground and the subscript $_{\text{for-ada}}$ refers to the difference between the adapting field and foreground.

$$[L - M]_{\text{for-ada}} = [L - M]_{\text{for}} - [L - M]_{\text{ada}} \quad \text{Eq. 4.1}$$

$$S_{\text{for-ada}} = S_{\text{for}} - S_{\text{ada}} \quad \text{Eq. 4.2}$$

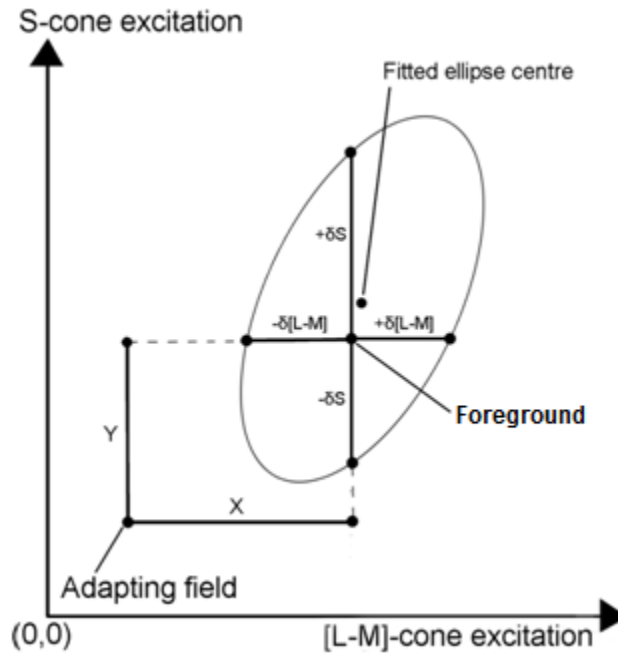


Fig. 4.5

An example of the coordinates of an adapting field and foreground combination are illustrated. The size and orientations of the $\pm\delta[L-M]$ and $\pm\delta S$ thresholds are illustrated with respect to the foreground chromaticity. The $\pm\delta[L-M]$ thresholds are defined as the distances from the foreground chromaticity to the ellipse surface (parallel to $[L-M]$ -cone excitation axis), the $\pm\delta S$ thresholds are defined as the distances from the foreground chromaticity to the ellipse surface (parallel to the S -cone excitation axis). X and Y represent the difference between the $[L-M]$ - and S -cone excitations of the adapting field and foreground ($[L-M]_{for-ada}$ and $S_{for-ada}$), respectively. X and Y are calculated from Eq.4.1 and Eq. 4.2, respectively.

4.5.2 L- and M-cone thresholds along L-M and S axes

The calculated $\pm\delta[L-M]$ thresholds were plotted as a function of $[L-M]_{for-ada}$. The resulting graph is shown in Fig. 4.6. The region of the x-axis where $[L-M]_{for-ada} > 0$ refers to values of $[L-M]_{for-ada}$ where the L-M foreground excitations are greater than the L-M excitations of the background (see Equation 4.1), the opposite is true for the region $[L-M]_{for-ada} < 0$. Table. 4.1 lists the linear relationships for each of quadrant of Fig 4.6.

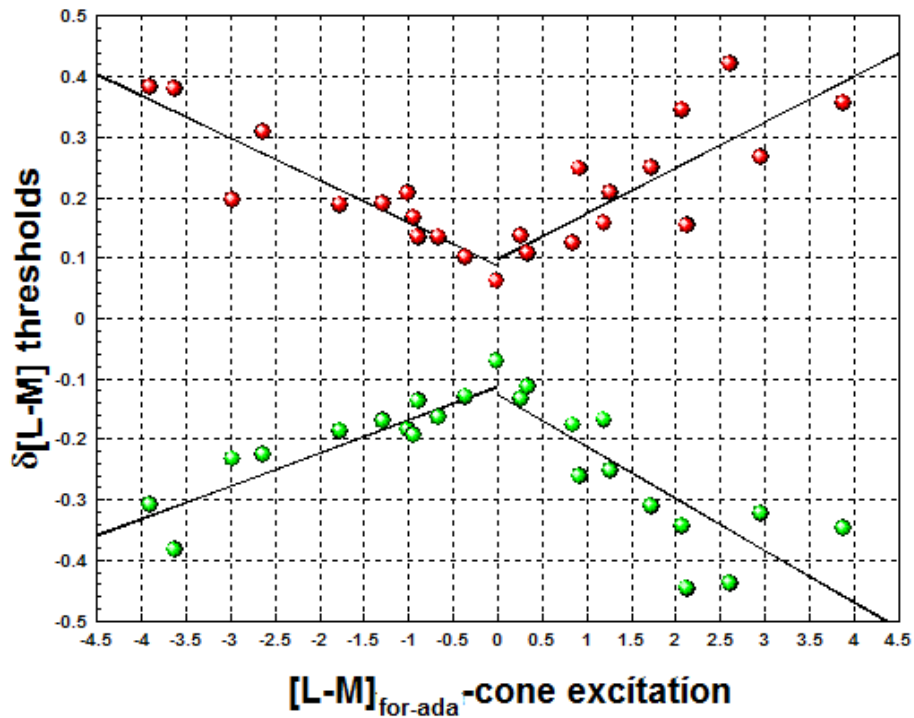


Fig. 4.6

The red and green circles represent the thresholds in the $+ [L-M]$ and $- [L-M]$ directions, respectively, for positive and negative $[L-M]_{\text{for-ada}}$ values. Note: the $\pm [L-M]$ axis is not exactly aligned with unique red and green (Philipona, 2006), but $+\delta [L-M]$ and $-\delta [L-M]$ can be considered to be detection thresholds in reddish and greenish colour directions, respectively.

Quadrant	$[L-M]_{\text{for-ada}}$	$\delta [L-M]$	$\delta [L-M] = a[L-M]_{\text{for-ada}} + k$	r^2
1	+ve	+ve	$\delta [L-M] = 0.076[L-M]_{\text{for-ada}} + 0.098$	0.64
2	+ve	-ve	$\delta [L-M] = -0.087[L-M]_{\text{for-ada}} - 0.126$	0.67
3	-ve	-ve	$\delta [L-M] = 0.054[L-M]_{\text{for-ada}} - 0.113$	0.81
4	-ve	+ve	$\delta [L-M] = -0.070[L-M]_{\text{for-ada}} + 0.088$	0.82

Table. 4.1

Parameters that represent the four $\pm [L-M]_{\text{for-ada}}$ vs. $\pm \delta [L-M]$ relationships (one per quadrant) shown in Fig 4.6, along with their linear correlation coefficients.

Considering the positive and negative sets of values of $\delta[L-M]$ separately, the mean values of the $\delta[L-M]$ axis intersections are at $([L-M]_{\text{for-ada}}, \delta[L-M]) = (0, 0.093)$ and $([L-M]_{\text{for-ada}}, \delta[L-M]) = (0, -0.12)$. These points correspond to the condition of the foreground and adapting fields producing equal $[L-M]$ -cone excitations, i.e., zero on the horizontal axis. Analysing the data from chapter 3 (for the same luminance level of 24 cd m^{-2}) where $[L-M]_{\text{for-ada}}$ was always zero, the corresponding intersection is found at $([L-M]_{\text{for-ada}}, +\delta[L-M]) = (0, 0.11)$. Within the experimental/observer error this implies that if $[L-M]_{\text{for-ada}}=0$, the $\pm\delta[L-M]$ threshold will be equal and oppositely signed around the $[L-M]_{\text{for-ada}}$ axis ($\sim\pm 0.1$ $[L-M]$ -cone excitations units); therefore the $\pm\delta[L-M]$ thresholds can be considered as independent of the adapting field S-cone excitation value. Fig. 4.6 also shows that the magnitude of the threshold is directly proportional to the difference between the foreground and adapting field excitation ($[L-M]_{\text{for-ada}}$), when $[L-M]_{\text{for-ada}}$ is positive or negative. The gradients of the four curves are similar to within one standard error, apart from the case when measuring $-\delta[L-M]$ thresholds for adapting field and foregrounds produced positive values of $[L-M]_{\text{for-ada}}$. These relationships are independent of the differences between S-cone excitations produced by the foreground and adapting fields. For the case where $\delta[L-M]$ and $[L-M]_{\text{for-ada}}$ are both negative, the results show there is a strong directly proportional relationship ($r^2 = 0.81$, $p < 0.05$), but the magnitude of the $-\delta[L-M]$ threshold is lower than the $+\delta[L-M]$ threshold produced by a $[L-M]_{\text{for-ada}}$ value of opposite sign but of the same magnitude. This implies that the observer was slightly more sensitive when making detections in the $-[L-M]$ direction when a negative $[L-M]$ -contrast exists between the foreground and adapting field i.e., $[L-M]$ decrements. Alternatively, as the deviation of the curve in quadrant 4 from the curves in the other three quadrants is small the difference could be accounted for

by some small observer error. If this assumption was true then detection thresholds along the [L-M]-cone cardinal axis direction could be considered symmetrical around the $[L-M]_{\text{for-ada}}$ and both the $+\delta[L-M]$ and $-\delta[L-M]$ axes. This would mean that for any given adapting background field and foreground combination ($[L-M]_{\text{for-ada}}$), the corresponding adapting field and foreground that produced the same sized but opposite signed difference $[L-M]_{\text{for-ada}}$, would result the thresholds being the same size for both $\pm\delta[L-M]$.

4.5.3 S-cones thresholds along the L-M and S axes

A similar method of analysis to the one described in the previous section was performed for the cardinal S-cone excitation direction. The thresholds $\pm\delta S$ were calculated and plotted as a function of $S_{\text{for-ada}}$, this is shown graphically in Fig. 4.7. Table. 4.2 list the linear relationships that exist in each of quadrant of Fig. 4.7. The $\pm\delta S$ excitation axis is not aligned with measured responses for unique blue and yellow (Philipona, 2006), but $+\delta S$ and $-\delta S$ can be considered to be detection thresholds in bluish and yellowish colour directions, respectively, as described in chapter 3.

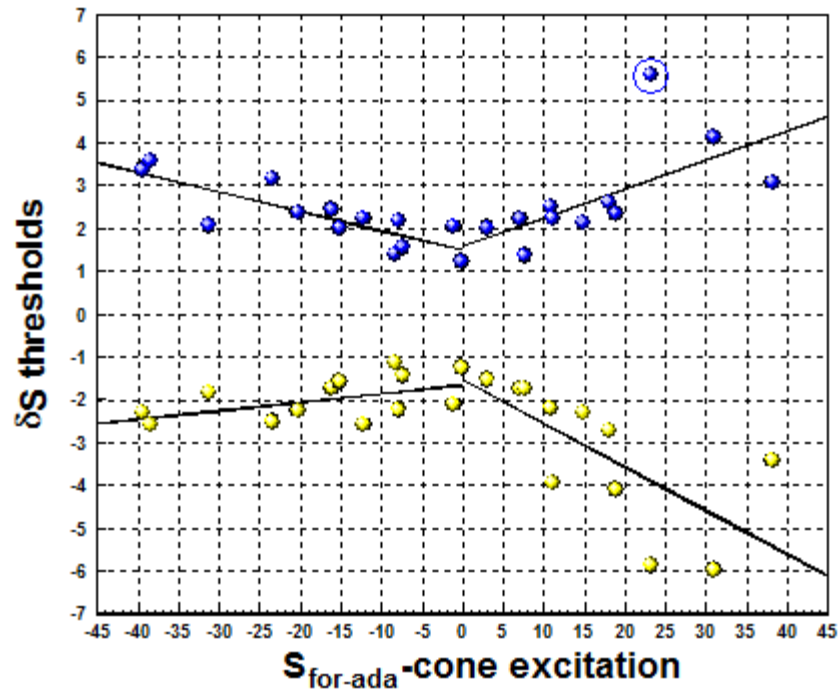


Fig. 4.7

The blue and yellow circles represent the thresholds in the +S and -S directions, respectively, for positive and negative $S_{for-ada}$ values.

Quadrant	$S_{for-ada}$	δS	$\delta S = a S_{for-ada} + k$	r^2
1	+ve	+ve	$\delta S = 0.067 S_{tar-ada} + 1.159$	0.38
2	+ve	-ve	$\delta S = -0.046 S_{tar-ada} + 1.486$	0.67
3	-ve	-ve	$\delta S = 0.020 S_{tar-ada} - 1.648$	0.27
4	-ve	+ve	$\delta S = -0.102 S_{tar-ada} - 1.549$	0.47

Table. 4.2

The linear relationships between δS and $S_{for-ada}$ are outlined for each quadrant of Fig. 4.7, all $ps < 0.05$.

Performing Grubbs' test for outliers (Pham, 2006) identified the point in quadrant 1 at (23.32, 5.56) as a significant outlier ($p < 0.01$), this point is highlighted with a blue ring in Fig. 4.7. This measured point was assumed to be due to a random

observer error and was removed from that data, resulting in a new adjusted relationship for quadrant 1; $\delta S = 0.0516 S_{\text{for-ada}} + 1.5995$, r^2 increased from 0.38 to 0.61 ($p < 0.05$). If the adjusted linear fit for quadrant 1 is compared to quadrant 2 the mean δS axis intersection ($S_{\text{for-ada}} = 0$) occurs at $(0, \delta S) = (0, 1.54)$ which falls within the mean standard errors for the two curves. As magnitudes of the gradients are effectively within ± 1 standard error of each other, the two curves can be considered symmetrical around the $+\delta S$ axis. This implies that any values of $S_{\text{for-ada}}$ equal in magnitude but of opposite signs will result in equal sized $+\delta S$ thresholds; these values are independent of $[L-M]_{\text{for-ada}}$. No outliers were identified in quadrants 3 and 4. The mean $-\delta S$ axis intersection ($S_{\text{for-ada}} = 0$) occurs at $(0, \delta S) = (0, -1.60)$ which falls within the mean standard errors for the two curves. The gradients in quadrants 3 and 4 differ significantly by a factor of ~ 5 . The data implies that the observer was less sensitive when making detections for positive values $S_{\text{for-ada}}$ than negative values of $S_{\text{for-ada}}$ of the same magnitude in the $-\delta S$ direction. Comparing quadrants 3 and 4 ($S_{\text{for-ada}} < 0$) the $\pm \delta S$ thresholds can differ by up to 30% over the range so $\pm \delta S$ values are not symmetrical around the negative $S_{\text{for-ada}}$ axis. This shows that when making detections in the $+S$ direction, a directly proportional relationship exists between $+\delta S$ and both $\pm S_{\text{for-ada}}$. The relationships that exist in quadrants 3 and 4 are not symmetrical around the $-\delta S$ axis.

4.5.4 Variation of thresholds with respect to ellipse orientation

An alternate method of analysing the results is presented. The previous section examined the thresholds in the $\pm[L-M]$ and $\pm S$ -cardinal cone excitation directions,

while this section is an analysis of the detection thresholds relative to the ellipse orientations. A general example is shown in Fig. 4.8 illustrating how the thresholds can be defined relative to the individual ellipse orientations. The thresholds that most closely align to the $+[L-M]$ and $-[L-M]$ directions are defined in Fig. 4.8 as $+\delta[L-M]_{\theta}$ and $-\delta[L-M]_{\theta}$, respectively. The thresholds that are most closely aligned with the $+S$ and $-S$ directions are defined in Fig. 4.8 as $+\delta S_{\theta}$ and $-\delta S_{\theta}$, respectively. The thresholds are calculated by extending the line from the foreground coordinate parallel to the relevant ellipse axis until it reaches the ellipse surface. The $\pm\delta[L-M]_{\theta}$ point in opposite directions (180°) relative to each other, as do $\pm S_{\theta}$. Defining the thresholds in this manner means that the thresholds are not necessarily aligned with the cardinal excitation axes, so the thresholds for a foreground with a given $[L-M]_{\text{for-ada}}$ may not have a constant S-cone excitation along the semi-major and -minor axes and vice versa. The difference in excitations between the adapting field and foreground combination are defined as before ($[L-M]_{\text{for-ada}}$ in Eq. 4.1 and $S_{\text{for-ada}}$ in Eq. 4.2).

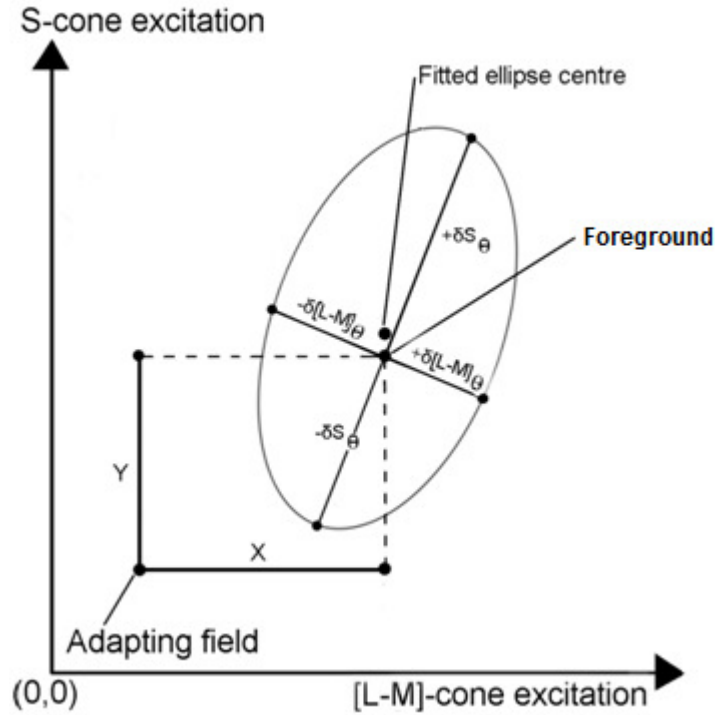


Fig. 4.8

An example of the coordinates of an adapting field and foreground combination is illustrated. The size and orientations of the $\pm\delta[L-M]_{\theta}$ and $\pm\delta S_{\theta}$ thresholds are illustrated with respect to the foreground chromaticity and ellipse orientation. The $\pm\delta[L-M]_{\theta}$ thresholds are defined as the distances from the foreground chromaticity to the ellipse surface (parallel to the ellipses semi-major axis), the $\pm\delta S_{\theta}$ thresholds as the distance from the foreground chromaticity to the ellipse surface (parallel to the ellipses semi-minor axis). X and Y represent the difference between the $[L-M]$ - and S -cone excitations of the adapting field and foreground ($[L-M]_{for-ada}$ and $S_{for-ada}$), respectively.

4.5.5 L- and M-cone thresholds along the ellipse exes

The individual L- and M-cone thresholds ($\pm\delta L_{\theta}$ and $\pm\delta M_{\theta}$) were analysed and were used to calculate the total $\pm\delta[L-M]_{\theta}$ threshold. $\pm\delta L_{\theta}$ and $\pm\delta M_{\theta}$ are defined by Eq. 4.3 and Eq. 4.4 and calculated along the ellipse axes that correspond most closely to the $\pm[L-M]$ -excitation axis.

$$\delta L_{\theta} = L_{\text{threshold}} - L_{\text{foreground}} \quad \text{Eq. 4.3}$$

$$\delta M_{\theta} = M_{\text{threshold}} - M_{\text{foreground}} \quad \text{Eq. 4.4}$$

The $+\delta L_{\theta}$ thresholds that are most closely aligned to the [L-M]-cone excitation axis in the positive x-direction with respect to the fitted ellipse (i.e., the detection thresholds that most strongly correspond to a reddish colour direction) are plotted as a function of the difference between the L-cone excitation of the foreground and adapting fields ($L_{\text{for-ada}}$), see Fig. 4.9(a). Fig. 4.9(b) shows the threshold excitations for the M-cones ($-\delta M_{\theta}$) in the same positive [L-M] direction. Fig. 4.10(a) and (b) show the $-\delta L_{\theta}$ and $+\delta M_{\theta}$ cone excitations at threshold for the direction that most strongly corresponds to the greenish $-[L-M]$ direction. These are the cone excitations, plotted in excitation space, orientated 180° relative to the $+[L-M]$ direction. All results indicate that as either the L- or M-cone excitation difference between the adapting field and foreground increases the magnitude of the individual cone thresholds increases linearly. Some of the linear relationships are noisy; for example Fig. 4.10(b) shows that the $+\delta M_{\theta}$ cone thresholds vs. $M_{\text{for-ada}}$ has $r^2 = 0.30$ ($p=0.54$). Only the relationship between $+\delta L_{\theta}$ vs. $L_{\text{for-ada}}$ (Fig. 4.9(a)), within its errors, can be considered symmetrical around the δL_{θ} axis; the L-cone excitations at threshold are of equal magnitude for equal sized (positive or negative) L-cone excitation differences between adapting field and foreground combinations.

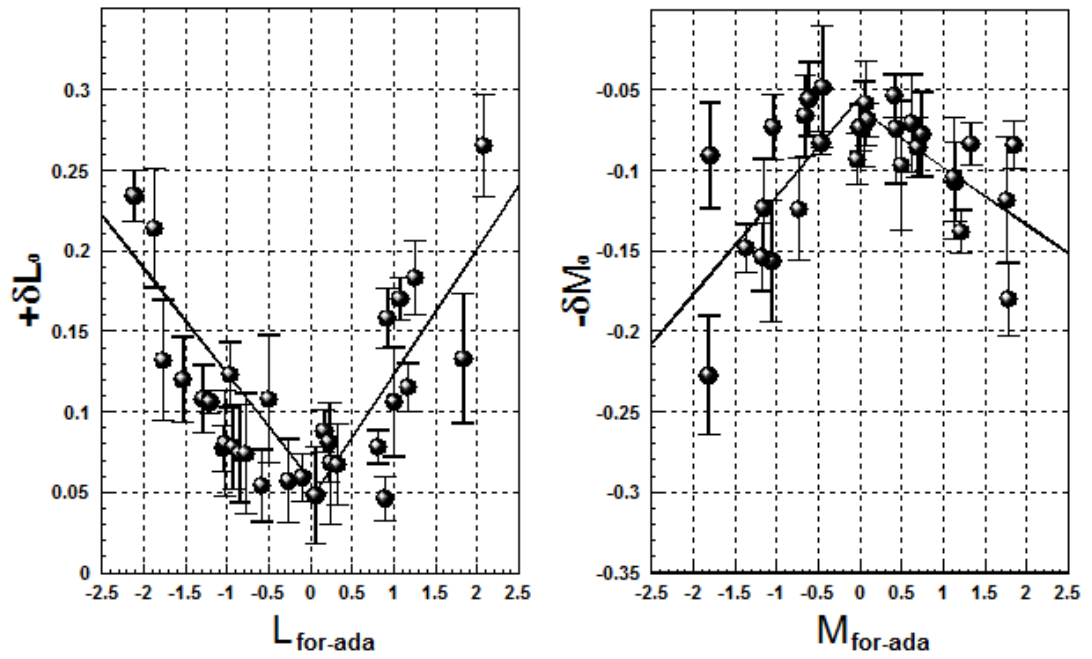


Fig. 4.9 (a) and (b)

The $+\delta L_\theta$ (a) and $-\delta M_\theta$ (b) thresholds are shown for detections that correspond to the reddish $+ [L-M]$ direction.

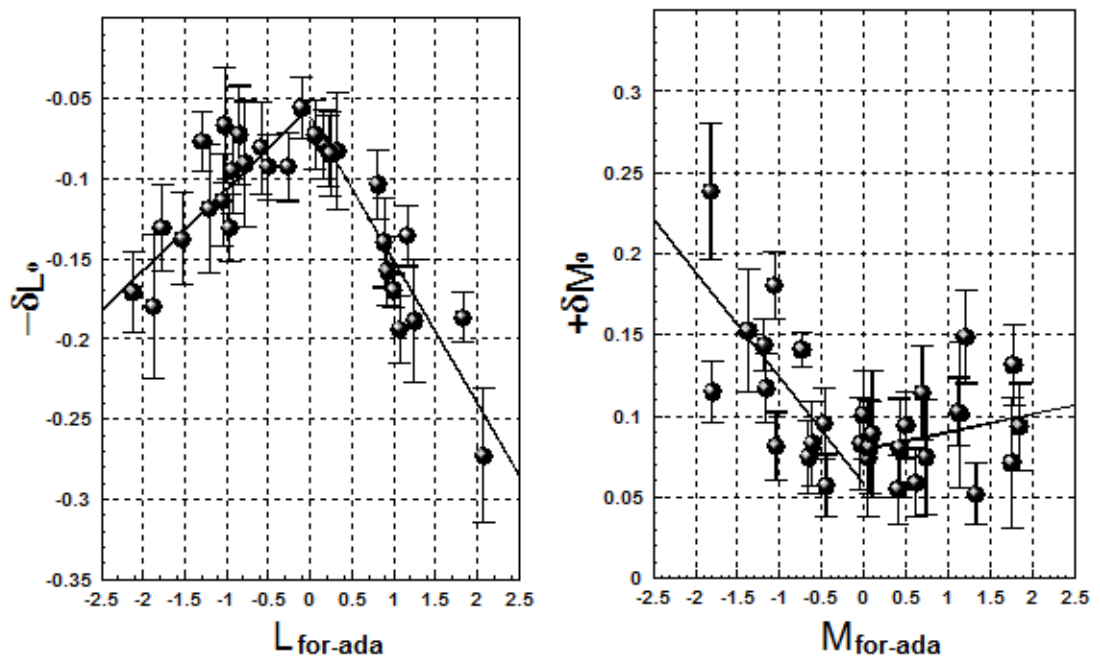


Fig. 4.10 (a) and (b)

The $-\delta L_\theta$ (a) and $+\delta M_\theta$ (b) thresholds are shown for detections that correspond largely to the greenish $- [L-M]$ direction.

Fig. 4.11(a) shows the result of combining the above cone thresholds into L-M pathway thresholds, to produce the relationship $-\delta[L-M]_{\theta}$ vs. $[L-M]_{\text{for-ada}}$; this indicates how the $-\delta[L-M]_{\theta}$ thresholds vary when making detections in a greenish colour direction relative to the foreground chromaticity. Fig. 4.11(b) combines the above results in a similar way; it shows how the $+\delta[L-M]_{\theta}$ vs. $[L-M]_{\text{for-ada}}$ -excitations vary for detections made in a reddish colour direction relative to the foreground chromaticity. Comparing the variation of $\pm\delta[L-M]_{\theta}$ thresholds for $[L-M]_{\text{for-ada}} > 0$ and $[L-M]_{\text{for-ada}} < 0$ for the greenish direction, it is found that the $-\delta[L-M]_{\theta}$ thresholds are not equal in magnitude for a given $\pm[L-M]_{\text{for-ada}}$ value. Within the measured standard errors, the magnitude of $+\delta[L-M]_{\theta}$ thresholds are equal in the reddish direction for given values of $\pm[L-M]_{\text{for-ada}}$, i.e., Fig. 4.11(b) can be considered symmetrical around the $+\delta[L-M]_{\theta}$ axis.

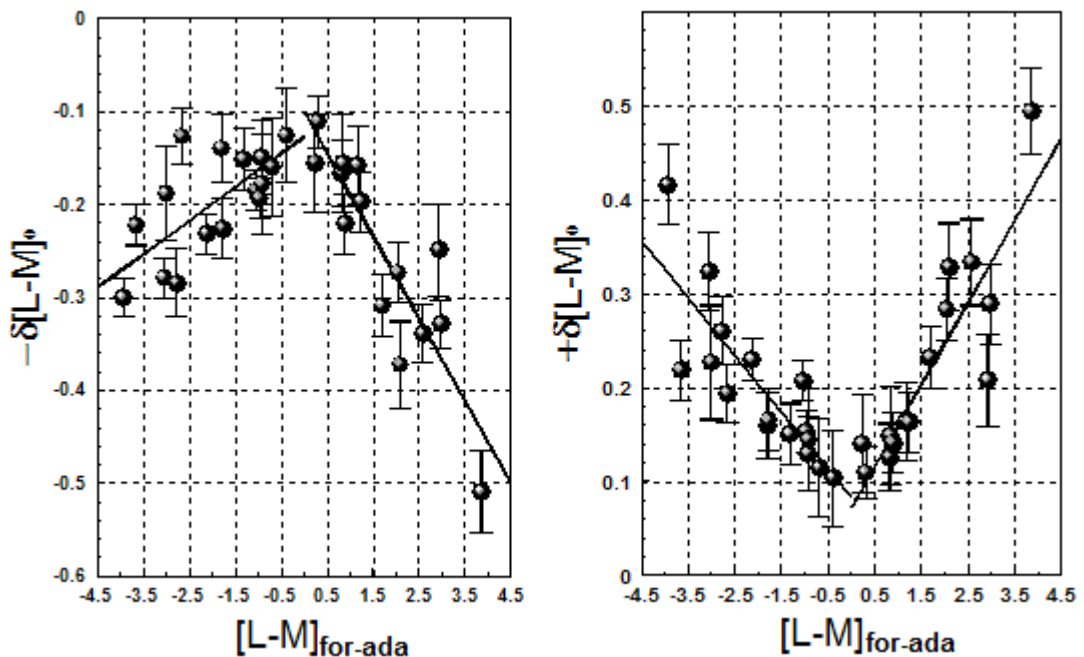


Fig 4.11(a) and (b)

The $-\delta[L-M]_{\theta}$ (a) and $+\delta[L-M]_{\theta}$ (b) thresholds plotted as a function of difference between the adapting field (the background) and the foreground, i.e., $[L-M]_{\text{for-ada}}$.

4.5.6 S-cone thresholds along the ellipse axes

The $\pm\delta S_\theta$ thresholds were calculated and plotted (Fig 4.12). Table 4.3 shows the linear relationships that exist within each quadrant of Fig. 4.12.

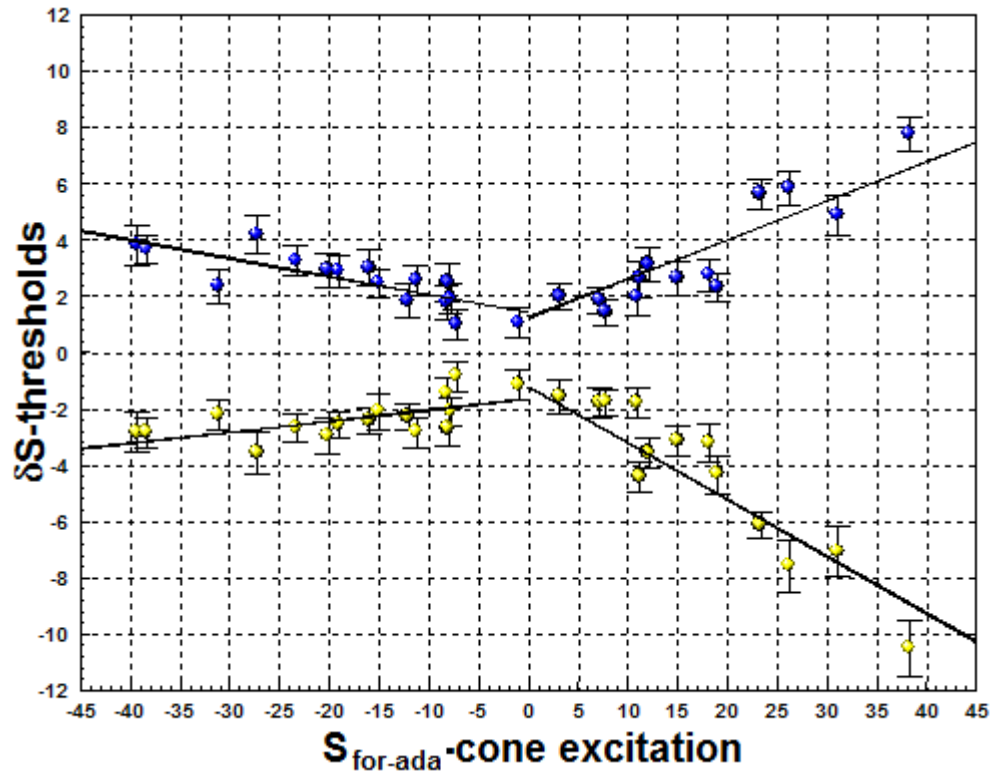


Fig. 4.12

Thresholds for the $\pm\delta S$ directions as a function of difference between foreground and background S-excitation.

Quadrant	$S_{\text{for-ada}}$	δS_θ	$\delta S_\theta = a S_{\text{for-ada}} + k$	r^2
1	+ve	+ve	$\delta S = 0.1725 S_{\text{for-ada}} + 0.4832$	0.82
2	-ve	+ve	$\delta S = -0.0651 S_{\text{for-ada}} + 1.4162$	0.56
3	-ve	-ve	$\delta S = 0.0387 S_{\text{for-ada}} - 1.6551$	0.39
4	+ve	-ve	$\delta S = -0.202 S_{\text{for-ada}} - 1.1902$	0.9

Table. 4.3

The linear relationships between δS_θ and $S_{\text{for-ada}}$ are outlined for each quadrant of Fig. 4.12, all $ps < 0.05$

The δS_θ axis intercept ($S_{\text{for-ada}}=0$) for the two detection curves in the $+\delta S_\theta$ direction are at $(0, \delta S_\theta) = (0, 0.48)$ and $(0, \delta S_\theta) = (0, 1.42)$, for positive and negative values of $S_{\text{for-ada}}$, respectively. These values differ by more than one standard error ($SE \sim 0.58$). This could imply observer error or it could be accounted for by a small deviation from the linear relationships when $S_{\text{for-ada}}$ tends to zero. The large difference in gradient magnitudes clearly indicates that the two curves are not symmetrical around the $+\delta S_\theta$ axis. The two curves representing the thresholds in the $-\delta S_\theta$ direction intercept the δS_θ axis at $(0, \delta S_\theta) = (0, -1.19)$ and $(0, \delta S_\theta) = (0, -1.66)$, for positive and negative values of $S_{\text{for-ada}}$ respectively. These values are within the value of one mean standard error for the two curves ($SE \sim 0.61$). These intercepts are consistent with earlier finding when $S_{\text{for-ada}}$ is zero (see chapter 3). The large difference in gradient magnitudes clearly indicates that the two curves are not symmetrical around the $-\delta S_\theta$ axis. However, there is an agreement in the gradient for $\pm\delta S_\theta$ when $S_{\text{for-ada}} < 0$, indicating the yellowish and bluish thresholds will have the same size for a given adapting field and foreground that produce a negative $S_{\text{for-ada}}$. For $S_{\text{for-ada}} > 0$ combinations of the same magnitude, the corresponding $\pm\delta S_\theta$ thresholds will be larger indicating the observer was more sensitive at making detections along the $\pm\delta S_\theta$ ellipse axis when a negative S-cone contrast existed between the foreground and background ($S_{\text{for-ada}} < 0$).

4.5.7 Distribution of ellipse orientations

The previous sections have outlined the influence of the background adapting field and foreground cone excitation differences on threshold sizes; one major problem arises with this analysis as the thresholds of interest ($\pm\delta[L-M]_\theta$ and $\pm\delta S_\theta$) are not

necessarily all aligned at a constant orientation relative to the [L-M]- or S-cone excitation cardinal axes. Therefore knowing how the thresholds vary for an adapting field and foreground chromaticity combination is of little practical use if only the magnitude of the threshold can be estimated and not the orientation in excitation space relative to the foreground chromaticity. The orientations were therefore also analysed. The ellipse orientations are defined as the angle between their semi-major axis and the +[L-M]-cone excitation axis. The results of measuring detection ellipses using a foreground and adapting field of the same chromaticity are described in chapter 3; these ellipses in cone excitation space have their semi-major axes aligned parallel to the S-cone excitation axis. When the background chromaticity is not equal to the foreground the ellipse orientation can deviate from this S-cone axis parallel alignment, as shown previously in Fig. 4.4(a), (b) and (c). The measured ellipses were found to shift and orientate themselves such that the semi-major axes point in the direction towards, or at least closer to, the adaptation chromaticity coordinate. This effect has also been observed by Kraukopf (1992). The measured ellipse orientations were analysed in terms of the angle they subtend relative to the +[L-M]-cone excitation axis (θ_{ellipse}) and the angle between the adaptation point (background) and foreground chromaticity coordinates ($\theta_{\text{ada-for}}$). Modulus values of the angle were used to keep the range $0 \leq \theta_{\text{ada-for}} \leq 180^\circ$ (Fig. 4.13). It is shown later in this chapter that the angles are symmetrical around the [L-M] axis - justifying this modulus transformation. The angle the foreground makes with the adapting field, in cone excitation space, is given by Eq. 4.5. It is a function of both the difference between the S-cone excitation signal (ΔS) of the foreground and the background adapting field (Eq. 4.6) and the difference between the [L-M]-cone excitation signals ($\Delta[L-M]$) of the foreground and the background adapting (Eq. 4.7).

$$\theta_{\text{ada-for}} (\Delta[L-M], \Delta S) = | \tan^{-1}(\Delta S / \Delta[L-M]) | \quad \text{Eq. 4.5}$$

$$\Delta S = S_{\text{for}} - S_{\text{ada}} \quad \text{Eq. 4.6}$$

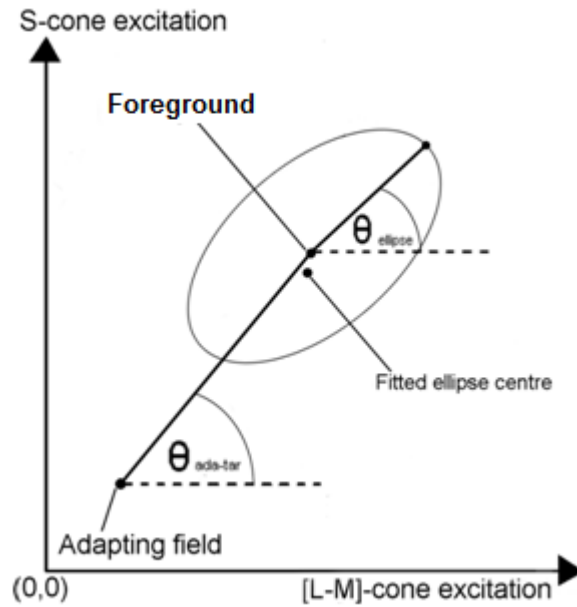


Fig. 4.13

The ellipse orientation is given by θ_{ellipse} and the angle between the adaptation point and foreground chromaticity coordinates is given by $\theta_{\text{ada-for}}$.

A plot of θ_{ellipse} vs. $\theta_{\text{ada-for}}$ is shown in Fig. 4.14. The linear relationship that exists between θ_{ellipse} and $\theta_{\text{ada-for}}$ ($r^2=0.92$, $p<0.01$) is described by Eq. 4.7.

$$\theta_{\text{ellipse}} = 0.44 \theta_{\text{ada-for}} + 50.20 \quad \text{Eq 4.7}$$

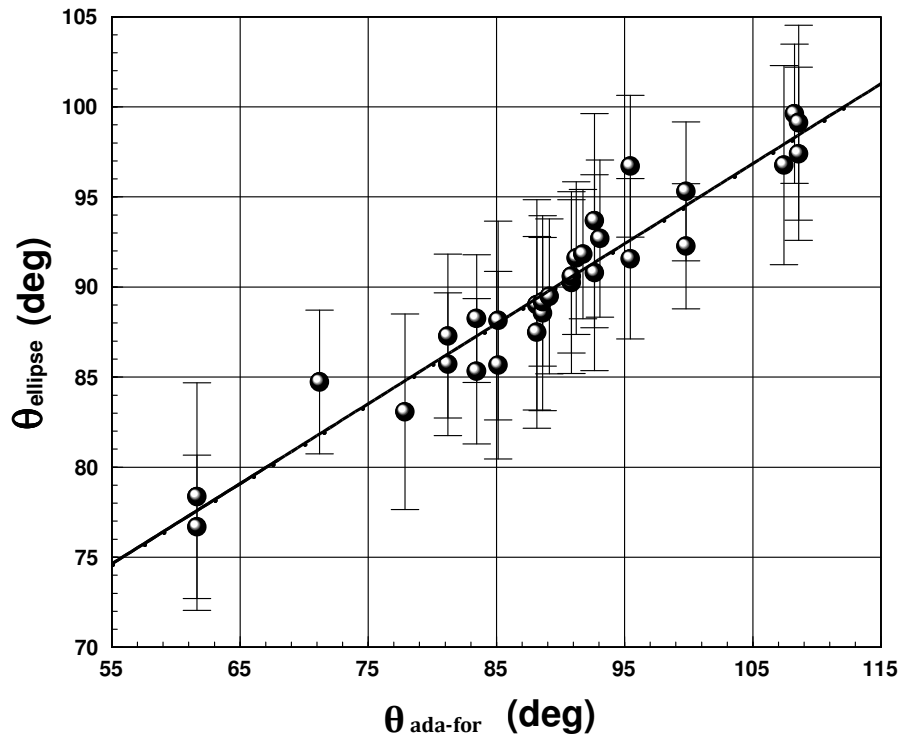


Fig. 4.14

The relationship between the measured ellipse angle (θ_{ellipse}) and the angle between the foreground and adapting field angle ($\theta_{\text{ada-for}}$).

Eq. 4.7 passes through the point $(\theta_{\text{ada-for}}, \theta_{\text{ellipse}}) = (90.00^\circ, 89.91^\circ)$; if the angle between the coordinates of the background adapting field and the foreground is $\pm 90^\circ$ then the ellipse will be aligned with its semi-major axis parallel to the S-cone excitation axis. This is consistent with earlier results for adapting field and foreground combinations that produce equal [L-M]-cone excitation values. The ellipses are spread, in cone excitation space, over a range ~ 6 times wider in the S-cone direction than the [L-M]-cone direction; this has the side effect that the angles between the foreground and adapting field for this dataset are centred around 90° within the restricted range $61^\circ \leq \theta_{\text{ada-for}} \leq 109^\circ$. It is unlikely that this $\theta_{\text{ada-for}}$ vs. θ_{ellipse} linear relationship remains valid for higher and lower foreground to adapting field angles outside this range $61^\circ \leq \theta_{\text{ada-for}} \leq 109^\circ$, as it implies that when

$\theta_{\text{ada-for}}=0$ the ellipses semi-major axes would subtend an angle of $\theta_{\text{ellipse}} \sim 50^\circ$. In order to verify this, an additional set of ellipses were measured for combinations of foregrounds and adapting background field chromaticities that subtended the 0, 30, 150 and 180° angles. Fig. 4.15 shows this extended dataset and Eq. 4.8 shows the fitted sine relationship that exists between $\theta_{\text{ada-for}}$ and θ_{ellipse} .

$$\theta_{\text{ellipse}} = 18.60 \sin(1.928 \theta_{\text{ada-for}}) + \theta_{\text{ada-for}} \quad \text{Eq. 4.8}$$

This fitted sine function passes through the points $(\theta_{\text{ada-for}}, \theta_{\text{ellipse}}) = (0.00^\circ, 0.00^\circ)$ and $(\theta_{\text{ada-for}}, \theta_{\text{ellipse}}) = (180^\circ, 178.68^\circ)$, the mean measured ellipse angles at these points are $(\theta_{\text{ada-for}}, \theta_{\text{ellipse}+\text{Err}}) = (0.00^\circ, 2.97^\circ \pm 6.08^\circ)$ and $(\theta_{\text{ada-for}}, \theta_{\text{ellipse}+\text{Err}}) = (180^\circ, 178.68^\circ \pm 5.45^\circ)$, respectively. Hence to within all ellipse fitting errors (Err) the fitted sine relationship is in agreement with the extended experimental dataset at these extreme values. This implies that when the S-cone excitation of the foreground and adapting field are equal, the ellipses will align their semi-major axes parallel to the [L-M]-cone excitation axis; consistent with earlier findings (Krauskopf and Gegenfurtner, 1992). The extended dataset shows that the outside of the $61^\circ \leq \theta_{\text{ada-for}} \leq 109^\circ$ range where most of the data is clustered, the linear relationship of Eq. 4.7 is not valid; however the sine and linear fitted functions are in agreement and differ by a maximum of only $\sim 1.5\%$ within the $61^\circ \leq \theta_{\text{ada-for}} \leq 109^\circ$ range.

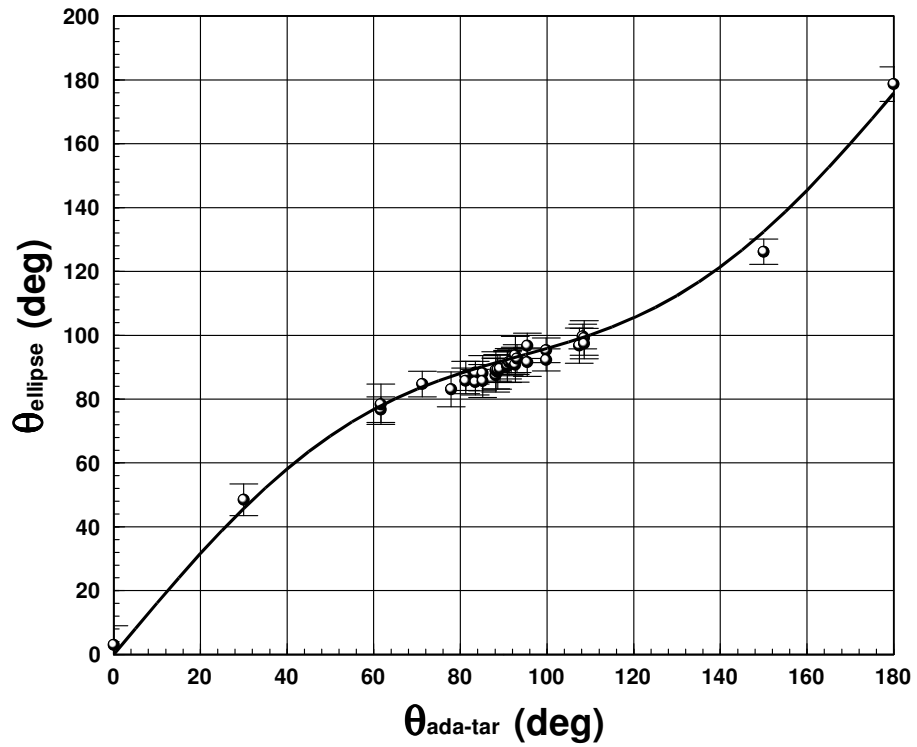


Fig. 4.15

The relationship between the foreground and adapting field angle ($\theta_{ada-for}$) vs. the measured ellipse angle for a foreground to adapting field angle range of $0 \leq \theta_{ada-for} \leq 180$.

If the adapting background produces an S-cone excitation lower than the S-cone excitation of the foreground then the angle between the foreground and adapting field coordinates will be in the range $180 < \theta_{ada-for} < 360^\circ$. The ellipse angle can still be determined in this range by transforming Eq. 4.8 into a format that is valid for the range $0 \leq \theta_{ada-for} \leq 360^\circ$, see Eq. 4.9.

$$\theta_{ellipse} = 360 - (18.6 \sin(1.93 \theta_{ada-for}) + \theta_{ada-for}) \quad \text{Eq. 4.9}$$

The different combinations of adapting field and foreground chromaticities tested had Euclidean separations that varied over the wide range $2 < \text{“excitation space separation”} < 40$ (cone excitation units) with 18.1 ± 10.4 (mean \pm SD). This indicates that it is not necessary to take into account the magnitude of the separation of the

adapting field and foreground; the angle between them is sufficient to estimate the resulting ellipse orientation. This suggests that the ellipse orientation is determined by the ratio of the cone excitations between the adapting field and foreground and not the absolute magnitude of the difference between them.

4.5.8 Fitting errors

The measured and the fitted linear relationships were compared for the [L-M]- and S-cone thresholds along the cardinal axes and ellipse axes. The results are shown in Table. 4.4. All values are the mean percentage errors and their corresponding standard deviations (mean \pm SD) for the comparison of the fitted linear relationships to the measured thresholds. The percentage errors were calculated for both the $\pm\delta$ [L-M] and $\pm\delta$ S thresholds along the cardinal axes and the $\pm\delta$ [L-M] $_{\theta}$ and $\pm\delta$ S $_{\theta}$ thresholds relative to the ellipse axes.

	Along ellipse axes			Along cardinal axes	
	[L-M] _{for-ada} > 0	[L-M] _{for-ada} < 0		[L-M] _{for-ada} > 0	[L-M] _{for-ada} < 0
$+\delta$ [L-M] $_{\theta}$	16.2 \pm 15.2	14.8 \pm 10.7	$+\delta$ [L-M]	27.0 \pm 20.3	14.1 \pm 14.0
$-\delta$ [L-M] $_{\theta}$	16.3 \pm 11.3	17.8 \pm 16.3	$-\delta$ [L-M]	24.8 \pm 18.1	11.4 \pm 5.7
	S _{tar-ada} > 0	S _{tar-ada} < 0		S _{tar-ada} > 0	S _{tar-ada} < 0
$+\delta$ S $_{\theta}$	23.1 \pm 16.2	21.6 \pm 17.9	$+\delta$ S	15.0 \pm 13.6	16.6 \pm 12.2
$-\delta$ S $_{\theta}$	20.3 \pm 22.5	17.8 \pm 13.2	$-\delta$ S	28.8 \pm 11.5	21.0 \pm 13.1

Table. 4.4

A comparison of fitting errors (%) for L-M and S detection in different directions relative to the fitted ellipses.

Table. 4.4 shows that the $\pm\delta$ [L-M] $_{\theta}$ and $\pm\delta$ [L-M] thresholds can all be estimated with good accuracy, either to within or slightly above ± 1 SD, apart from the $-\delta$ [L-M] when [L-M]_{for-ada} < 0 which has a SD of less than half the mean SD. The percentage

error between the predicted ellipse orientation and the orientations based on the fitted ellipses is $5.9\% \pm 3.8\%$.

In order to assess the accuracy of these fitted relationships in predicting new ellipse parameters, an additional independent set of five detection ellipses were measured for observer BJ. These were measured using different sets of adapting field and foreground combinations not previously used. All 5 of these fitted ellipses had their parameters predicted to within, or approximately equal to, the errors as estimated by the fits of the data presented in this chapter, using both the “along cardinal axis” threshold data and also the “along ellipse axes” threshold data (coupled with the orientation data).

4.6 Discussion and conclusion

The results presented here are consistent with Krauskopf *et al.* (1992) who investigated the variation of threshold sizes when discriminations were made in regions of colour space that were distant to the adapting background chromaticity. Both studies found that the thresholds are lowest when the adaptation point and foreground (which they refer to as “test vectors”) are of similar or equal chromaticity i.e., observers become more sensitive as they make detections near the adaptation point. Krauskopf’s analysis is presented mainly in terms of thresholds along the cardinal axis directions; the analysis of the data presented here has been extended to examine the threshold variations relative to the individual ellipse orientations and along the ellipse axes. The results presented here are also consistent with Hita *et al.* (1989) in finding that adapting to a reddish chromaticity results in the largest increase in thresholds for detections made at

different locations. In general the thresholds along the ellipse axes are higher than the corresponding thresholds along the cardinal axes; this is expected as the thresholds relative to the ellipse orientation are approximately equal to the ellipse semi-major and -minor axes (neglecting the slight difference that can occur between the foreground and fitted ellipse's centre coordinates). The ellipse axes most closely align with the cardinal axes when either $S_{\text{for-ada}}$ or $[L-M]_{\text{for-ada}}$ is zero. When either $S_{\text{for-ada}}$ or $[L-M]_{\text{for-ada}}$ is zero, both methods of analysis are equivalent and give equal results. When considering the thresholds along the ellipse axes, linear relationships need to be supplemented with a method of determining their direction in colour space; this relationship takes the form of a $\sin(x)+x$ curve. Krauskopf *et al.* (1992) found that along the cardinal L-M axis the measured thresholds depended only on the difference between the background and the adaptation point and it was noted this was analogous to brightness discrimination (Craik, 1938). Krauskopf showed the test vector magnitudes along one cardinal direction had no influence on the thresholds in another cardinal direction. The results presented here are consistent with this, for example $\pm\delta[L-M]$ vs. $S_{\text{for-ada}}$ is constant and insignificant compared to $\pm\delta S$ vs. $S_{\text{for-ada}}$. This observation supports the hypothesis of independent detection mechanisms acting along the cardinal $[L-M]$ and S-cone axes. It is important to note that psychophysical studies have demonstrated that although the coding of elementary visual features within each chromatic pathway seem to be independent at perceptual threshold, they can be subject to highly non-linear interactions (inhibitory or facilitatory) at suprathreshold stimulation (Kulikowski, 2003).

Chapter 5

Effect of chromatic adaptation as a function of retinal location

5.1 Introduction

During the previous sets of experiments outlined in chapters 3 and 4, observers attempted to detect a chromatic stimulus as it moved diagonally across a $\sim 2.9^\circ \times 2.9^\circ$ region of the $3.3^\circ \times 3.3^\circ$ area of luminance contrast noise (the foreground area of the CAD test). During this task, observers always fixated on the centre of this foreground region (there is a small solid dark dot in the centre of luminance noise that acts as a fixation guide). Observers therefore only ever make colour detections based on a foveally projected stimulus. Throughout each CAD run (chapter 4) the chromaticity of the foreground region alternated between the foreground chromaticity and the background adapting field chromaticity during the 3000 ms delay periods between each trial each presentation; this maintained chromatic adaptation to the background chromaticity, see chapter 4 control experiment. The rest of the adapting field (the full $22^\circ \times 24^\circ$ of the CRT display) surrounding the foreground was kept constant throughout each testing block. Therefore, if the observers fixate throughout each testing block, only the central $3.3^\circ \times 3.3^\circ$ region of the retina where the detections are made is ever exposed to the foreground chromaticity. This chapter presents the methodology and results of an experiment performed to investigate the influence that peripheral chromatically adapted cones have on chromatic detection thresholds being

measured using central chromatically adapted cones, when adapted to equal or difference chromaticities.

5.2 Method

The experiment was performed in three sections to systematically investigate the effect of chromatically adapting different regions of the retina to different chromaticities;

- A control experiment was performed
- An experiment using a dark border surrounding the foreground along with a background of equal chromaticity was performed, and
- An experiment using a dark border along with a background of a different chromaticity to the foreground was performed.

The CAD test was used to measure chromatic detection thresholds (chapter 2). A variable sized dark border was introduced around the $3.3^\circ \times 3.3^\circ$ foreground region; the purpose of this border was to create a retinal area that was not stimulated by light coming from the region of the CRT screen immediately surrounding the CAD test foreground area. The border comprised a hollow square; its thickness subtended a visual angle of X° in the horizontal and vertical directions around the foreground area (see Fig. 5.1).

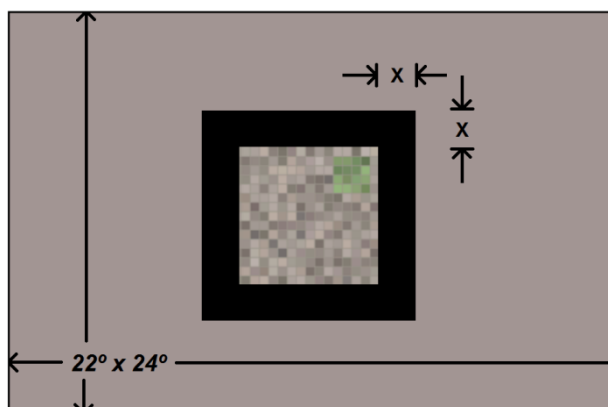


Fig. 5.1
The full display (22° x 24°) is shown along with the central 3.3° x 3.3° patch of luminance noise where the moving chromatic stimulus is detected (not to scale). X indicates the thickness of the dark surround.

A series of borders, of varying sizes (X°), were constructed from light insulating black felt and stuck around the foreground area directly onto the display; this ensured no light was emitted from the border region as CRT displays are capable of emitting some light even when “black” is required (Brainard, 2002). The border thicknesses subtended a variety of angles ($X=1, 2, 3, 6, 8, 12^\circ$) and only allowed the adapting background field to be visible beyond them towards the retina’s periphery. Detection thresholds were measured for each border thickness (including zero, i.e., no border ($X=0$) and no background ($X=\infty$), i.e., all of the background was covered by the dark border) with equal and unequal background and foreground chromaticity combinations. When the foreground and backgrounds were equal, the 3000 ms delay between trials was removed as it was not required; this also had the advantage of reducing data acquisition times.

5.3 Observers

Two observers were chosen to take part in this experiment the author BJ and subject MRR, both of whom are experienced psychophysical observers. This was important as possessing the ability to maintain good fixation was required in order to ensure different areas of the retina were kept in different chromatically adapted states (or kept inactive).

5.4 No border control experiment

Chromatic detection thresholds were measured along one colour direction using two different foreground chromaticity combinations, a reddish foreground at CIE xy: (0.3977, 0.3283) and a bluish foreground at CIE xy: (0.2600, 0.2400). A white adapting background field at CIE xy: (0.305, 0.323) was used in combination with both foregrounds. Fig. 5.2 shows, in CIE xy space, the coordinates of the adapting field (white circle), the two foreground chromaticities (blue and red crosses) and the position of the measured thresholds (blue and red circles) for BJ with no border present. The same 3000 ms delay was included between presentations, as used in chapter 4, to ensure the central foveal cones remained adapted to the whitish background throughout the experiment. The two thresholds were measured in the colour direction from the foreground chromaticity to the white point.

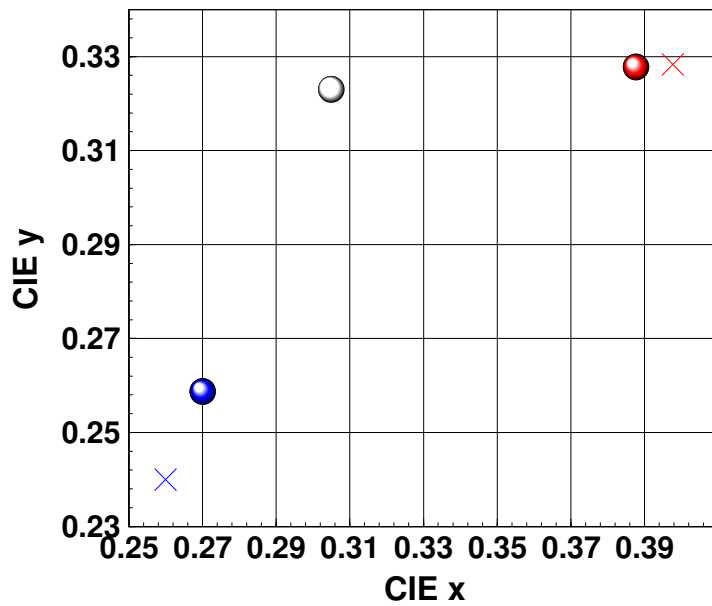


Fig 5.2

The white disc plots the chromaticity coordinates of the white adapting background field, the red and blue crosses are the chromaticity coordinates of the red and blue foreground fields and the red and blue discs are the detection thresholds obtained with no border present.

Fig 5.2 shows the thresholds to be consistent with the results of chapter 4; thresholds measured for unequal background and foreground chromaticities indicate when measured at a rate of one threshold per test (rather than 16 as measured in the experiments described in chapters 3 and 4) will result in a threshold of equal magnitude being produced, i.e., thresholds in a given direction can be measured separately without the need to use interleaved staircases in different directions in the same testing block, i.e., each measured threshold is independent. Fig 5.2 shows thresholds for observer BJ only, however observer MRR produced similar thresholds.

5.5 Results

The results are presented in two sections; firstly for the condition when the adapting background and foreground chromaticities are equal and secondly for the condition when they are unequal.

5.5.1 Equal adapting field and foreground chromaticity results

The effect of varying the border thickness on detection thresholds when the foreground and visible background are of equal chromaticity are shown in Fig. 5.3(a) and (b); these are the measured thresholds (the mean is indicated by the horizontal dashed lines) for detections made for the reddish foreground and background combination. The results indicate, for both observers, that the threshold level remains constant and independent of border thickness, over the whole range from zero (no border) through each thickness used to infinity (no visible background). Both observers' thresholds, in these directions are consistent with their fitted threshold ellipses as measured in chapter 3.

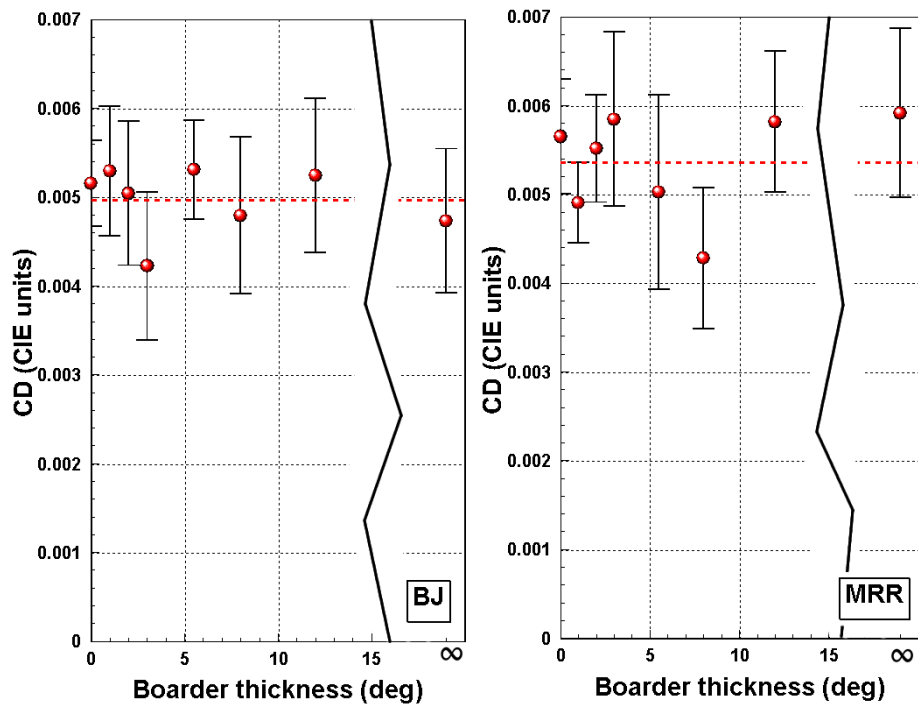


Fig. 5.3(a) and (b)
 Threshold sizes (CD) plotted as a function of border thickness for BJ and MRR. The thresholds were measured using reddish adapting background field and foreground.

5.5.2 Different adapting field and foreground chromaticity results

Fig. 5.4(a), (b), (c) and (d) illustrate how the measured thresholds, expressed as chromatic displacements (CD) (i.e., Euclidian distances) in the CIE xy colour space, vary as a function of border thickness for the two observers. Fig. 5.4(a) and (b) are the measured CDs for the reddish foreground, Fig. 5.4(c) and (d) show the CDs for the bluish foreground; both using the white at CIE xy: (0.305, 0.323) as the adapting chromaticity. The data indicates that with no border, a border of any thickness or a border of infinity will result in equal thresholds being measured; this was the case for both observers. Only 2/16 (BJ) and 3/16 (MRR) measured thresholds out of the total of the 16 measured are located further than one standard error from the mean threshold (shown as the dashed horizontal lines in

Fig. 5.4(a), (b), (c) and (d)). The mean measured CD for both observers are consistent in those colour directions with their fitted ellipse predictions for the same foreground and adapting field chromaticity combinations (also illustrated for BJ in Fig. 5.2). During the experiment for large border thicknesses, both observers reported an increase in the perceived luminance, i.e., brightness, of the foreground region; this is consistent with Williams (1998). For the largest border thickness, observer MRR remarked the foreground area was “painfully bright”.

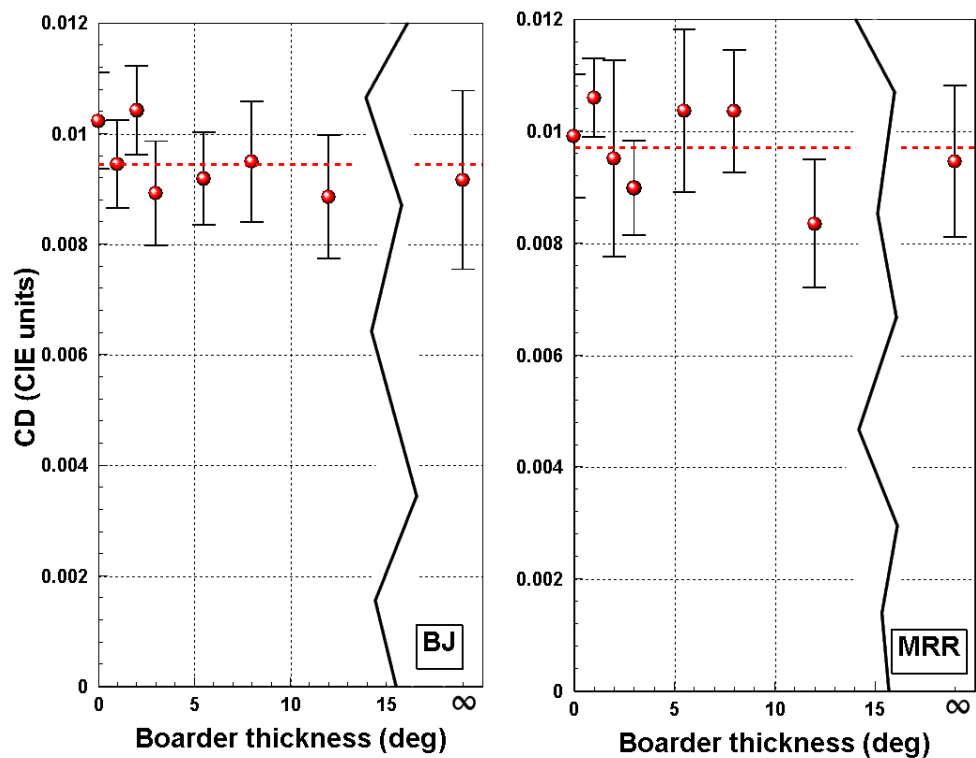
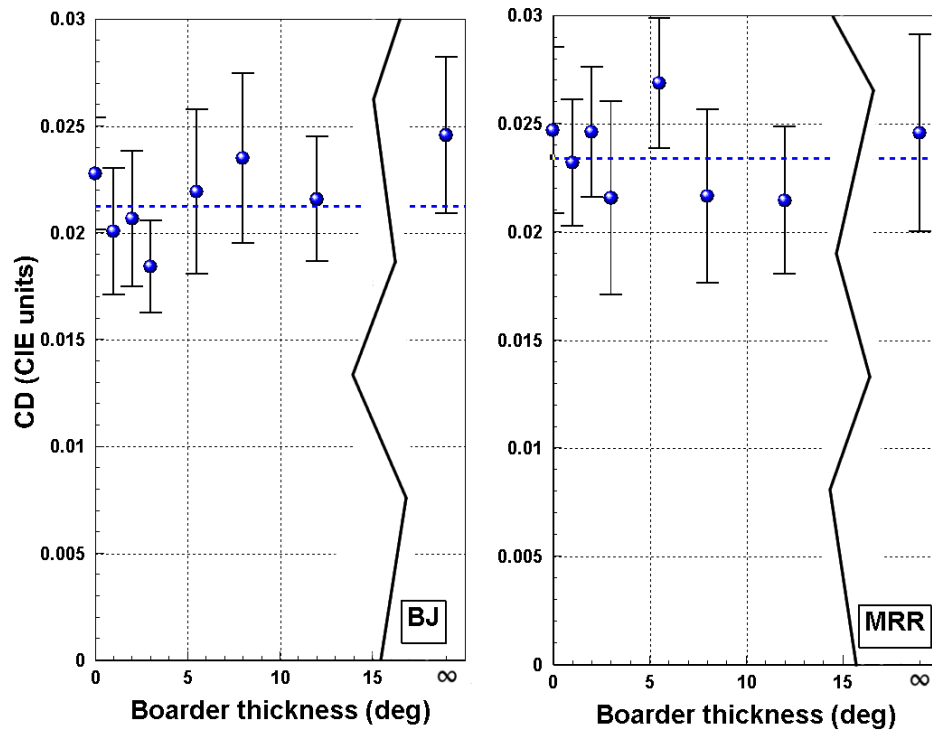


Fig. 5.4(a) and (b). Threshold sizes (CD) plotted as a function of boarder thickness for BJ and MRR. (a) and (b) are thresholds produced using a combination of white adapting field and red foreground.



5.4 (c) and (d)

Threshold sizes (CD) plotted as a function of boarder thickness for BJ and MRR. (c) and (d) are thresholds produced using a combination of a white adapting field and bluish foreground.

5.6 Discussion and conclusion

There are some well known phenomena that act across large regions of the retina, such as colour constancy (Land and McCann, 1971). Colour constancy is the process whereby the global appearance of hues across a scene or image remain unaltered with changes in either or both of the spectral power distribution or intensity of the scene's illumination. In order for colour constancy to be maintained, signals from across a large region of the scene and hence the retina (Leeuwen, 2004) need to be combined. In isolation, however, smaller regions of the scene will be subject to colour appearance changes, indicating long range interactions are involved. Further, Pöppel (1986) has shown that colour induction (the phenomena of perceiving colour without the corresponding retinally located

cones receiving any stimulating signals) is a retinal process which relies on integration over large regions, suggesting long range retinal interactions. However, the results presented here show threshold levels to be independent of the dark border thickness, implying that there cannot be any long-range interactions between cones in the adapted foveal and peripheral retina when the adaptation states are either equal or unequal in those regions.

Only the adapted state of the central $\sim 3.3^\circ \times 3.3^\circ$ region where the detections are made is of importance. This implies that the use of a $22^\circ \times 24^\circ$ adapting background field was not required to produce the measured threshold ellipse sizes shown in chapters 3 and 4; provided the observers have their foveal cones chromatically adapted and make detections using those foveally adapted cones then the adapted state or absence of cone signal (regions covered by the dark border) in the peripheral retina will not influence the detection sensitivity. This suggests no mechanism exists that communicates chromatically adapted states globally across the retina. This is possibly an advantage when viewing real world scenes composed of a variety of different illuminations (Graham *et al.*, 1997), as any peripherally adapted cones will not affect chromatic sensitivity in the fovea. Psychophysical testing using the full CRT display as a chromatic adapting field is, however, an advantage for practical reasons as it safeguards against any involuntary saccades that are made; the background adapting field will always be in view maintaining chromatic adaptation. This is advantageous when attempting to test inexperienced observers that may find it difficult not to make eye movements throughout each testing block.

Chapter 6

The variation of cone contrasts at threshold with macular pigment optical density

6.1 Introduction

The amount of macular pigment present on the retina, i.e., the macular pigment optical density (MPOD), has been shown to vary in both peak value (MP_{peak}) (Kilbride, 1988) and spatial distribution (Hammond Jr *et al.*, 1997) within the general population. These variations have been shown to be due to a combination of both genetic and dietary factors (Hammond Jr, 1995). The macular pigment filters the incoming light by absorbing some of the relatively high energy photons over the range ~390 to ~550 nm, peaking in the bluish region for a wavelength of 457 nm. An increase in MPOD will result in a higher proportion of bluish light being filtered (absorbed) and hence not reach the photoreceptors. The macular pigment absorption range spans the whole wavelength range the S-cones are sensitive to, but only partially overlaps the M-cone spectral sensitivity range and to an even lesser degree the L-cone spectral sensitivity range. This chapter presents an investigation examining the effect that differing MPODs in individuals ($n=15$) with normal colour vision has on their chromatic detection thresholds and specifically how it affects the individual L-, M- and S-cone contrasts as a function of colour direction. Simulations were performed varying the size and orientation in CIE xy colour space of a detection ellipse to assess the effect these two parameters

had on the cone contrast curves (see chapter 2); it is shown that some of the variation can be attributed to MPOD. The results reveal a relationship between the L-cone contrast curve gradient over the region of reddish chromaticities and the MPOD levels. This relationship can be used to estimate MPOD for individuals with ~10% error, based only on their chromatic detection ellipse.

6.2 Method

In order to investigate the effect MPOD levels have on chromatic detection thresholds, two tests were employed; the Colour Assessment and Diagnosis (CAD) test was used to measure subjects' colour detection threshold ellipse and the Macular Assessment Profile (MAP) test was used to measure MPOD profiles (see Chapter 2 for details). Fifteen subjects took part in the investigation, they had an age of 29.3 ± 7.4 years (mean \pm SD), all subjects had 6/6 vision or better and wore refractive correction when required. All subjects had normal colour vision as determined by the CAD test.

6.2.1 Colour Assessment and Diagnosis (CAD) test

A chromatic detection ellipse was measured for each of the 15 subjects using the CAD test (see chapter 2). The following test parameters were used: the foreground and background chromaticity were whitish and located at CIE xy: (0.305, 0.323) and the luminance of both was kept constant at 24 cd m⁻². Thresholds were measured along 16 equally spaced directions in colour space using 16 interleaved staircases. Two identical blocks of the CAD test were performed; this meant

ellipses could be fitted (Fitzgibbon *et al.*, 1999) to the mean data points from both trials lowering the overall fitting errors and also the two individual trials could be fitted separately giving an estimate of the error of the fitted ellipse orientation.

6.2.2 Macular Assessment Profile (MAP) test

The MAP test was employed to measure the macular pigment profile of each student. This test produced a macular pigment optical density profile as a function of visual angle (θ) where $0 \leq \theta \leq 7.8^\circ$ (zero corresponding to central vision). Two useful values relating to macular pigment levels were extracted for each subject from this optical density profile; the subject's peak macular pigment level (MP_{peak}) located foveally at $\theta=0^\circ$ and the average MPOD over the subject's central 2.8° field of view ($MP_{2.8^\circ}$). During each CAD trial the moving stimulus was displayed moving diagonally over a region of $\sim 2.9 \times 2.9^\circ$ within the foreground $3.3 \times 3.3^\circ$ region. This means the value of $MP_{2.8^\circ}$ accurately represents the average filtering effect of the macular pigment with respect to the central retinal region that the chromatic stimulus is being detected within.

6.3 Results

6.3.1 Range of test subject macular pigment levels

The peak macular pigment levels for the 15 subjects were found to be in the range $0.13 \leq MP_{\text{peak}} \leq 0.80$; these correspond to the macular pigment levels at zero eccentricity. The mean macular pigment levels over the central 2.8° were found to

be in the range $0.05 \leq MP_{2.8^\circ} \leq 0.45$. These data show a linear trend ($r^2 = 0.36$, $p=0.059$) for peak macular pigment levels (MP_{peak}) to increase with the mean macular pigment levels over the central 2.8° ($MP_{2.8^\circ}$) (see Fig. 6.1). This relationship is described by Eq. 6.1; the linear fitting of which was forced through point $(MP_{2.8^\circ}, MP_{peak})=(0, 0)$ as this tuple cannot be a combination of zero and non-zero values.

$$MP_{peak} = 1.7 MP_{2.8^\circ} \quad \text{Eq. 6.1}$$

Neelam (2005) measured macular pigment levels in subjects using both Raman Spectroscopy and Heterochromatic Flicker Photometry techniques and concluded that peak macular pigment values only approximately represent total macular pigment concentration. This is consistent with the data presented here as a highly significant relationship is not expected between $MP_{2.8^\circ}$ and MP_{peak} .

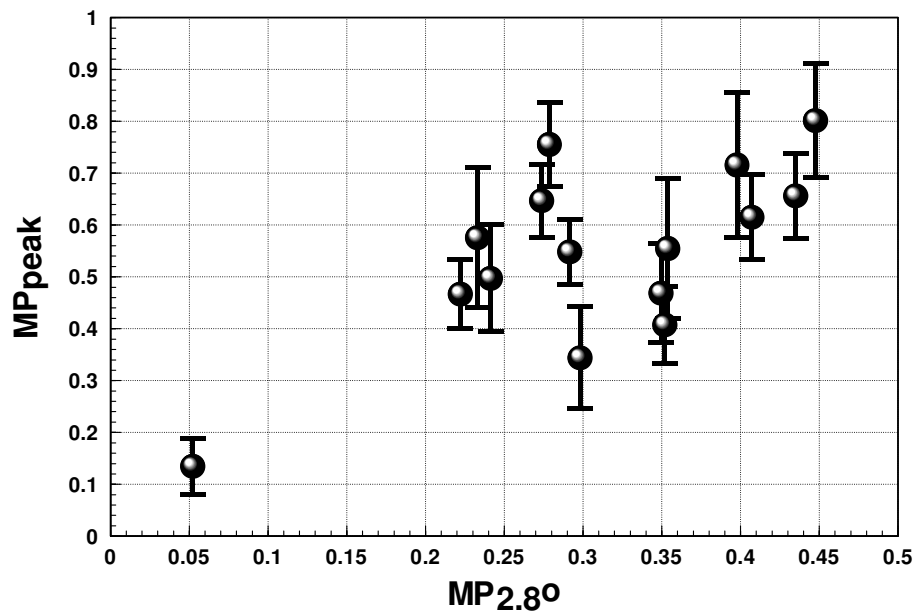


Fig. 6.1

The weak relationship between peak macular pigment levels vs. the average macular pigment levels over the 2.8° of central vision.

6.3.2 Ellipse orientation vs. macular pigment levels

The CAD test measured threshold ellipse orientations were compared to the MAP test results. The ellipse orientation ($\emptyset_{\text{ellipse}}$) was defined as the direction of the semi-major axes of the fitted ellipse relative to the positive CIE x axis. The mean orientation for the 15 subjects was found to be 62.2° . This orientation is consistent with the standard CAD observer ellipse (Barbur *et al.*, 2006) which has an orientation of $\sim 62^\circ$ (see chapter 2). The fitted ellipses were orientated within a $\sim 10^\circ$ range ($56.8^\circ \leq \emptyset_{\text{ellipse}} \leq 67.2^\circ$). Fig. 6.2 and 6.3 shows the relationship between the fitted ellipse orientation in CIE xy space vs. the peak (MP_{peak}) and central 2.8° ($\text{MP}_{2.8^\circ}$) levels of macular pigment, respectively. The error bars shown in Fig. 6.2 and 6.3 are the difference between the two fitted ellipses based on two estimates of CAD thresholds per observer; this value is typically $\sim 2.5^\circ$. The ellipse orientations vs. peak macular pigment levels (Fig. 6.2) essentially show only a linear trend ($p=0.054$) and are not considered further. The ellipse orientations show a linear relationship ($r^2 = 0.67$, $p < 0.05$) with the mean central 2.8° macular pigment levels ($\text{MP}_{2.8^\circ}$) as shown in Fig. 6.3. The relationship is described by Eq. 6.2; the fitting error cannot be significantly reduced by fitting a higher order polynomial curve to the data.

$$\emptyset_{\text{ellipse}} = -25.5 \text{MP}_{2.8^\circ} + 70.0 \quad \text{Eq. 6.2}$$

In Eq. 6.2 $\emptyset_{\text{ellipse}}$ is the ellipse orientation in CIE xy space and $\text{MP}_{2.8^\circ}$ is the mean central 2.8° macular pigment level; for the $n=15$ observers tested this spans the range $0.05 \leq \text{MP}_{2.8^\circ} \leq 0.45$.

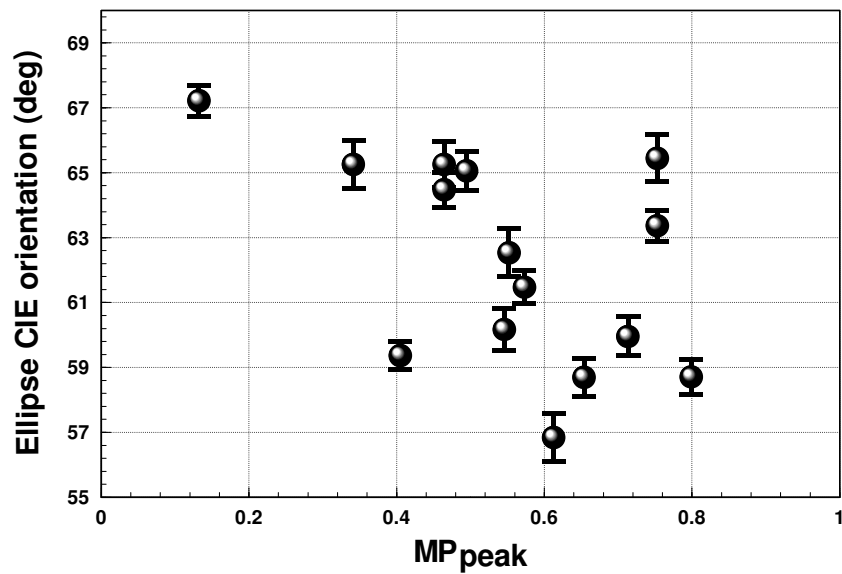


Fig. 6.2

Variations of fitted ellipse orientations in CIE space as a function of peak macular pigment levels. A non-significant trend exists ($r^2=0.56$, $p=0.054$).

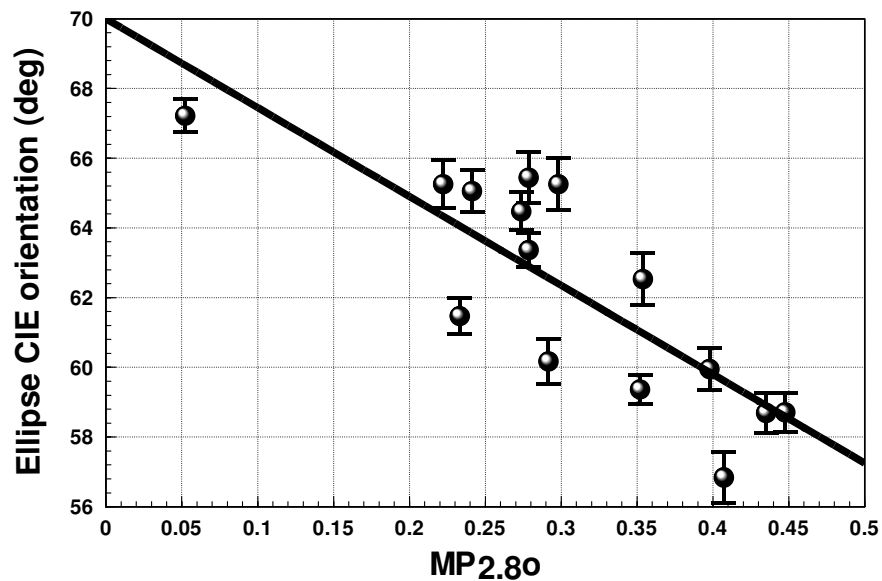


Fig. 6.3

Variations of fitted ellipse orientations in CIE space as a function of average central 2.8° macular pigment levels. A linear relationship ($r^2=0.67$, $p<0.05$) described by Eq. 6.2 is plotted as the solid black line.

The data shown in Fig. 6.3 shows that for the average orientation of 62.2° , an observer would be expected to have $MP_{2.8^\circ} \sim 0.3$. Ellipses with $MP_{2.8^\circ} > 0.3$ will be

orientated at a lower CIE angle relative to the mean ellipse orientation, i.e., their ellipse will appear to be rotated clockwise towards the deutan confusion line; this is consistent with previous finding of Moreland and Westland (2003). For $MP_{2.8^\circ} < 0.3$, ellipses are orientated at a higher CIE angle relative to mean ellipse orientation, i.e., the ellipse will appear to be rotated anti-clockwise towards the protan confusion line.

6.3.3 The effect of ellipse size and orientation on cone contrast curves

Cone contrast curves in CIE xy space (as introduced in chapter 2) are used to visualize the variation of L-, M- and S-cone contrasts along the contour of a threshold detection ellipse as a function of angle (θ_{cie}) in CIE xy colour space with respect to the foreground chromaticity location; this angle is zero when parallel to the positive CIE x axis. The observers' measured threshold ellipses varied in both size and orientation; these two parameters were investigated independently by two simulations assessing their effect on the cone contrast curves. A simulation was also performed which varied levels of macular pigment and re-calculated the "corrected" L-, M- and S-cone contrast curves; the cone contrast curves used for this were calculated from the standard CAD observer ellipse parameter. The following two sections describe the effect that simulated variations in ellipse size and ellipse orientation have on the L-, M- and S-cone contrast curves.

6.3.3.1 Variation of ellipse size and cone contrast curves

A series of ellipses were generated that varied in size using the standard CAD observer ellipse parameters. This was achieved by scaling the semi-major and -minor ellipse axes of the standard CAD observer ellipse by a range of factors from 0.5 to 1.5 in 0.2 spaced increments. These ellipses are shown in Fig. 6.4 in CIE xy space. The corresponding L-, M- and S-cone contrast curves were calculated for each of the simulated ellipses and are plotted in Fig 6.5(a), (b) and (c), respectively. The method for this transformation is outlined in chapter 2.

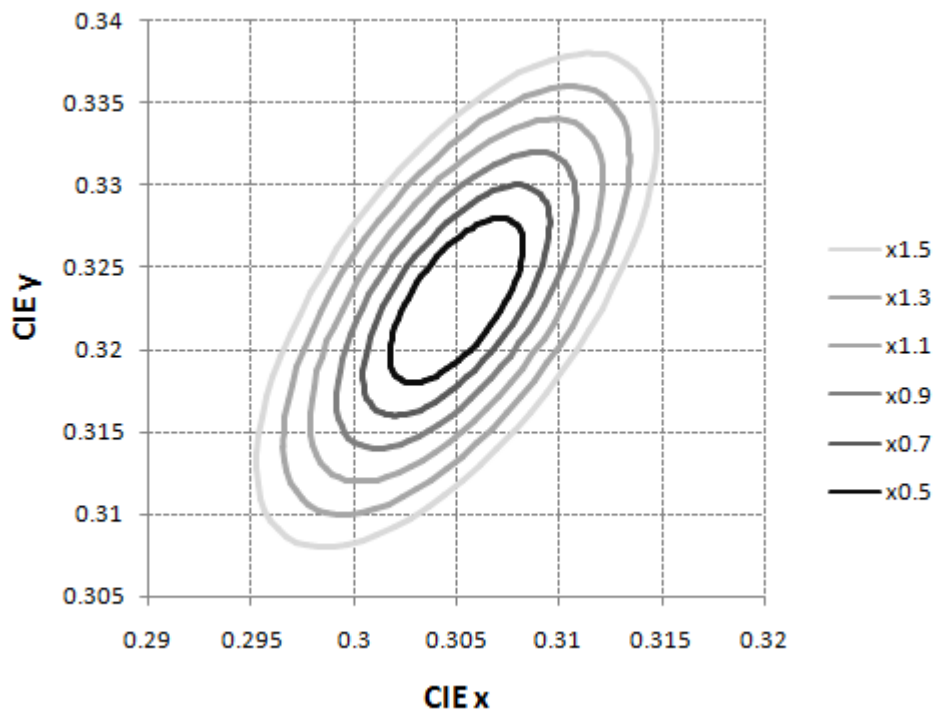


Fig. 6.4

The series of generated ellipses based on scaled values of the standard CAD observer's semi-major and -minor axes, the standard CAD observer ellipse would fall between ellipse x0.9 and ellipse x1.1.

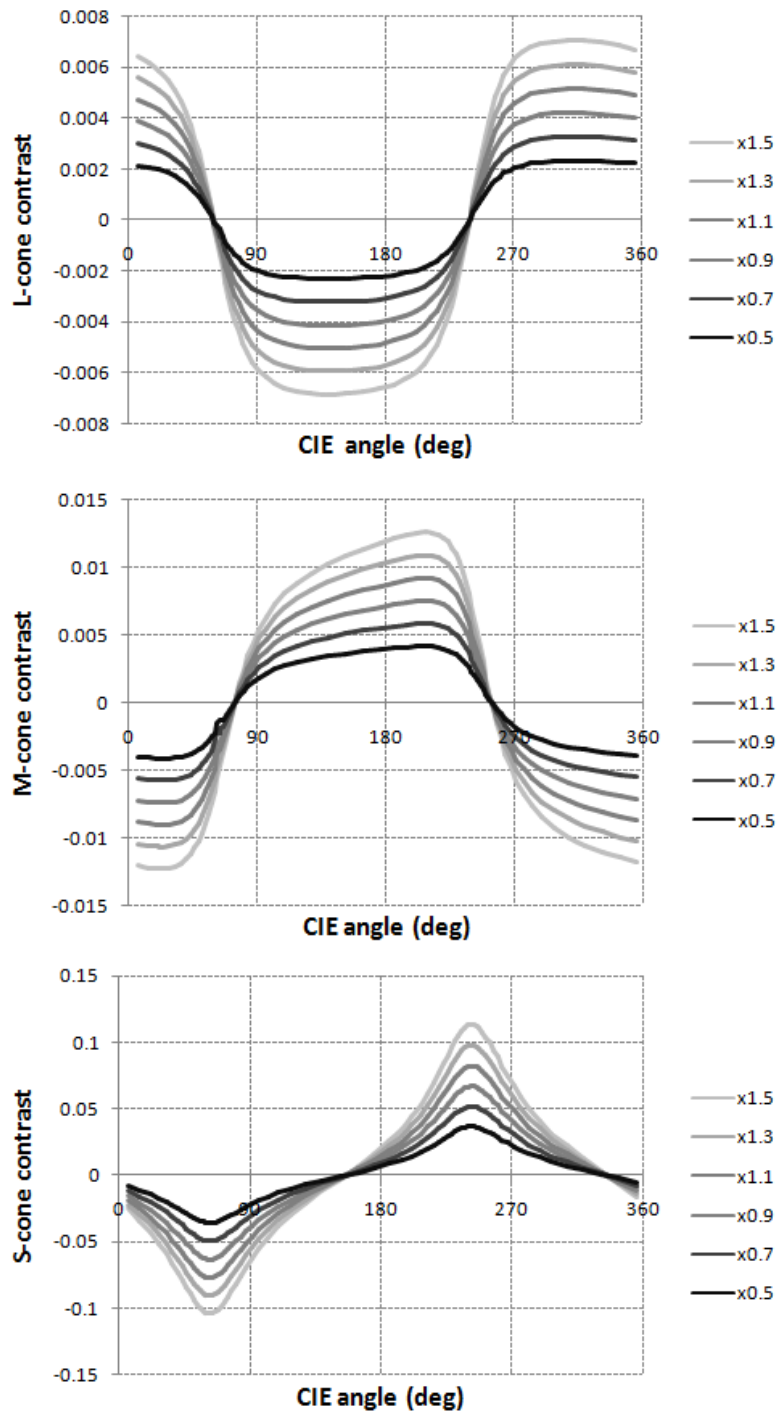


Fig. 6.5(a), (b) and (c)

The L-, M- and S-cone contrast curves plotted as a function of CIE angle (θ_{cie}); the greyscale corresponds to the grayscale used in Fig 6.4, for example the largest ellipse in Fig. 6.4 corresponds to the largest S-cone contrasts in Fig 6.5.

Relative to the whitish foreground and background at CIE xy: (0.305, 0.323) reddish chromaticities are represented, in the CIE xy colour direction range of angles from $\theta_{cie} \sim 297^\circ$ (wrapped around through zero degrees) to $\theta_{cie} \sim 7^\circ$ and the greenish chromaticities are represented in the range $\sim 117^\circ \leq \theta_{cie} \leq 187^\circ$. The results of this simulation indicate that as the ellipse size either increases or decreases both the L- and M-cone contrasts in the reddish and greenish CIE xy colour directions increase or decrease, respectively. The simulation also shows that in the yellowish ($\theta_{cie} \sim 60^\circ$) and bluish ($\theta_{cie} \sim 240^\circ$) colour directions, the S-cone contrast also increases and decreases with increasing and decreasing ellipse size, respectively. As the ellipse size is increased, the L- and M-cone contrast curves in the reddish and greenish directions also show a slight variation in gradient; this effect is slightly more visible in the M-cones.

6.3.3.2 Variation of ellipse orientation and cone contrast curves

In order to investigate the effect of ellipse orientation on the cone contrast curves, a series of ellipses were simulated that varied in orientation in both clockwise and anti-clockwise directions relative to the standard CAD observer. The standard CAD observer ellipse size was used and kept constant as it was rotated around its center coordinate. Two degree increments within the range $-6^\circ \leq \theta_{cie} \leq 6^\circ$ relative to its initial $\sim 62^\circ$ orientation were simulated. These simulated ellipses are shown in Fig. 6.6. The corresponding cone contrast curves were calculated for each of the simulated rotated ellipses, these are shown in Fig 6.7(a), (b) and (c) as a function of colour angle for the L-, M- and S-cones, respectively.

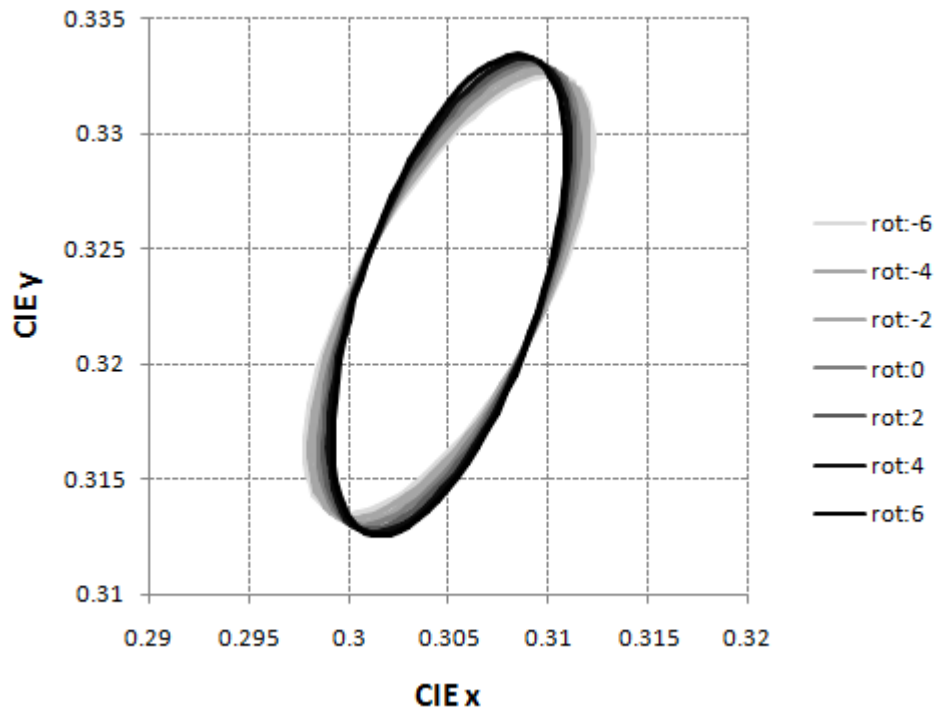


Fig. 6.6

The standard CAD observer ellipse, centered at CIE xy: (0.305, 0.323), is shown at rot:0 i.e., not rotated, the other ellipses are shown rotated relative to this within the range -6° to 6°.

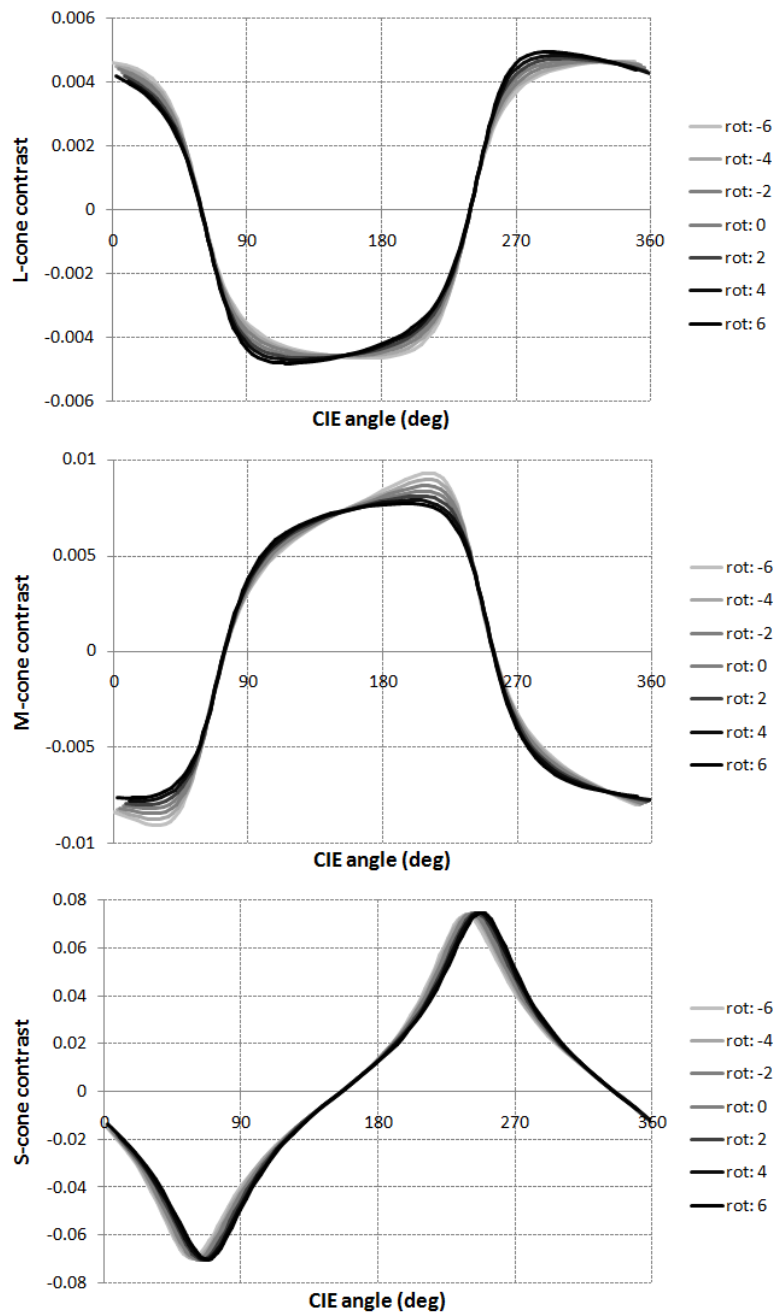


Fig. 6.7(a), (b) and (c)

The L-, M- and S-cone contrast curves contrast curves plotted as a function of CIE angle (θ_{cie}), the greyscale corresponds to the grayscale used in Fig 6.6.

Fig. 6.7(a), (b) and (c) show a smaller variation in L-, M- and S-cone contrast magnitudes compared with increasing or decreasing the ellipse size, but a much larger variation in the gradients of the L- and M-cone contrast curves in the

reddish and greenish colour directions. The S-cone contrast curves show a slight shifting of their peaks and troughs along the CIE angle axis, but with approximately constant maximum and minimum contrast values.

6.3.4 Extraction of L- and M-cone gradients from the fitted data

The gradients of the L- and M-cone contrast curves were extracted from the cone contrast curves within the reddish and greenish regions. The reddish and greenish CIE colour direction angle ranges, relative to the target at CIE xy: (0.305, 0.323), are defined as $117^\circ \leq \theta_{\text{cie}} \leq 187^\circ$ and $297^\circ \leq \theta_{\text{cie}}$ (wrapped around through zero degrees to) $\leq 7^\circ$, respectively. The L- and M-cone contrast curves follow a very strong linear relationship in these regions with typical r^2 values greater than 0.98; the gradients were calculated using a standard statistical ‘best gradient’ algorithm (Sheskin, 2007). This produced a set of four variables: the L-cone contrast gradient over the reddish and greenish regions ($L_{\text{grad_red}}$ and $L_{\text{grad_green}}$, respectively) and the M-cone contrast gradient over the reddish and greenish regions ($M_{\text{grad_red}}$ and $M_{\text{grad_green}}$, respectively). $L_{\text{grad_green}}$, for example, is calculated using Eq. 6.3.

$$L_{\text{grad_green}} = \frac{\Delta L_{\text{cont}}}{\Delta \theta} = \frac{n \sum L_{\text{cont}} \theta - \sum L_{\text{cont}} \sum \theta}{n \sum \theta^2 - (\sum \theta)^2} \quad \text{Eq. 6.3}$$

6.3.4.1 L- and M-cone gradients in the reddish and greenish colour directions

Four plots are presented that show the relationships between the gradients of the L- or M-cone contrasts for detections made in the reddish and greenish CIE xy colour directions as a function of the mean macular pigment level within the central 2.8° of visual angle. Fig. 6.8(a) shows the L-cone contrast gradients over the greenish colour direction range ($117^\circ \leq \theta \leq 187^\circ$) and Fig. 6.8(b) shows M-cone contrast gradients over the reddish colour direction range ($297^\circ \leq \theta$ (wrapped through 0°) $\leq 7^\circ$). No significant relationship exists between the variables shown in Fig. 6.8(a) or (b) and they are no longer considered.

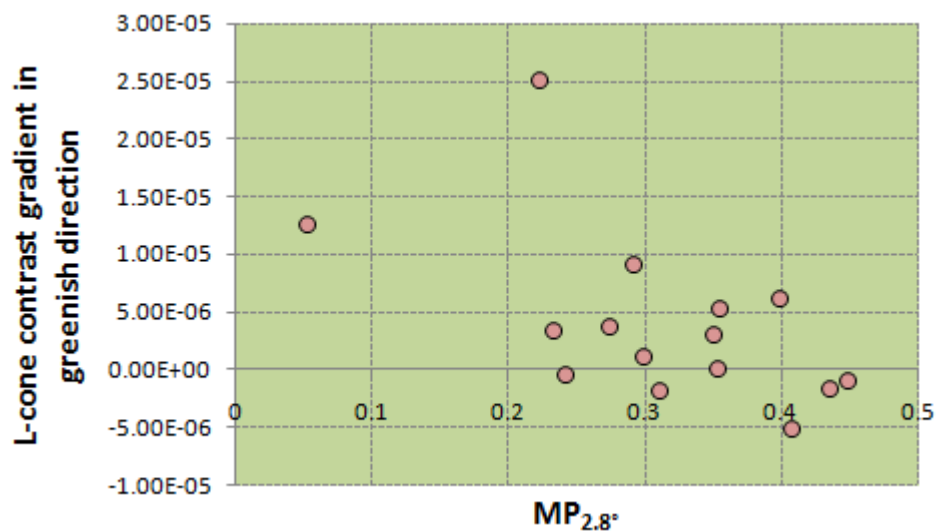


Fig. 6.8(a)

The gradients of the L-cone contrast curve over the greenish colour direction is plotted. No significant relationship exists ($p=0.084$).

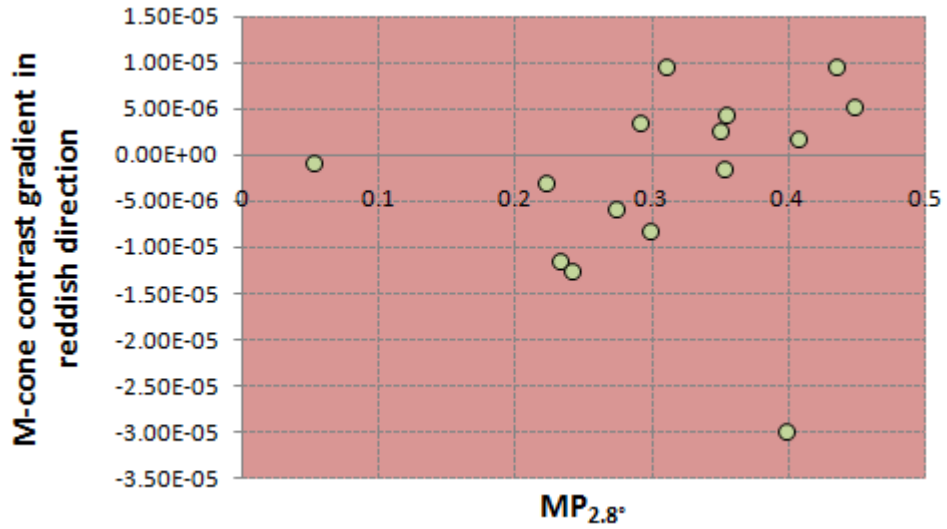


Fig. 6.8(b)

The gradients of the M-cone contrast curve over the reddish colour direction is plotted. No significant relationship exists ($p=0.10$).

Fig 6.9(a) shows the distribution of L-cone contrast gradients over the reddish direction and Fig. 6.9(b) shows the distribution of M-cone contrast gradients over the greenish colour direction, both plotted as a function of $MP_{2.8^\circ}$. The error bars are the maximum and minimum gradients derived from the raw CAD test data, i.e., they are the difference between the L- and M-cone contrast gradients for the two CAD test trials per subject. The mean differences are $\sim 7 \times 10^{-7}$ and $\sim 2 \times 10^{-6}$ for the reddish and greenish colour directions, respectively. Exponential curves were fitted to the datasets shown in Fig 6.9(a) and (b); these are described by Eq. 6.4 and 6.5, respectively. The data were reduced to a linear form and the product moment correlation coefficients were found to be $r^2 = 0.92$ ($p < 0.05$) and 0.86 ($p < 0.05$) for $L_{\text{grad_red}}$ vs. $MP_{2.8^\circ}$ and $M_{\text{grad_green}}$ vs. $MP_{2.8^\circ}$, respectively.

$$L_{\text{grad_red}} = -1.05 * 10^{-6} e^{4.89 MP_{2.8^\circ}} \quad \text{Eq. 6.4}$$

$$M_{\text{grad_green}} = 4.14 * 10^{-6} e^{6.06 MP_{2.8^\circ}} \quad \text{Eq. 6.5}$$

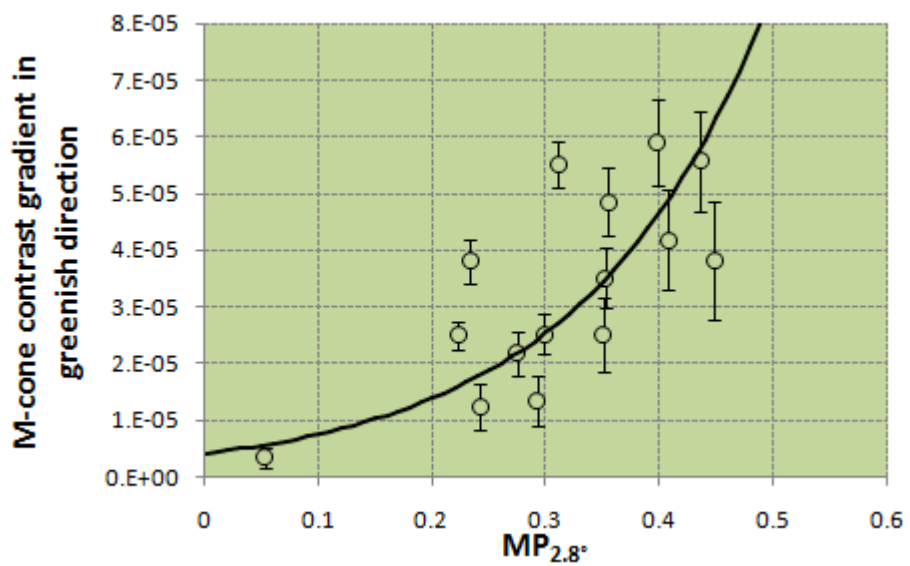
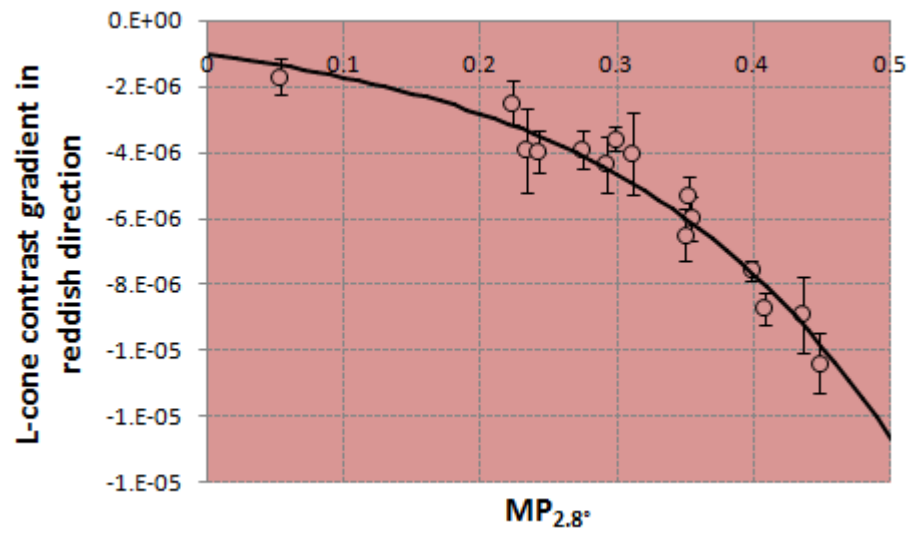


Fig 6.9(a) and (b)

The significant exponential relationships between L_{grad_red} and $MP_{2.8^\circ}$ (a) and M_{grad_green} and $MP_{2.8^\circ}$ (b) are plotted.

6.3.4.2 Predicting MP levels from cone contrasts

The highly significant relationship between the mean central 2.8° macular pigment level ($MP_{2.8^\circ}$) and the gradient of the L-cone contrast over the CIE reddish colour direction (L_{grad_red}) described by Eq. 6.4 can be used to estimate $MP_{2.8^\circ}$. Eq. 6.5 is derived from Eq. 6.4 and when tested for prediction accuracy yields a mean percentage error of $9.9 \pm 5.1\%$ (mean % error \pm SD) and provides a method of estimating an individual's macular pigment levels based only on their L-cone contrast curve.

$$MP_{2.8^\circ} = \frac{\ln(-L_{grad_red}) + 13.69}{4.69} \quad \text{Eq. 6.5}$$

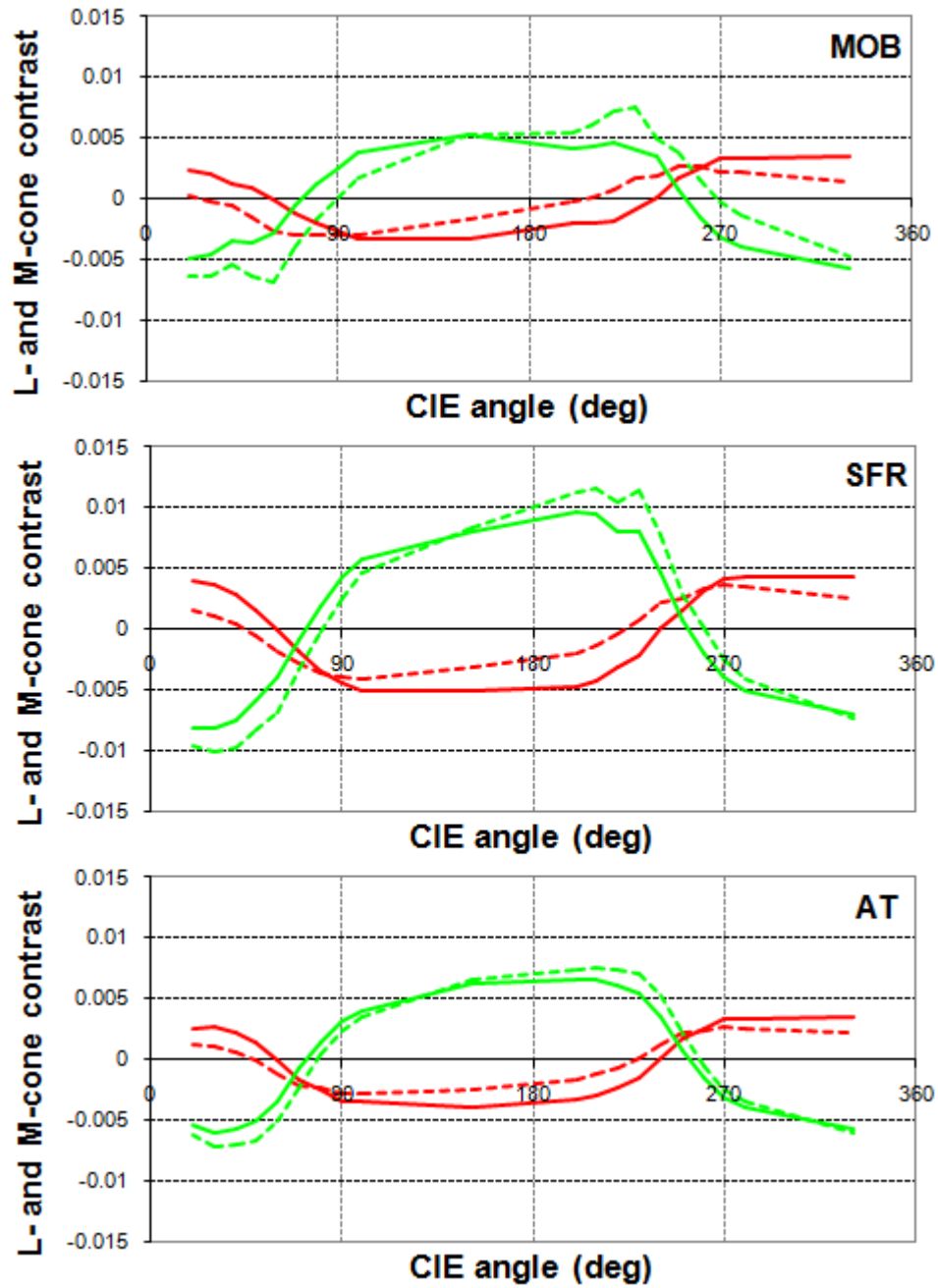
6.3.5 Correcting cone fundamentals for MP

When the chromatic stimulus is located at or very close to that observer's chromatic threshold an observer making a chromatic detection for a single CAD test presentation in either the reddish or greenish colour direction will not have any perception of the actual stimulus chromaticity, i.e., when they detect a stimulus at, or close to, threshold then the perceived colour remains largely invariant over the red and green ranges. This implies that the L- and M-cone contrasts required for threshold should vary over the reddish and greenish colour direction regions such that the total signal in the red-green chromatic channel remains unchanged, i.e., the $[L-M]_{cont}$ signal will be a constant over the two regions. This constant $[L-M]_{cont}$ contrast signal is independent of, for example, whether a green stimulus is a

greenish-yellow stimulus (when θ_{cie} is close to 117°) or a greenish-blue stimulus (when θ_{cie} is close to 187°). This constant $[L-M]_{cont}$ contrast signal at threshold would be achieved if the L- and M-cone contrast curves over the reddish and greenish regions were parallel. The calculated L- and M-cone contrasts presented so far in this chapter have been calculated using the Stockman-Sharpe cone fundamentals; in deriving this set of cone fundamentals the populations' mean macular pigment level was factored into them (Stockman and Sharpe, 2000). Some subjects in this study were found to have their L- and M-cone contrast curves aligned in a non-parallel fashion over the reddish and greenish directions. In order to test whether these non-parallel L- and M-cone contrast curves are the result of using the Stockman-Sharpe cone fundamentals (with a fixed MP level factored into them) as opposed to individual observer levels of MP, a set of cone fundamentals were calculated for each observer based on their measured peak macular pigment level. This was achieved by adjusting the Stockman-Sharpe cone sensitivities using the Bone (1992) macular pigment template. The Stockman-Sharpe cone fundamentals incorporate a macular pigment optical density with a peak value of 0.35; this macular pigment concentration was subtracted from each of the L-, M- and S-cone functions using the method outlined in Gegengurtner and Sharpe (1999, chapter 2). Once the mean macular pigment level had been removed from each of the cone sensitivity curves, an amount of macular pigment was factored back based on the peak measured value for each individual observer. The three cone contrast curves were re-calculated using the same method as before except that the individually adjusted cone sensitivities were substituted for the Stockman-Sharpe cone sensitivities. The four gradients L_{grad_red} , L_{grad_green} , M_{grad_red} and M_{grad_green} were also re-calculated.

6.3.5.1 Effect of macular pigment corrected cone sensitivities on the L- and M-cone contrast curves

When the individually adjusted cone sensitivities were used to calculate the L- and M-cone contrast curves it was observed that the L- and M-cone contrast curves over the reddish and greenish regions align themselves more closely parallel (i.e., the angle between them tends to zero) with the colour direction x-axis and also more parallel relative to each other. This is consistent with the above hypothesis regarding constant [L-M]-cone contrasts at threshold over these two regions. 6.10(a), (b) and (c) shows the raw (non-fitted) L- and M-cone contrasts vs. CIE angle for 3 subjects calculated using the Stockman-Sharpe cone sensitivities (dashed lines) and their corresponding individually MP adjusted L- and M-cone contrast curves (solid lines). These three subjects have $MP_{2.8^\circ}$ values that are spread throughout the measured range; $MP_{2.8^\circ}(\text{MOB})=0.05$, $MP_{2.8^\circ}(\text{SFR})=0.23$ and $MP_{2.8^\circ}(\text{AT})=0.41$. The individually MP adjusted cone contrast curves are shown to become more parallel to the colour direction x-axis; this effect can be observed clearly in Fig. 6.10(b) in the L- and M-cone contrast curves for subject SFR over the greenish region ($117^\circ \leq \theta \leq 187^\circ$).



6.10(a), (b) and (c)

Cone contrasts calculated with the Stockman-Sharpe (dashed lines) and individually macular pigment adjusted cone spectral sensitivity functions (solid lines) for subjects MOB, SFR and AT, respectively.

6.3.5.2 Effect of macular pigment corrected cone sensitivities on the S-cone contrast curves

The same adjustment as that performed with the L- and M-cones, was also performed on the S-cone contrast curves; they were also re-calculated with the individually adjusted MP cone sensitivities. It was found that between individuals with differing levels of $MP_{2.8\%}$, adjusting for this MP concentration had no significant effect on the S-cone contrasts at threshold. This was true for negative S-cone contrasts in the yellowish ($\theta_{cie} \sim 60^\circ$) colour direction and also bluish ($\theta_{cie} \sim 330^\circ$) positive S-cone contrasts, relative to the foreground chromaticity. This lack of shift in S-cone contrasts at threshold when adjusting for MP is illustrated in Fig. 6.11(a), (b) and (c) for the same three subjects as Fig. 6.10(a), (b) and (c), respectively. This observation is consistent with the reported invariance of S-cone contrast and macular pigment as reported by Rodriguez-Carmona *et al.* (2006). The solid lines are the Stockman-Sharpe calculated S-cone contrasts and the individual solid circles are the S-cone contrasts calculated from the individually MP adjusted cone sensitivities. The mean percentage difference between the MP adjusted and the Stockman-Sharpe calculated S-cone contrast curves for these three observers (MOB, SFR and AT) are only $(1.82 \pm 0.50)\%$, $(1.22 \pm 0.33)\%$ and $(0.54 \pm 0.14)\%$, respectively; this small difference is reflected in Fig. 6.11(a), (b) and (c) by the almost perfect alignment of the lines and circles.

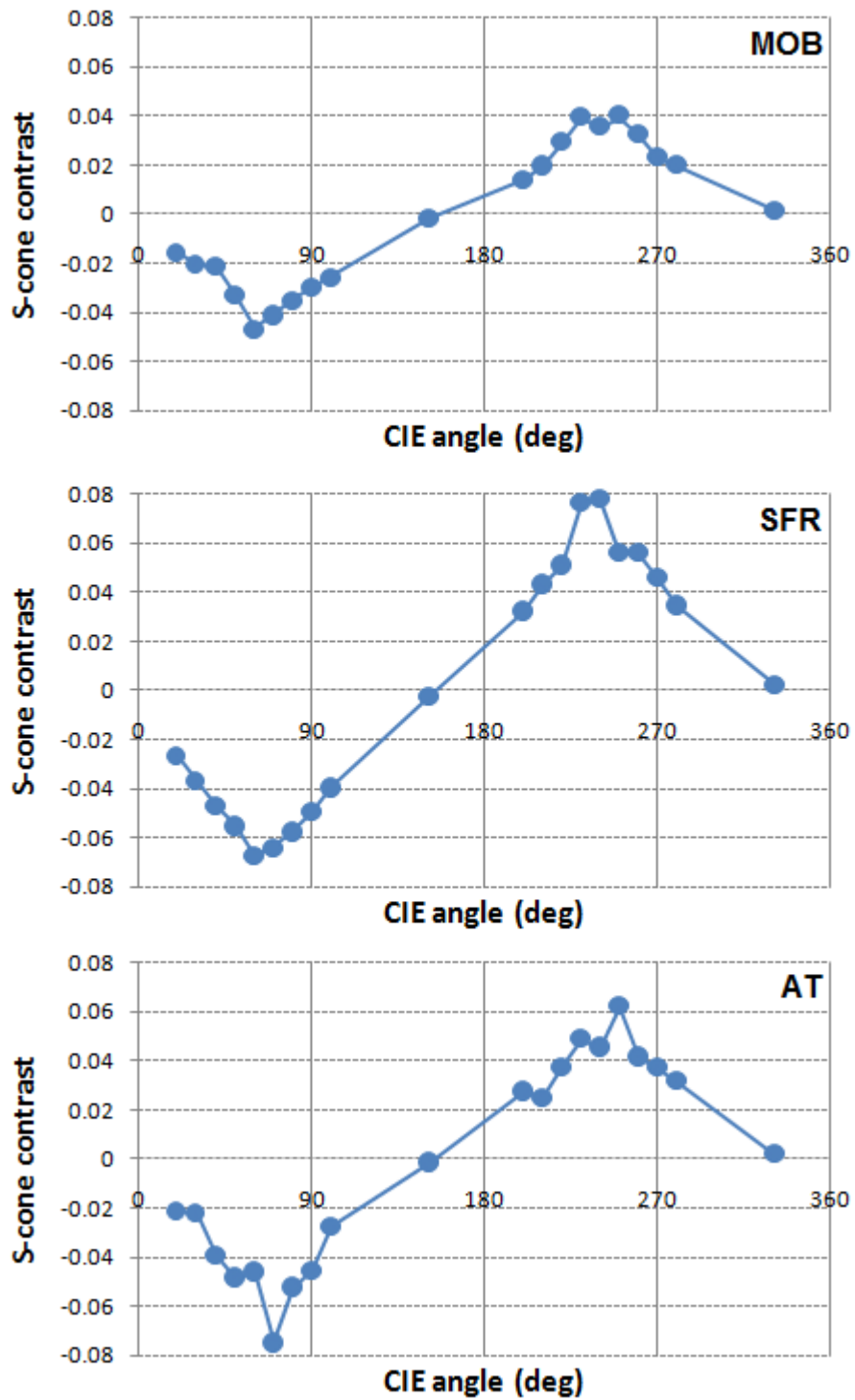


Fig. 6.11(a), (b) and (c)

S-cone contrast curves calculated using the Stockman-Sharpe (solid lines) and the individually MP adjusted S-cone spectral sensitivity functions (circles). Note the values of each are almost exactly equal.

The lack of change of S-cone contrasts when adjusting MP levels can be explained as follows, when making a detection of a chromatic stimulus on a chromatic foreground the difference between the S-cone excitations produced by the stimulus and foreground provide the S-cone contrast that the subject uses in order to make the detection. Macular pigment filtering affects the whole of the S-cones sensitivity range so the S-cone excitations of both the stimulus and foreground will be affected by equal amounts i.e., the macular pigment filters the stimulus and target by the same amounts. Therefore whilst the total S-cone excitation may change, the S-cone contrast required for threshold will remain constant and independent of macular pigment concentration. This finding forms the basis for the model described by Rodriguez-Carmona *et al.* (2006) to explain the lack of correlation between yellow-blue thresholds (in the $\pm S$ direction) and MPOD values.

6.3.6 Correcting cone fundamentals for lens yellowing

While the average age range of 14 of the 15 subjects tested was 29.3 ± 2.4 years (mean \pm SD), one observer was >50 years. It has been shown that the filtering effect of the crystalline lens varies dramatically over the course of a human lifetime as it loses its transparency becoming “yellow” (Weale, 1988). This is possibly due to damage from high energy photons within the blue region spectral power distribution of sunlight. The assumption was made that the 14 closely aged observers will possess similarly yellowed lens (as they had all been exposed to approximately the same amount of sunlight over their lifetime) and hence a correction for the yellow filtering was not applied. It was expected that the single older observer would appear as an outlier during the data analysis due to

increased lens yellowing; this is not the case so it was decided not to adjust any data for lens yellowing.

6.4 Discussion and conclusion

Within the tested set of $n=15$ subjects, a weak linear correlation existed between $MP_{2.8^\circ}$ and MP_{peak} . It was expected that the peak MPOD would not reliably give an estimate of the total (in this case $MP_{2.8^\circ}$) MPOD, in agreement with Neelam (2005). The measured detection ellipses were not orientated in CIE colour space dependent on MP_{peak} , but instead orientation was linearly related to the $MP_{2.8^\circ}$ levels. Ellipse size was found to affect the L- and M-cone contrast curves; increasing or decreasing them by fixed ratios over values of θ_{cie} . The effect of varying the ellipse orientation had a more interesting effect on the L- and M- cone contrast curves; a change in ellipse orientation caused a change in the gradient of the L- and M-cone contrast curves over the reddish and greenish CIE colour directions. The gradient of the L-cone contrast curve over the reddish colour region was significantly correlated with $MP_{2.8^\circ}$. This could be due to the filtering effect of the MP only partially overlapping the L-cone sensitivity range in the lower wavelength region of the sensitivity curve, as opposed to the S-cone sensitivity curve which has its whole range affected by the MP.

Adjusting individual subject's cone sensitivities for MPOD and re-generating the S-cone contrast curves had an insignificant effect on the contrast required for threshold. The relative cone excitations vary but the MP filtering will apply to both the foreground and stimuli so no change in contrast is required, although the S-cone excitations may vary. Loughman *et al.* (2008) found an MPOD independence

with colour discrimination along the yellow-blue confusion axis in agreement with results presented here. Loughman however attributes this (possibly) to a long-term chromatic adaptation effect that acts on the blue-yellow retinal pathway with respect to the prevailing MPOD; they show how this long-term chromatic adaptation can be temporally upset by applying a short-term chromatic adaptation using the Short-term Automated Perimetry Test (SWAP) (Racette, 2003). This technique involves decreasing the sensitivity of the L- and M-cones via the use of a chromatic adapting light which leads to the isolation of the yellow-blue chromatic pathway.

The main finding of the experiment presented here is that it is possible to reliably estimate (with a typical fitting error of <10%) an individual's mean central 2.8° MPOD using only a series of colour detections made over the reddish CIE direction (relative to CIE xy : (0.305, 0.323)).

Chapter 7

Cone noise, pupil size and photoreceptor excitation

7.1 Introduction

The first experiment (experiment 1 – pupil size) presented in this chapter investigates the variation in steady state pupil size as a function of L-, M- and S-cone, rod and melanopsin excitation following adaptation to a series of background chromaticities and light levels. The second experiment (experiment 2 – cone noise) investigates the L-, M- and S-cone signal-to-noise ratios as a function of colour space direction relative to a whitish adaptation point.

7.2 Introduction - Experiment 1

The human eye has an iris that defines the pupil and is formed of a partially opaque medium located on the outside surface of the lens. It can vary in size, i.e., the diameter of the pupil is not fixed, due to a variety of factors ranging from, for example, external lighting conditions to attentional loads (see chapter 1). This iris is known as the aperture stop; as it varies in diameter with the constriction or relaxation of the iris sphincter muscle only a small effect on the field of view of the eye is induced, but the total amount of light entering the eye will vary greatly, varying the retinal illuminance. Small and large pupil diameters correspond to low and high retinal illuminances (R_i), respectively. R_i is defined by Eq 1.5 (chapter 1).

A study presented by Atchison *et al.* (2011) demonstrated that if corneal flux density (F , the product of the stimulus size and luminance, measured in $\text{cd deg}^2 \text{m}^{-2}$) is constant the steady state pupil diameter will remain constant as the size of the stimulus field increases. This was shown for stimuli sizes in the range 1 to 24° and is illustrated in Fig. 7.1.

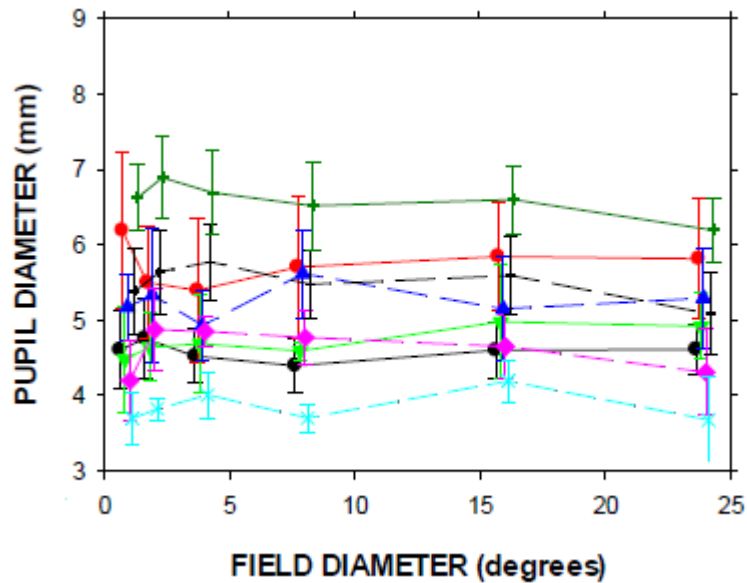


Fig 7.1

*A constant pupil diameter is observed as the stimulus field size is varied from 1 to 24° . Reproduced from Atchison *et al.* (2011).*

This result is consistent with Stanley and Davies (1995), they presented data for pupil diameters as a function of luminance for a variety of field sizes and conclude that the pupil control mechanism acts as a flux integrator, proposing that the pupil diameter (D in mm) can be estimated from the relation defined by Eq. 7.1 for a given corneal flux density (F).

$$D = 7.75 - 5.75 \left(0.41 \left(\frac{F}{846} \right) / \left(0.41 \left(\frac{F}{846} \right) / 2 \right) \right) \quad \text{Eq. 7.1}$$

However, both of these studies used the total amount of incoming white light as a measure of the input signal and failed to examine the differing contributions individual cone classes make to the control of pupil size. Bouma (1962) partially addressed this by investigating the variation of steady state pupil sizes when the eye was exposed to a series of different wavelengths. It was found that when the eye was chromatically adapted to a bluish light the state pupil size was smaller. It was not clear when the rods are saturated and not contributing to the perceptual experience whether they have some role in regulating the steady state pupil diameter. Laurens (1923) presented data relating pupil size to wavelength and showed it was dependant on the eye's adaptation state. The data for a light-adapted eye showed a minima at ~ 554 nm, whilst a dark-adapted eye showed a minima at ~ 514 nm, this could have possibly been due to both rods and cones influencing pupil size. De Launay (1949) performed an experiment that first dark adapted the eye and then slowly increased the incident light level, thereby allowing the eye sufficient time to adapt to the new light level, their data indicated that the pupil shows very little, if any, variation in pupil size, until the point that the cone threshold is exceeded. This experiment implied a cone only based mechanism for pupil control. These experiments did not however investigate the relationship between the individual L-, M- and S-cone excitations and the steady-state pupil diameter. Another candidate for pupil size control are the photosensitive Retinal Ganglion Cells (ipRGC). Hattar *et al.* (2002) showed in rats the ipRGCs expressed melanopsin and concluded that this pigment could be responsible for phototransduction that inputs into non-visual processes. Zaidi *et al.* (2007) extended this finding and showed in humans that these cells can input into visual and non-visual mechanisms, such as pupil control. Tsujimura *et al.* (2010) performed an experiment that isolated the cones and ipRGCs via the use of

narrow band light emitting diodes, they showed that changes in pupil size when the melanopsin is stimulated is ~3 times larger than that of the summed L- and M-cones, i.e, the luminance signal. They suggest that the ipRGC and cones contribute to the steady state pupil size via some unknown non-linear signal summing, but some issues exist in the isolation due to the large overlap of melanopsin, S-cone and rod sensitivity curves. The following experiment was conducted in order to examine the relationship between the individual chromatically adapted photoreceptors and the steady state pupil size.

7.3 Method and data collection

The five subjects, all with normal colour vision, as assessed by the Colour Assessment and Diagnosis (CAD) test had their steady state pupil diameters measured during exposure to a series of background lights of different chromaticities, displayed over a range of luminance levels. In total, eight different chromaticities were employed over a maximum of six luminance levels; not all chromaticities were reproducible for each luminance on the CRT display. Table. 7.1 lists the CIE xy coordinates of the chromaticities tested and summaries reproducible luminance levels for each chromaticity employed in the study.

CIE x	CIE y	Luminance level (cd m ⁻²)					
		31	24	16	8	3	1
0.305	0.323	✓	✓	✓	✓	✓	✓
0.285	0.558	✓	✓	✓			
0.3977	0.3283	✓	✓	✓	✓	✓	
0.385	0.472	✓	✓	✓	✓	✓	✓
0.265	0.25	✓	✓	✓	✓	✓	
0.25	0.3	✓	✓	✓	✓	✓	
0.3	0.22	✓	✓	✓	✓		
0.215	0.1745	✓	✓	✓			

Table. 7.1

The CIE xy coordinates of each of the tested chromaticities, the ticks indicate that the chromaticity was reproducible on the CRT display and hence pupil sizes at that chromaticity and luminance level were measured.

The experimental procedure was as follows; the subject was exposed to a test chromaticity displayed uniformly, at a given luminance, over the entire CRT display (22° x 27°). Subjects were chromatically adapted by fixating the display for ~90 s. Using the P_Scan pupillometer the steady state pupil diameter was measured (see chapter 2). This process was repeated for each of the reproducible chromaticity and light level combinations for each subject. The chromaticities at each light level were transformed in the corresponding L-, M- and S-cone excitations and rod excitations that they produced using the method outlined in chapter 2. For each condition the data were averaged across subjects.

7.4 Results

Fig. 7.2 is a summary of the results; it plots the mean pupil diameters as a function of the adapting field luminance level. The symbol colours approximate the

adapting chromaticities. It can be observed that for each chromaticity tested decreasing luminance levels results in larger pupil diameters (D_{pupil}), this is consistent with many previous studies, for a summary see Oyster (2006). However the pupil diameters for given luminance levels are not necessarily equal, i.e., they are shown to be dependent on the adapting chromaticity; for example at 16 cd m^{-2} a yellowish adapting field will produce a pupil that is ~ 1.7 times the diameter as that produced by a bluish adapting field.

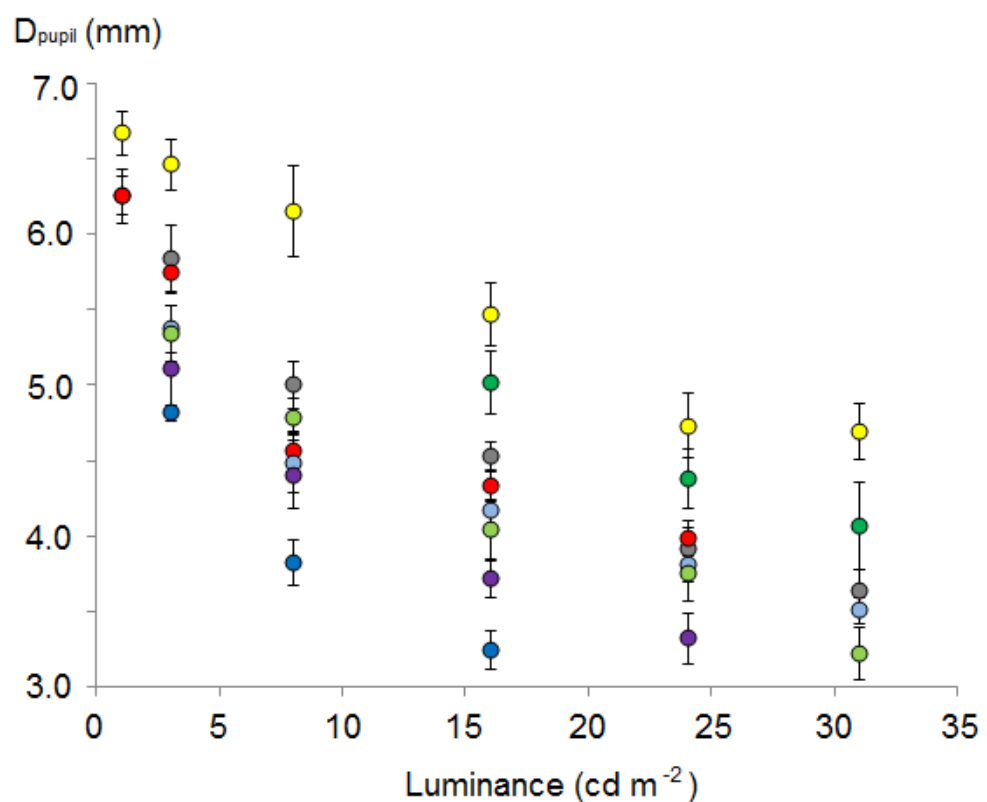


Fig. 7.2

Pupil diameter a function of luminance level, as the luminance increases the pupil diameter decreases, but for a given luminance the pupil diameter is also dependant on the adapting chromaticity.

The relationships between pupil diameter and the L-, M- and S-cone excitations (and rod excitation) are presented in the following figures; Fig. 7.3, 7.4(a) and (b),

and 7.5, each of these plots have fitted linear regression lines and in all cases these were calculated for the whole dataset collapsed across chromaticities; note, the data have again been plotted in a colour coded manner so as to approximately indicate the adapting field chromaticities.

7.4.1 Pupil size vs. rod, cone and melanopsin excitation

The rod excitations were calculated using the scotopic luminous efficiency function (CIE Proceedings, 1951) along with an analogous method to that used to calculate the cone excitation. Fig. 7.3 shows the mean pupil diameter plotted as a function of $\log(\text{Rod-excitation})$, the relationship is described by Eq. 7.2.

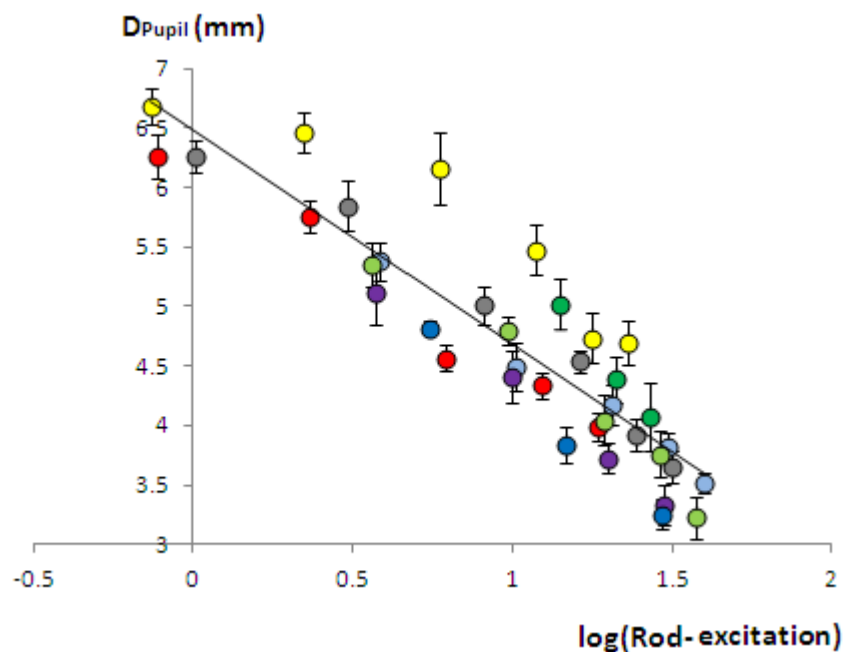


Fig 7.3

The mean pupil diameters (D_{pupil}) plotted as a function of $\log(\text{Rod excitation})$ ($R^2 = 0.82, p < 0.05$), the fitted line is given by Equation 7.2.

$$D_{pupil} = -1.8 \log(R_{excitation}) + 6.5$$

Eq. 7.2

The L- and M-cone excitations were calculated for each adapting field chromaticity at each reproducible luminance level. Fig. 7.4(a) and (b) show the mean pupil diameter plotted as a function of $\log(\text{L-cone excitation})$ and $\log(\text{M-cone excitation})$, respectively. The corresponding fitted functions are indicated by Eq. 7.3 and 7.4, respectively.

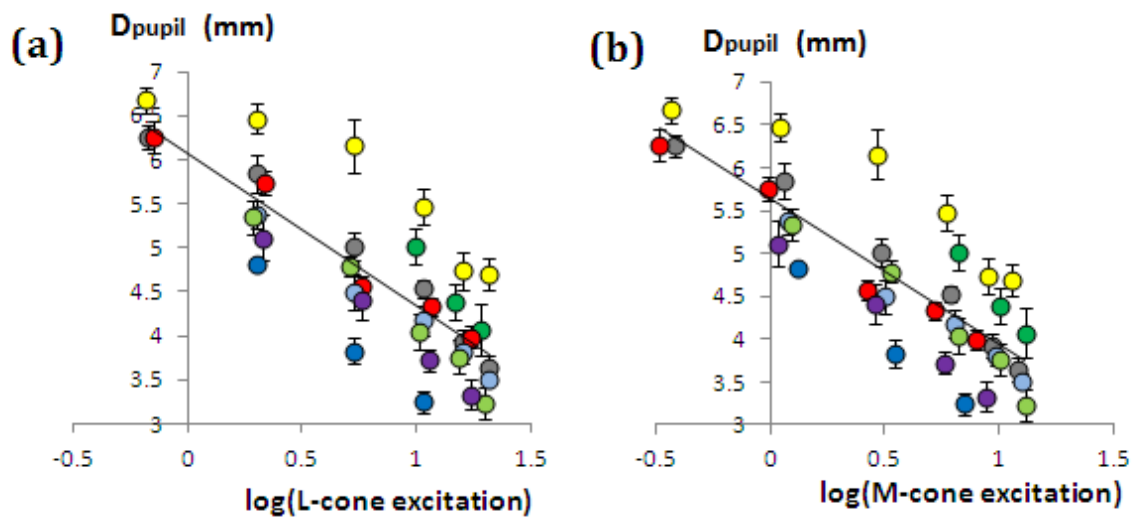


Fig 7.4(a) and (b)

The mean pupil diameters (D_{pupil}) plotted as a function of $\log(\text{L-cone excitation})$ ($R^2 = 0.68, p < 0.05$) in (a) and $\log(\text{M-cone excitation})$ ($R^2 = 0.68, p < 0.05$) in (b), the fitted lines are given by Equation 7.3 and 7.4, respectively.

$$D_{pupil} = -1.7 \log(L_{excitation}) + 6.1 \quad \text{Eq. 7.3}$$

$$D_{pupil} = -1.7 \log(M_{excitation}) + 5.6 \quad \text{Eq. 7.4}$$

The S-cone excitations were also calculated for each adapting field chromaticity at each reproducible luminance level. Fig. 7.5 show the mean pupil diameters plotted

as a function of $\log(\text{S-cone excitation})$, the corresponding fitted function is indicated Eq. 7.5.

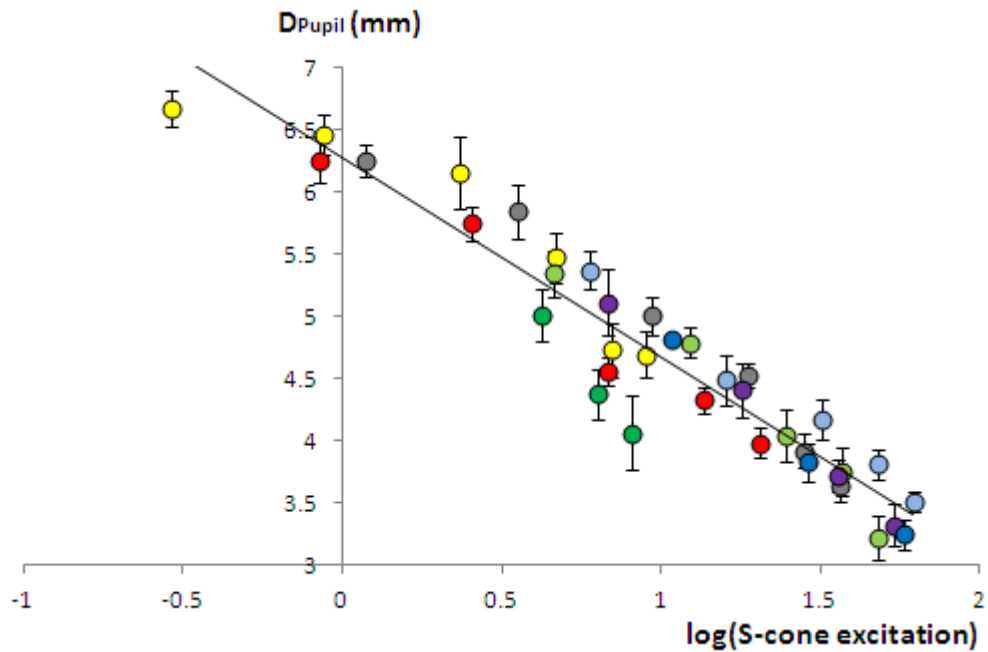


Fig. 7.5

The mean pupil diameters (D_{pupil}) plotted as a function of $\log(\text{Rod excitation})$ ($R^2 = 0.91$, $p < 0.05$), the fitted line is given by Equation 7.5.

$$D_{pupil} = -1.6 \log(\text{S}_{excitation}) + 6.3 \quad \text{Eq. 7.5}$$

Finally the melanopsin excitations were calculated, these data are plotted against pupil size in Fig. 7.6. The fitted relationship is indicated by Eq. 7.6.

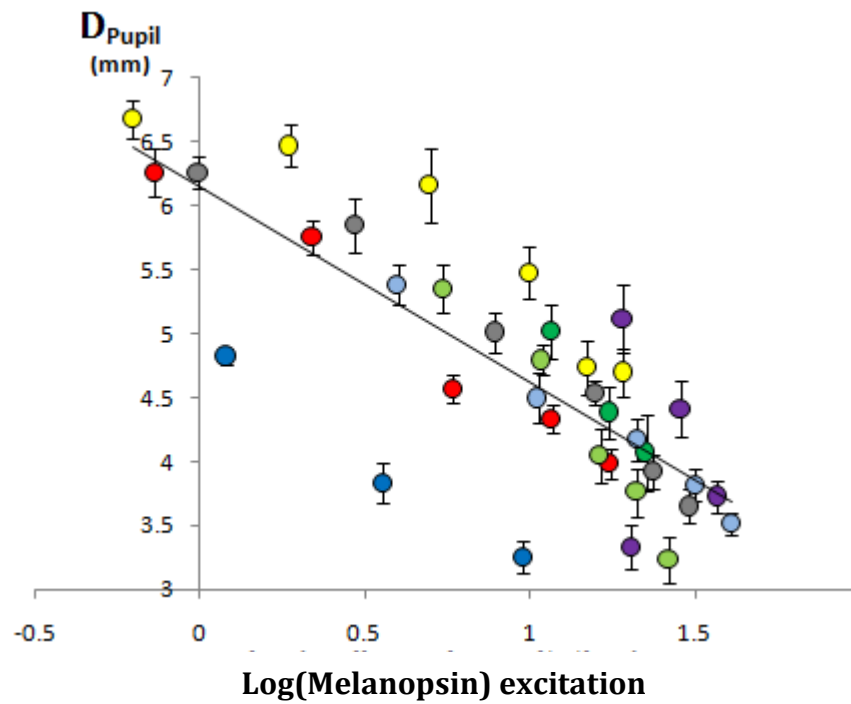


Fig. 7.6

The mean pupil diameters (D_{pupil}) plotted as a function of $\log(\text{melanopsin excitation})$ ($R^2=0.63, p<0.05$), the fitted line is given by Equation 7.5.

$$D_{pupil} = -1.6 \log(M_{excitation}) + 6.1 \quad \text{Eq. 7.6}$$

7.5 Conclusion - experiment 1

Within the range investigated the data presented in Fig. 7.2 illustrate that the steady state pupil size after adaptation to different chromaticities can differ widely, even when the luminance remains unchanged. These data are consistent with that of Bouma (1962) that showed bluish/purple chromaticities, composed of short wavelength light, will produce the smallest steady state pupil sizes for a given light level. Further analysis using the cone excitation levels reveal that the S-cone excitation is most highly correlated with the steady state pupil size. The rod excitation was correlated significantly but to a lesser extent than the S-cones, and

finally the L- and M-cones and melanopsin excitations were correlated with pupil size, but again to an even lesser extent. Whilst it cannot be concluded from these data that the S-cones have a dominant input to the pupil size, and it is possible a non-linear combination of inputs is responsible, it is interesting to note that the correlation is not dependant on absolute luminance level. For example, a blue which produces a relatively high S-cone excitation and a green (which produces only a small S-cone excitation) could be displayed in such a way as to produce equal S-cone excitations (by reducing the luminance level of the blue). In spite of the large difference in luminance, the blue and green lights produce very similar steady state pupil sizes.

7.6 Introduction - experiment 2

After performing the within subjects experiment presented in chapter 3, the question arises as to how much variation exists when chromatic threshold measurements are repeated within a single observer. The investigation described in this section addresses this and derives an estimate of what can be considered as the cone noise (and hence the signal-to-noise ratios) over a range of colour directions. The signal-to-noise estimate used in this study is one that is commonly employed in a variety of different fields, e.g., medical imaging (Bushberg, 2006), is defined by Eq. 7.7.

$$SNR = \frac{\bar{X}}{\sigma} \quad \text{Eq. 7.7}$$

Where, \bar{X} is the mean signal (contrast) and σ is an estimate of the noise, assumed to be equal to the standard deviation of the mean.

7.7 Method and data collection

A set of twenty one threshold detection ellipses were measured under the same conditions for two observers (BJ and MRR). This allowed the cone noise to be estimated from the standard deviations derived from the multiple threshold measurements (in terms of chromatic displacements). The CAD system was used to obtain thresholds along twenty equally distributed directions in CIE xy colour space relative to the adapting background. Both the background and foreground chromaticity was located at CIE xy : (0.305, 0.323), and both displayed with a luminance of 24 cd m⁻². The time to measure twenty one detection ellipses represented more than 4 hours of psychophysical testing per observer, hence the testing was carried out over 4 sessions on separate days. The L-, M- and S-cone contrasts required for threshold were calculated from measured chromatic displacement thresholds in CIE space for each colour direction. The mean and standard deviations, and hence signal-to-noise ratios were derived. These are presented as a function of colour direction (in degrees) and in cone L-M vs. S-contrast space in the following section.

7.8 Results

The results obtained for the two observers were similar, observer BJ's data will be presented. Fig. 7.7 shows the distribution of the repeated measurements of

thresholds plotted in CIE xy space for each colour direction tested. Fig. 7.8 shows the relationship between the coefficients of variation (CoV) over the range of colour directions tested. The CoV is observed to remain relatively low (~18%) over the whole range with no significant differences existing over the range ($p < 0.05$).

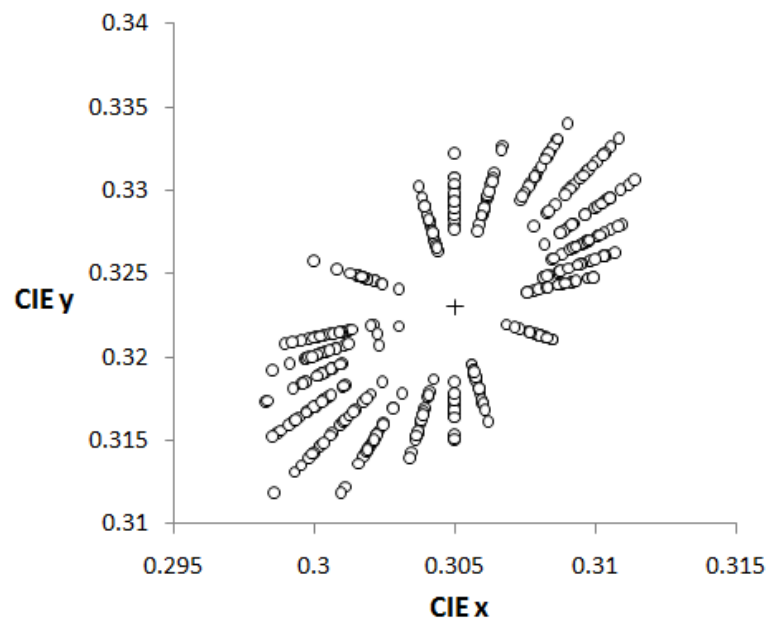


Fig. 7.7

21 repeated threshold measurements are plotted in CIE xy space for the 20 colour directions tested. The “+” indicates the location of the background and foreground chromaticity.

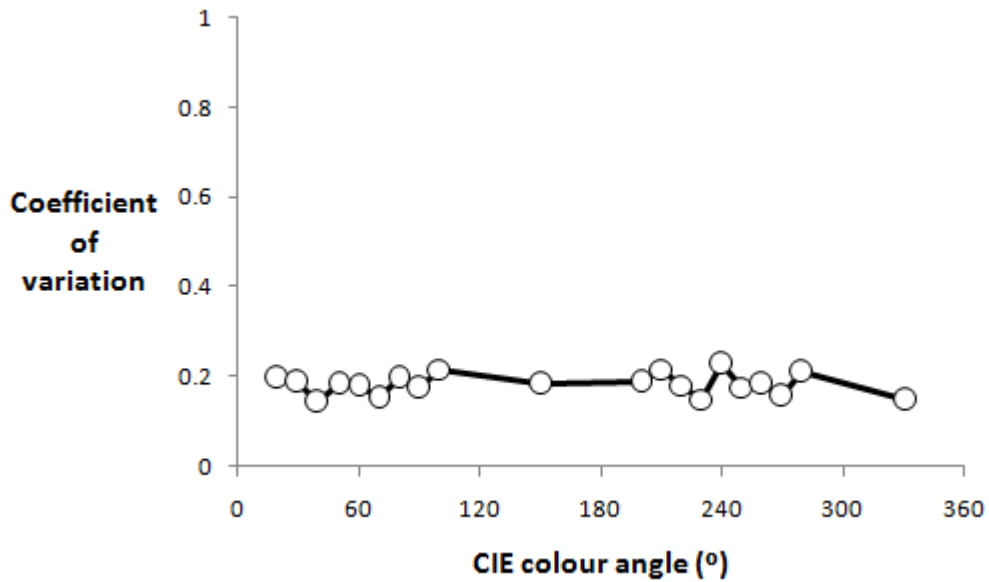


Fig. 7.8

The coefficient of variation vs. CIE colour angle for observer BJ. The CoV remains low and independent of colour angle across the whole range.

7.8.1 Variation of L-, M and S-cone contrast signal-to-noise ratio

The L-, M- and S-cone signal-to-noise ratios were calculated in terms of cone contrast for each colour direction. Fig. 7.9(a) shows the variation as a function of colour direction; 0, 90 180 and 270° correspond to the reddish, bluish, greenish and yellowish colour directions, respectively (see insert within Fig. 7.9(a)). Fig. 7.9(b) plots only the L- and M-cone contrasts for clarity.

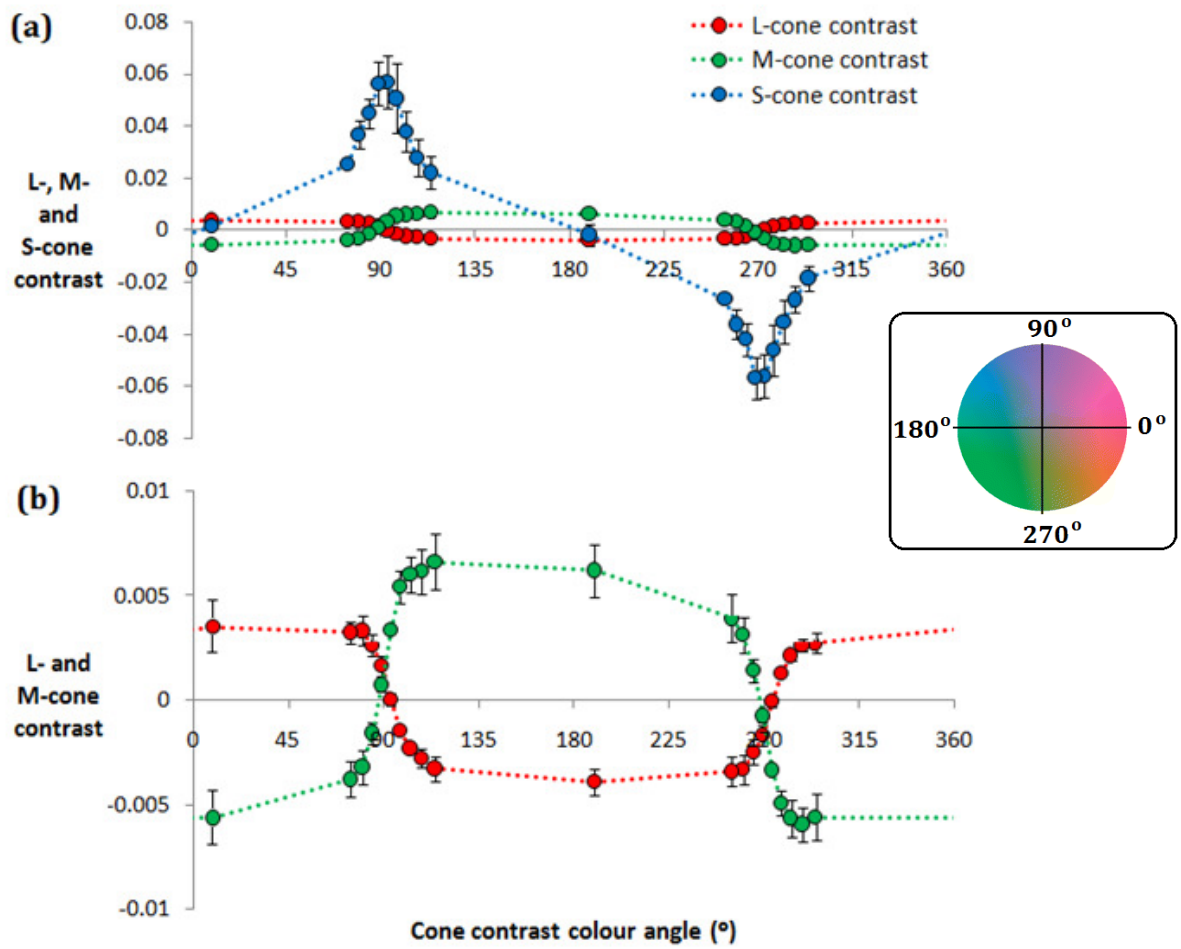


Fig 7.9(a) and (b)

The L-, M- and S-cone contrasts (plotted as red, green and blue circles, respectively) as a function of cone contrast space angle are shown in (a). The L- and M-cone contrast curves from (a) are plotted alone in (b) for clarity.

(Insert in (a) indicates the distribution of chromaticities over cone contrast space).

As a linear model of cone excitation is assumed the thresholds in terms of CIE chromatic displacement correspond proportionally to L-, M- and S-cone contrasts at threshold, therefore any variance in thresholds within one cone class will be present and equal in the other cone classes for a given direction. It should be noted that within CIE xy space this proportional relationship becomes non-linear for high contrast levels, but the contrasts presented here are low and within the

linear region. As the magnitude of the S-cone contrast increases around 90° (bluish) and 270° (yellowish) in cone contrast space, the noise increases in such a way as to keep the signal-to-noise ratio constant. This is also observed in Fig. 7.9(b) for the L- and M-cones, where a larger contrast corresponds to a larger noise level, this occurs in both the reddish and greenish colour directions (0 and 180°, respectively). Fig 7.10 plots the absolute values of signal-to-noise ratio for each chromatic direction tested, the dashed black line indicates the mean, the grey shaded area indicates the 95% confidence interval. The signal-to-noise level averaged over all colour directions, is 5.56 ± 0.77 (mean \pm SD).

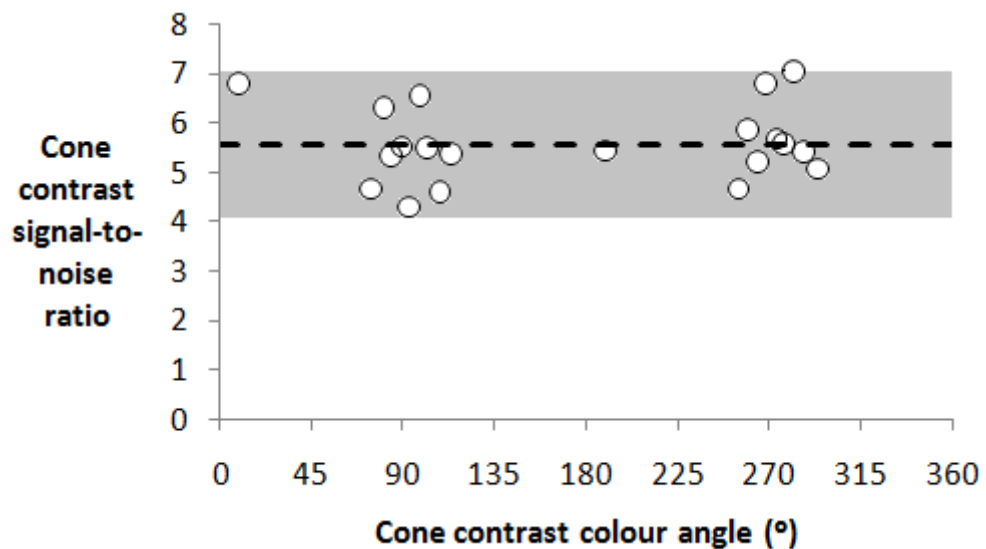


Fig. 7.10

The cone signal-to-noise ratios plotted as a function of cone contrast space colour direction, the mean value (~5.6) is indicated by the dashed line, the grey area indicated the 95% confidence interval.

7.9 Conclusion – experiment 2

It has been shown that as the radius of the ellipse varies with colour direction, i.e., the chromatic displacement required for threshold, the noise also varies; this variation increases and decreases so as to maintain a constant coefficient of variation, observed in both subjects BJ and MRR (~18% and ~23%, respectively). When these thresholds are transformed into L-, M- and S-cone contrasts, it is shown that the cone signal-to-noise ratios are also constant, over the three cone types in all colour directions. The results show that in the yellowish and bluish directions, that are dependent on the S-cone contrast alone being ~6% used (the stimulus is presented under isoluminant conditions so the L+M contrast is zero), the noise increases as the S-cone signal increases. Similarly over the reddish and greenish colour directions, where the L- and M-cones both reach threshold at ~0.5% contrast, the signal-to-noise is also constant in this region. In contrast space S-cones only contribute to detection at threshold within two relatively small ranges, from ~75 to 105° (the bluish region) and ~255 to 285° (the yellowish region). In all other directions outside of these S-cone ranges the L- and M-cones are used for either greenish or reddish detection. The noise levels close to these transitions are likely to be artefacts arising due to, for example, the S-cone contrasts being calculated in every direction even when they are not made use of. At 80° in contrast space, for example, the S-cones are active and used for detection of a stimulus with +S contrast, in this direction the calculated signal-to-noise ratio in the L- and M-cones remains at ~5, but this value is essentially irrelevant and needs not be considered as they play no active role in the detection. In conclusion, provided that a cone class is actively contributing to detection, at threshold, the signal-to-noise ratio will remain constant at ~5.

Final conclusions

The majority of experiments reported in this thesis investigated how chromatic detection sensitivity varies under different states of light adaptation. Both chromatic and light level variations were investigated. These variations are of practical importance since they represent frequently encountered conditions particularly in visually-demanding working environments. Many examples of work places exist where employees are subjected to illumination conditions that induce chromatic adaptation. An example is the lighting within an airplane cockpit during a flight at night; pilots are subjected to a background illumination that is often reddish and may be tasked with reading a map that contains airspace marking printed in red against a blue or green background (representing water or land, respectively). It is hence useful to be able to predict the limits of chromatic detection capability under a variety of conditions in order for colour coding to be implemented, for example in maps or safety critical instrumentation. In order to study chromatic detection the Colour Assessment and Diagnosis test was employed, it isolates colour signals by embedding the isoluminant chromatic stimulus within dynamic luminance contrast noise. A series of detection threshold ellipses were measured for different states of chromatic adaptation. This was done for adapting background and foreground (upon which detections were made) combinations that were located either in the same (chapter 3) or in different (chapter 4) locations in colour space. The measured ellipses were analysed in terms of the differences in L-, M- and S-cone excitations required for threshold. A model is proposed that can predict the threshold ellipses accurately for a range of background chromaticities. This model assumes the ellipse semi-major axis aligns with the S-excitation axis (this is consistent with the measured data) when the

background and foreground are equal. When the background and foreground are unequal, i.e., when detections are made away from the adaptation point, a change in ellipse orientation is observed, the ellipse semi-major axis rotates to align more closely along the direction towards the adaptation point. These ellipse orientations can be predicted accurately from the difference in cone excitations produced by the background and foreground combination. For the conditions when an equal background and foreground combination was employed additional ellipses were measured over a series of light levels, typically from 0.3 to 31 cd m⁻². The findings from these experiments show that when a cone class is adapted to a given excitation level, the signal at threshold is independent of the light level and chromatic combination employed to achieve adaptation and is also independent of the adapted state of the other cone classes.

The results from the experiment presented in chapter 5 indicate that foveal colour thresholds remain independent of the adapted state of the peripheral retina, i.e., no long range retinal interactions are demonstrated.

The effect that macular pigment optical density can have on colour detection thresholds was investigated (chapter 6). Measurement of observers' peak and mean macular pigment optical densities were obtained over the central 2.8° of visual angle and these two measures approximately correlated as expected. Controlled simulations that varied the chromatic threshold ellipse size and orientation in order to assess theoretical variations in the cone contrast curves were performed. These simulations revealed that changes in ellipse orientation caused either an increase or decrease in the L- and M-cone contrast curve gradients over the reddish and greenish colour directions, relative to the colour direction axis. Subsequent analysis of observers' measured ellipse orientations

along with the measured macular pigment optical densities was performed; these were also related to the cone contrast curves. It was found that the variation in the L-cone contrast curve gradient was highly correlated with macular pigment optical density; this provides a method for estimating macular pigment levels from the L-cone contrasts required for threshold alone. At threshold the hue of a reddish or greenish CAD stimulus is not perceived, i.e., observers cannot discriminate yellowish-reds from bluish-reds, or yellowish-greens from bluish-greens. This implies that the L- and M-cone contrasts over the reddish and greenish regions should be constant. It is shown that when the cone sensitivity functions are individually corrected for the filtering provided by an individuals' macular pigment optical density the cone contrasts over these regions become more stable, i.e., aligned more parallel with the colour direction axis. Correcting for macular pigment differences does not change the S-cone contrasts; this is due to the filtering effect of the macular pigment effecting both the background and stimulus (within the foreground) by an equal amount. So while the S-cone excitations may change, when expressed in terms of contrast they remain constant.

Previous studies that investigated steady state pupil size have been extended (chapter 7). Pupil sizes were measured after adaptation to a range of chromaticities and light levels, this allowed for analysis to be performed that related the measured pupil size to individual L-, M- and S-cone excitations. Consistent with an earlier study, the smallest pupil size was found to correspond to exposure to light composed of short wavelengths. The S-cone excitation was found to be highly correlated with the steady state pupil size and also to be independent of the adapting chromaticity and luminance level that induced it. Noise within colour mechanisms was also investigated; signal-to-noise ratios were derived from

repeated measurements of detection ellipses and are shown to be constant over all colour directions. This result indicates that in a particular cone class as the contrast level required for threshold increases so does the noise level. When a cone class is not playing an active role at threshold, for example the S-cones when a reddish colour is being detected, the noise level will be small. On the other hand when the S-cone signal is being used at threshold, for example when making detections in the yellow direction, their noise level will increase, but the signal-to-noise ratio will remain constant. These observations suggest that red-green and yellow-blue chromatic mechanisms are independent at threshold.

The principal outcome from this study is the ability to predict accurately colour detection thresholds against a range of light levels and adapting chromaticities. The practical applications of the findings remain to be explored.

References

- Anderson, DFT. (2008). Curvilinear analysis of learning for cost estimation. SWDSI proceedings. Decision sciences unit. University of New Mexico. USA.
- Arda, H. Oner, A. Mutlu, S. Kose, Z. Gumus, K. Karakucuk, S. Mirza, E. (2006). Multifocal electroretinogram for assessing sun damage following the solar eclipse of 29 March 2006: multifocal electroretinography in solar maculopathy. *Doc Ophthalmol*, 114 :159-162.
- Atchison, DA. Girgenti, CC. Campbell, GM. Byrnes, TM. Zele, AJ. (2011). Influence of field size on pupil diameter under photopic and mesopic light levels. *Clinical and Experimental Optometry*, 94(6):545-548.
- Barbur, JL. Konstantakopoulou, E. Rodriguez-Carmona, M. Harlow, JA. Robson, AG. Moreland, JD. (2010). The Macular Assessment Profile test - a new VDU-based technique for measuring the spatial distribution of the macular pigment, lens density and rapid flicker sensitivity. *Ophthalmic Physiol Opt*. 30(5):470-483.
- Barbur, JL. Rodriguez-Carmona, M. Harlow, AJ. (2006). Establishing the statistical limits of "normal" chromatic sensitivity: CIE Proceedings Expert Symposium - 75 Years of the CIE Standard Observer (CIE x030:2006). ISBN: 3901906517.
- Barbur, JL. (2003). 'Double-blindsight' revealed through the processing of color and luminance contrast defined motion signals. *Progress in Brain Res*. 144(17):243-259.
- Barbur, JL. Birch, J. Harlow AJ. (1992). Threshold and suprathreshold responses to chromatic stimuli using psychophysical and pupillometric methods. In: *Non-invasive assessment of the visual system. Technical Digest Series. J. Opt. Soc. Am*, 1:51-54.
- Barbur, JL. Thomson, WD. Forsyth, PM. (1987). A new system for the simultaneous measurement of pupil size and two-dimensional eye movements. *Clin Vis Sci*, 2:131-2.
- Barnes, GR. (2008). Cognitive processes involved in smooth pursuit eye movements. *Brain Cognition*, 68(3):309-26.
- Birch. J, Harlow, AJ. Barbur. JL. (1992). New method based on random luminance masking for measuring isochromatic zones using high resolution colour displays. *Ophthalmic Physiol Opt*, 12(2):133-136.
- Björck, Å. (1996) *Numerical Methods for Least Squares Problems*, SIAM.

- Boff, K. Kaufman, L. Thomas, J. (Eds). (1986). Handbook of Perception and Human Performance. New York: Wiley.
- Bone, RA. Landrum, JT. Cains, A. (1992). Optical density spectra of the macular pigment in vivo and in vitro. *Vis Res*, 32:105-110.
- Bouma, H. (1962). Size of the static pupil as a function of wave-length and luminosity of the light incident on the human eye. *Nature*. 193:690-691
- Boynton, RM. Nagy, AL. Eskew, RT. (1986). Similarity of normalized discrimination ellipses in the constant-luminance chromaticity plane. *Perception*, 15(6):755-763.
- Brainard, DH. Pelli, DG. Robson, T. (2002). Display characterization. In the Encyclopedia of Imaging Science and Technology. J. Hornak (ed.), Wiley, 172-188.
- Brown, WRJ. (1951). The influence of luminance level on visual sensitivity to Color Differences. *J. Opt. Soc. Am*, 41(10):684-688.
- Brown, WRT, MacAdam, DL, (1949) Visual Sensitivities to Combined Chromaticity and Luminance Differences. *J. Opt. Soc. Am*, 39(10):808-823.
- Bushberg, JT. (2006). The Essential Physics of Medical Imaging (Second edition). Philadelphia, Lippincott Williams Wilkins.
- CIE Proceedings. (1951). Bureau Central de la CIE, Paris. 1(4):37.
- CIE. (1932). Commission internationale de l'Eclairage proceedings. Cambridge University Press.
- Clyde, WO. (1999). The human eye: structure and function. Sinauer Associates Inc. ISBN-10: 0878936459.
- Connolly, DM. (2011). Oxygenation state and twilight vision at 2438m. *Aviat Space Environ Med*, 82(1):2-8.
- Craik, KJW. (1938). The effect of adaptation on differential brightness discrimination. *J Physiol*. 92(4):406-421
- CRS Ltd, Cambridge Research Systems. www.crsLtd.com. Rochester, U.K.
- Curcio, CA. Sloan, KR. *et al.* (1990). Human photoreceptor topography. *J. Comp Neuro*, 292(4):497-523.
- CVRL. Colour Vision Research laboratory online database. www.cvrl.org. Institute of Ophthalmology. University College London.
- Daniels, L. Hock, HS. Nichols, D. Huisman, A. (2009). The effect of spatial attention on pupil dynamics. *JoV*, 10(7):87.

- Davidson, HR. (1951). Calculation of Color Differences from Visual Sensitivity Ellipsoids. *J. Opt. Soc. Am*, 41(12):1052-1055.
- De Launay, J. (1949). A note on the photo-pupil response. *J. opt. Soc. Am*, 39:364-367.
- Derrington, A.M., Krauskopf, J., Lennie, P. (1984). Chromatic Mechanisms in Lateral Geniculate Nucleus of Macaque. *Journal of Physiology*, 357, 241–265.
- Dischler, E. Valberg, A. (2006). Comparing chromatic detection ellipses of colour-deficient subjects with standard colour vision tests. *Perception* 35 (ECPV Abstract Supplement).
- E. Peli. (1990). Contrast in Complex Images. *J. Opt. Soc. Am*, 7(10): 2032–2040.
- Ellipses. *IEEE - Pattern Analysis and Machine Intelligence*. 21(5):476-480.
- Fitzgibbon, A. Pilu, M. Fisher, B. (1999). Direct Least Squares Fitting of Ellipses. *IEEE - Pattern Analysis and Machine Intelligence*. 21(5):476-480.
- Gander, W. Golub, GH. and Strebel, R. (1994). Least-square fitting of circles and ellipses. *BIT*, 43:558–578.
- Gander, W. (1981). Least squares with aquadratic constraint. *Numerische Mathematik*, 36:291–307.
- Gegengurtner, KR, Sharpe, LT. (Eds). (1999). *Color Vision: From Genes to Perception*. Cambridge University Press.
- Golz, J. MacLeod, D. (2003). Colorimetry for CRT displays. *J. Opt. Soc. Am*. 20(5):769-781.
- Graham, KB. Finlayson, G. Funt, B. (1997). Colour constancy for scenes with varying illumination. *Computer Vision and Image Understanding*, 65(2):311-321.
- Guild, J. (1931). The colorimetric properties of the spectrum. *Philosophical Transactions of the Royal Society of London (Royal Society of London, papers of a Mathematical or Physical Character)*. 230:149–187.
- Gunther, KL. Dobkins, KR. (2002). Individual differences in chromatic (red/green) contrast sensitivity are constrained by the relative number of L- versus M-cones in the eye. *Vis Res*, 42:1367–1378.
- Hammond Jr., BR. Wooten, BR. Snodderly, DM. (1997). Individual variations in the spatial profile of human macular pigment. *J. Opt. Soc. Am. A*, 14:1187-1196.

- Hammond Jr., BR. Fuld, K. Curran-Celentano. (1995). Macular pigment density in monozygotic twins. *Invest Ophthalmol Vis Sci.* 36(12):2531-41.
- Harrison, NA. Wilson, E. Critchley, HD. (2007). Processing of observed pupil size modulates perception of sadness and predicts empathy. *Emotion*, 7(4):724-729.
- Heathy Eyes. www.healthyeyes.org.uk (accessed Feb 2012).
- Heeger, D. www.cns.nyu.edu, Perception (graduate) lecture notes (accessed Feb 2012).
- Hita, H. Romero, J. Cervantes, A. Jimbez Del Barco, L. (1998). The influence of chromatic adaptation upon successive colour discrimination. *J. Optics (Pans)*. 20(2):87-94
- Hofer, H. Carroll, J. Neitz, J. Neitz, J, Williams, DR. (2005). Organization of the Human Trichromatic Cone Mosaic. *J. Neurosci.* 25(42):9669 –9679.
- Hunt, RW. (1998). *Measuring Colour* (Edition 3). Fountain Press. ISBN 0863433871.
- Ioana Tincas, I, Vasile MV. Muresan, PC. (2011). Pupil dilation and visual object recognition. Conference: International Conference on Cognitive Neuroscience (XI), Palma, Mallorca, Spain.
- Jordan, G. Deeb, SS. Bosten, JM. Mollon, JD. (2010). The dimensionality of color vision in carriers of anomalous trichromacy. *JoV*. 10(8):1–19.
- Judd, DB. (1951). Report of U.S. Secretariat Committee on Colorimetry and Artificial Daylight. In *Proceedings of the Twelfth Session of the CIE, Stockholm* (vol 1, page 11). Paris: Bureau Central de la CIE.
- Kallmark, FP. Ygge, J. (2005). Photo-induced foveal injury after viewing a solar eclipse. *Acta Ophthalmol Scand*, 83(5): 586-9.
- Kolb, H. Fernandez, E. Schouten, J. Ahnelt, P (1994). Are There Three Types of Horizontal Cell in the Human Retina? *J comp neuro*, 343:370-386
- Krauskopf, J. Gegenfurtner, K. (1992), Color discrimination and adaptation. *Vis Res.* 32(11):2165-2175.
- Krauskopf, J. Carroll, J. (2007). L:M cone ratios estimated by colour appearance, ERG, and adaptive optics methods. *Perception*. 36. ECVF Abstract Supplement.
- Krauskopf, J. Williams, DR, Heeley, DW. (1982). Cardinal directions of color space. 22(9):1123-31.

- Kulikowski, JJ. (2003). Neural basis of fundamental filters in vision. *Modulation of Neuronal Signalling: Implications for Active Vision*. NATO Science Series, Life Sciences. 334: 3-68.
- Land, EH. McCann, JJ. (1971). Lightness and Retinex theory. *J Opt Soc Am*. 61:1-11.
- Laurens, H. (1923). Studies on the relative physiological value of spectral lights. III. The pupillomotor effects of wave-lengths of equal energy content. *Amer. J. Physiol*. 64:97-119.
- Leeuwen, MT van. Numan, R. Kamermans, M. (2004). Colour-constancy is coded in the retina. *Perception*. 33. ECVF Abstract Supplement.
- Levine, MW. (2000). *Fundamentals of Sensation and Perception*. Oxford University Press, Oxford, ISBN: 9780198524663.
- Lindsay T. Sharpe, LT. Stockman, A. Wolfgang, J. Herbert, J. (2005). A luminous efficiency function, $V^*(\lambda)$ for daylight adaptation. *JoV*, 5, 948-968
- Loomis, JM. Berger, T. (1979). Effects of chromatic adaptation on color discrimination and color appearance. *Vis Res*. 19(8):891-901.
- MacAdam, DL. (1942). Visual sensitivities to color differences in daylight. *J. Opt. Soc. Am*. 32(5):247-274.
- Martinovic, J. Mordal, J. Wuerger, SM. (2011). Event-related potentials reveal an early advantage for luminance contours in the processing of objects. *JoV*, 11:7.
- McIntyre, M. (2002). *Colour Blindness: Causes and Effects*. Dalton Publishing, UK. ISBN 0954188608.
- Michelson, A. (1927). *Studies in Optics*. University of Chicago Press.
- Mollon, JD. Pokorny, P. Knoblauch, K. (eds). (2003). *Normal and Defective Colour Vision*. Oxford University Press. ISBN:9780198525301. Chapter 28 Macular Pigment: Nature's Notch Filter.
- Moreland, JD. Kerr, J. (1979). Optimization of a Rayleigh-type equation for the detection of tritanomaly. *Vision Research*. 19(12):1369-1375.
- Morgan, MJ. Adam, A. Mollon, JD. (1992). Dichromats detect colour-camouflaged objects that are not detected by trichromats. *Proc. Biol. Sci*. 248(1323): 291-5.
- Morovic, J. (2008). *Color Gamut Mapping (Edition 1)*. Wiley. ISBN:9780470030325.

Mullen, KT, Beaudot, WHA. Mcllhagga, WH. (2000). Contour integration in color vision: a common process for the blue-yellow, red-green and luminance mechanisms? *Vis Res*, 40, 639-655.

Nagy, AL. Eskew, RT Jr. Boynton, RM. (1987). Analysis of color-matching ellipses in a cone-excitation space. *J. Opt. Soc. Am.* 4(4):756-768.

Neelam, K. (2005). Measurement of Macular Pigment: Raman Spectroscopy versus Heterochromatic Flicker Photometry. *Invest Ophth Vis Sci.* 46:1023-1032.

Noboru, O. Robertson, AR. (2005). Standard and Supplementary Illuminants. *Colorimetry*. Wiley. Chapter 3. ISBN 0470094729.

Okawa, H. Alapakkam, PS. (2007) Optimization of Single-Photon Response Transmission at the Rod-to-Rod Bipolar Synapse. *Physiology*, 22(4): 279–286.

Oyster, CW. (2006). *The Human Eye: Structure and Function: Its Structure and Function* (new ed). Sinauer Associates Inc.,U.S. ISBN 9780878936441.

Paul E. Kilbride, PE. Alexander, KR. Fishman, M. Fishman, GA. (1988). Human macular pigment assessed by imaging fundus reflectometry. *Vis Res.* 29(6) 663–674.

Pham, H. (ed). (2006). *Springer Handbook of Engineering Statistics*. Springer. ISBN-10:1852338067.

Philipona, DL. O'Regan, JK. (2006). Color naming, unique hues, and hue cancellation predicted from singularities in reflection properties. *Visual Neuroscience* . 23:331–339.

Poirson, AB. Wandell, BA. Varner, D. Brainard, DH. (1990). Surface characterizations of color thresholds. *Journal of the Optical Society of America*, 7 :783-789.

Pokorny, J. Smith, V. (1970). Wavelength discrimination in the presence of added chromatic fields. *J Opt Soc America*, 69:562–9.

Pöppel, E. (1986). Long-range colour-generating interactions across the retina. *Nature*, 320:523 – 525.

Porrill, J. (1990). Fitting ellipses and predicting confidence envelopes using a bias corrected Kalman filter. *Image Vision and Computing*, 8(1):1140–1153.

Robson, AG. Moreland, JD. Pauleikhoff, D. Morrissey, T. Holder, GE. Fitzke, FW. Bird, AC. van Kuijk, FJ. (2003). Macular pigment density and distribution: comparison of fundus autofluorescence with minimum motion photometry. *Vis Res*, 43(16) :1765-1775.

Rodriguez-Carmona, ML. Harlow, JA. Walker, F. Barbur, JL. (2005). The variability of normal trichromatic vision and the establishment of the "normal" range. Proceedings of 10th Congress of the International Colour Association. Granada: 979-982.

Rodriguez-Carmona, ML. Kvansakul, J, Harlow, JA, Kopcke, W, Schalch, W, Barbur, JL. (2006). The effects of supplementation with lutein and/or zeaxanthin on human macular pigment density and colour vision. *Ophthalmic Physiol Opt.* 26 (2):137-147.

Rodriguez-Carmona, ML. (2006). Variability of chromatic sensitivity: fundamental studies and clinical applications. PhD Thesis, City University London, United Kingdom.

Rosin, PL, (1999). Further five-point fit ellipse fitting, *Graphical Models and Image Processing*, 61(5):245-259.

Rozanowski, M. Jarvis-Evans, J. Korytowski, W. (1995). Blue light-induced reactivity of retinal age pigment. In vitro generation of oxygen-reactive species. *J Biol Chem*, 270:18825-30.

Sacek, V. (2006). Amateur Telescope Optics. www.telescope-optics.net, (accessed Jan 2012).

Salomon D. (2005). *Curves and surfaces for computer graphics*. Springer, ISBN:0387241965.

Salvini-Plawen, L. V., Mayr, E. 1977. On the evolution of photoreceptors and eyes. *Evol. Biol.* 10:207-53.

Schmid, MC. Mrowka, SW. Turchi, J. Saunders, RC. Wilke, M. Peters, AJ. Ye, FQ. Leopold, DA. (2010). Blindsight depends on the lateral geniculate nucleus, *466(7304):373-7*.

Sheskin, DJ. (2007). *Handbook of Parametric and Nonparametric Statistical Procedures: Fourth Edition*. Chapman and Hall/CRC, ISBN-10:1584888148.

Shevell, SK. (2003). *The science of color (Edition 2)*. Elsevier. ISBN:0444512519.

Smith, G. Atchison, DA. (1997). *The Eye and Visual Optical Instruments*. Cambridge University Press. ISBN-10:0521478200.

Sparrow. JR. Zhou. J. Ben-Shabat, S. (2002). Involvement of oxidative mechanisms in blue-light-induced damage to A2E-laden RPE. *Invest Ophthalmol Vis Sci*, 43:1222-7.

Stanley, PA., Davies, AK., (1995). The effect of field of view size on steady-state pupil diameter. *Ophthalmic Physiol Opt.* 15(6):601-3.

Stiles, WS. Crawford, BH. (1933). The luminous efficiency of rays entering the eye pupil at different points. *Proc. R. Soc. Lond B.* 112:428-450.

Stockman, A. Sharpe, LT. (2006). Into the twilight zone: the complexities of mesopic vision and luminous efficiency. *Ophthalmic Physiol Opt.* 26(3): 225-39.

Stockman, A. Sharpe, LT. (2000). Spectral sensitivities of the middle- and long-wavelength sensitive cones derived from measurements in observers of known genotype. *Vis Res*, 40:1711-1737.

Stockman, A. Sharpe, LT. Fach, CC. (1999). The Spectral Sensitivity of the Human Short-Wavelength Cones. *Vis Res*, 39.

Thibos, LN. (1990). Optical limitations of the Maxwellian view interferometer. *Applied Optics*, 29(10):1411-1419.

Troxler, DIPV. (1804). Über das Verschwinden gegebener Gegenstände innerhalb unseres Gesichtskreises. [On the disappearance of given objects from our visual field]. *Ophthalmologische Bibliothek.* 2(2): 1–53. OCLC 491712012.

Valberg, A. (2005). *Light, Vision, Color.* Wiley, ISBN:0470849037.

van Norren, D. Vos, JJ. (1974). Spectral transmission of the human ocular media *Vision Research*, 14:1237-1244.

Ventura, DF. Rodrigues, AR. Moura, ALA. Vargas, ACC. da Costa, MF. Souza, JM. ou de Souza, JM. Silveira LCL . (2002). Color discrimination measured by the Cambridge Colour Vision Test (CCVT) in children and adults. In: *Reunião Anual da Association for Research in Vision and Ophthalmology.*

Vos, JJ. (1972). Literature review of human macular absorption in the visible and its consequences for the cone receptor primaries. The Netherlands: Netherlands Organization for applied scientific research, Institute for Perception.

Vos, JJ. (1978). Colorimetric and photometric properties of a 2-deg fundamental observer. *Color Research and Application*, 3:125Y128.

Walkey, HC. Barbur, JL. Harlow, JA, Hurden, Moorhead, AIR . Taylor, JAF. (2005). Effective contrast of colored stimuli in the mesopic range: a metric for perceived contrast based on achromatic luminance contrast. *J.Opt.Soc.Am*, 22(1):17-28.

Walkey, HC. Barbur, JL, Harlow, AJ. Makous, W. (2001). Measurements of Chromatic Sensitivity in the Mesopic Range. *Colour Research and Application*, 26:36-42.

- Weale, RA. (1988). Age and the transmittance of the human crystalline lens. *Journal of Physiology*. 395:577-587.
- Whittle, P. (1994). The psychophysics of contrast brightness. In A. L. Gilchrist (Ed.), *Lightness, Brightness, and Transparency*. Hillsdale, NJ: Lawrence Erlbaum Associates.
- Williams, DR. MacLeod, DIA. Hayhoe, M. (1981). Punctate sensitivity of the blue-sensitive mechanisms. *Vision Res*. 1981;21:1357–1375.
- Williams, SM. McCoy, AN. Purves, D. (1998). The influence of depicted illumination on brightness. *Proc Natl Acad Sci*. 95(22):13296–13300.
- Wright, WD. (1928). A re-determination of the trichromatic coefficients of the spectral colours. *Transactions of the Optical Society*, 30(4):141–164.
- Wright, WD. Pitt, FHG. (1934). Hue-discrimination in normal colour-vision. *Proceedings of the Physical Society*, 46(3):459–473.
- Wuerger, SM. Atkinson, P. Cropper, SJ. (2005). The cone inputs to the unique-hue mechanisms. *Vis Res*. 45:3210-3223.
- Wyszecki, G. Fielder, GH. (1971). New Color-Matching Ellipses. *J.Opt.Soc.Am*, 61(9):1135-1152.
- Wyszecki, G. Stiles, WS. (1982). *Color Science: concepts and methods, quantitative data and formulae* (2nd ed.). New York: Wiley.
- Wyszecki, G. Stiles, WS. (1967). *Color Science: concepts and methods, quantitative data and formulae* (1st ed.). New York: Wiley.
- Xiaofeng, R. Fowlkes, C. Malik, J. (2006). Figure-Ground Assignment in Natural Images. *European Conference on Computer Vision*. Graz, Austria.
- Yebra, JA. García, JL. Nieves, J. Romero. (2001). Chromatic discrimination in relation to luminance level. *Colour Research and Application*, 26(2):123–131.
- Yeh, T. Pokorny, J. Smith, VC. (1993). Chromatic discrimination with variation in chromaticity and luminance: data and theory. *Vis Res*. 33(13):1835-1845.
- Young, J. (2007). scienceblogs.com/purepedantry (accessed Feb 2012).
- Zhaoping, L. Geisler, WS, May, KA. (2011). Human Wavelength Discrimination of Monochromatic Light Explained by Optimal Wavelength Decoding of Light of Unknown Intensity. *PLoS ONE*, 6(5): e19248.